Electronic structure of multiorbital correlated systems

Dissertation
zur Erlangung des Doktorgrades
des Fachbereichs Physik
der Universität Hamburg

vorgelegt von
Evgeny Gorelov
aus Ekaterinburg

Hamburg
2007

Gutachter der Dissertation:	Prof. Dr. A. Lichtenstein Prof. Dr. M. Potthoff
Gutachter der Disputation:	Prof. Dr. A. Lichtenstein Prof. Dr. E. Pavarini
Datum der Disputation:	28.11.2007
Vorsitzender des Prüfungsausschusses:	PD. Dr. A. Chudnovskiy
Vorsitzender des Promotionsausschusses:	Prof. Dr. G. Huber
MIN-Dekan des Departments Physik:	Prof. Dr. A. Frühwald

Zusammenfassung

Wir stellen ein numerisch exaktes Verfahren zur Berechnung der lokalen elektronischen Struktur und magnetischer Eigenschaften korrelierter Systeme vor. Das Verfahren verwendet die kürzlich entwickelte Zeitkontinuum-Determinanten- Quanten-Monte-Carlo Methode zur lösung des Quanten-Störstellen-Problems. Mit diesem Zugang sind wir in der Lage, multiorbitale Störstellen-Probleme einschließlich der Coulomb-Wechselwirkung in der allgemeinsten Form anzugehen. Dieses Verfahren gestattet es, sowohl Spin-Suszeptibilitäten als auch Green-Funktionen zu berechnen, indem alle Merkmale der Zustandsdichte der Leitungselektronen genau berücksichtigt werden.

Die Zeitkontinuum-Quanten-Monte-Carlo Methode wurde angewandt, um die Eigenschaften eine Kondo-Störstelle mit einem einzelnen Spin zu berechnen, der an ein Band von Leitungselektronen mit beliebiger Zustandsdichte gekoppelt ist. Wir erörtern das Verhalten der Spin-Suszeptibilität einer Kondo-Störstelle in verschiedenen Umgebungen: in einem ultrakleinen Krümel, im Anderson-Modell eines Gitters mit auf den Gitterplätzen zufällig verteilten Energieniveaus und auf einem zweidimensionalen Gitter, auf dem die Zustandsdichte eine van-Hove-Singularität aufweist.

Für Atome in realistischen Übergangsmetallen wurde das Fünf-Band-Modell einer Kondo-Störstelle in einer metallischen Umgebung mit vollem Coulomb-Wechselwirkung-Vertex berechnet. Die Anwendung auf eine Kobalt Störstelle in einer Kupfer-Umgebung zeigt eine starke Renormierung einer ursprünglich nicht-wechselwirkenden Zustandsdichte nahe der Fermikante.

Um die Eigenschaften korrelierter Festkörper zu berechnen, wird die Zeitkontinuum-Quanten-Monte-Carlo Methode als Lösungsmethode für das Störstellenproblem innerhalb der Dynamischen Molekularfeld-Theorie benutzt. Der Metall-Isolator-Phasenübergang für zwei und drei anisotrope Orbitale auf dem Bete-Gitter mit Spin-Umklapp-Wechselwirkung wird betrachtet. Die gewonnenen Ergebnisse stimmen gut mit bekannten früheren Untersuchungen überein. Die Methode wird auf einen realen korrelierten Festkörper, Strontium-Ruthenat (Sr_2RuO_4), angewandt. Wir untersuchen die Bedeutung nicht-diagonaler Terme im Wechselwirkungsteil des Hamilton-Operators, der sich auf Spin-Umklapp- und Paar-Hüpf-Prozesse bezieht.

Abstract

We propose a numerically exact scheme to calculate the local electronic structure and magnetic properties of correlated systems. The scheme employs the recently developed determinantal Continuous Time Quantum Monte Carlo method for the solution of the quantum impurity problem. With this approach, we are able to treat multiorbital impurity problems, including Coulomb interaction of the most general form. This scheme allows to calculate spin susceptibilities as well as Green functions, accurately taking into account all the features of the conduction electron density of states.

The Continuous Time Quantum Monte Carlo method has been applied to calculate properties of a single-spin Kondo impurity coupled to a band of conduction electrons with an arbitrary density of states. We discuss the behavior of the spin susceptibility of a Kondo impurity embedded into different environments: an ultrasmall grain, the Anderson model, corresponding to a lattice with random on-site energy levels, and a two-dimensional lattice, where the density of states has a van Hove singularity.

The realistic five-band model for transition metal atoms with full Coulomb interaction vertex as a Kondo impurity in a metal matrix has been calculated. Application to a cobalt impurity in a copper matrix shows a strong renormalization of the initial non-interacting density of states near the Fermi level.

In order to calculate properties of correlated solids, the Continuous Time Quantum Monte Carlo method is used as an impurity solver within the dynamical mean-field theory. The metal-insulator phase transition for two and three anisotropic orbitals on the Bethe lattice with spin-flip interactions is considered. The results obtained are in good agreement with previous studies. The method is applied to a real correlated solid, namely strontium ruthenate (Sr_2RuO_4). We investigated the role of non-diagonal terms in the interaction part of the Hamiltonian, related to spin flip and pair hopping interactions.

Contents

1 Introduction

Strongly correlated electronic systems are of great physical interest nowadays. From a technological point of view, the most interesting feature is that many of such systems are extremely sensitive to small changes in their control parameters (pressure, temperature, doping, magnetic field, etc.). Moreover, these systems usually have very complex phase diagrams. The reason of this unusual behavior is the competition between different ordering states, related to the complicated balance between the kinetic energy and the electron-electron interactions. Because kinetic and potential energy are of the same order of magnitude, competition between localization and delocalization of electrons takes place. This leads to variety of nontrivial effects related to spin, charge and orbital fluctuations. It was found, experimentally, that some oxide systems containing copper ions (so-called high-T_c) have unexpectedly high superconducting transition temperatures (above liquid-nitrogen temperatures). Another systems, exhibiting interesting correlation effects are so-called heavy-fermion systems. These compounds contain rare-earth or actinide elements where the effective mass of the electrons can be extremely large. This fact in conjunction with large orbital degeneracy leads to a couple of effects: the exceptionally large Seebeck coefficients, which can be used for constructing low-temperature thermoelectric devices, colossal magnetoresistance, and giant nonlinear optical susceptibility with an ultrafast recovery time. This will be useful in the design of data storage and processing devices.

The Kondo effect is another demonstration of electron correlations; in the 1930s it was found that even a little fraction of magnetic transition metal atoms added to nonmagnetic host metal leds to unusual asymptotic behaviour of resistivity in the low temperature limit. Namely, lowering the temperatue below some point lead to an increase in the resistivity. The first theoretical explanation was given by Kondo in 1964. He showed that the resistivity increase is related to spin-dependent scattering of the itinerant electrons by the magnetic moments of the transition metal impurities. For a long time, the consequences of this behaviour were investigated with macroscopic methods, and most experiments were done for dilute 3d transition elements in Au and Cu host metals. Recently it became possible to measure the properties of isolated impurities on the atomic scale using Scanning Tunnel Microscopy (STM). The consideration of single surface Kondo-systems lead to revealing a variety of very interesting many-body effects in chains, clusters and islands.

Another manifestation of correlation effects is the Mott metal-insulator transition; de Boer and Verwey in 1937 reported that many transition-metal oxides with a partially filled d-electron band were nonetheless poor conductors and indeed often insulators. A typical example in their report was NiO. Concerning their report, Peierls pointed out the importance of the electron-electron correlation; strong Coulomb repulsion between electrons could be the origin of the insulating behavior. These observations launched the long and continuing history of the field of strongly correlated electrons, particularly the effort to understand how materials with partially filled bands could be insulators and, as the history developed, how an insulator could become a metal as controllable parameters were varied.

The metal-insulator transition (MIT) in oxide materials is indeed the most outstanding and prominent feature of strongly correlated electrons and has long been central to research in this field. In the past sixty years, much progress has been made from both theoretical and experimental sides in understanding strongly correlated electrons and MIT. In theoretical approaches, Mott in 1949 took the first important step toward understanding how electron-electron correlations could explain the insulating state, and we call this state the Mott insulator.

There are two major approaches to the theoretical understanding of many electron systems: density-functional theory (DFT) and the simplified model Hamiltonian approach (e.g. Anderson impurity model (AIM), Kondo impurity model, Hubbard model and its generalizations). On one hand, we have the simplified model Hamiltonian approaches that can catch these correlation effects qualitatively but often fails to describe particular real system quantitatively. On the other hand, the DFT approach allows us to treat quite complicated realistic systems, but because of its mean-field nature it can overlook some physically relevant effect induced due to electronic correlations (e.g. MIT cannot be described in framework of the DFT).

The recent breakthrough in this field was done by G. Kotliar, A. Georges, W. Metzner, and D. Vollhardt (see Refs. [1, 2, 3]). They proposed the way on how to map the lattice problem to a self-consistent impurity one. This approximate approach is based on taking the limit of infinite dimensions. Although, this method initially was designed to solve simplified model Hamiltonians (like Hubbard one), a short time later it was extended to realistic systems, involving DFT as a starting point [4, 5]. So far this approach has become surprisingly successful in treating correlated solids, it still has a number of obstacles. First, since DMFT is a local approximation, it cannot treat non-local correlations, that are of great importance in a variety of physically interesting systems (e.g. high-temperature superconductors, low-dimensional conductors). This problem can be overcome by different extensions of the DMFT approach (e.g. cluster DMFT [6], dual fermion approach [7], self-energy functional [8]). Another problem of the DMFT technique is an absence of a universal impurity solver. Attempts to make an impurity solver encountered many difficulties, and now we have a variety of impurity solvers, each of them can be applied only within a certain range of parameters (see Chapter 2, sec. 2.2). For such interesting systems, as cobalt impurity on metallic surfaces, taking into account many correlated orbitals is of crucial importance. Another important requirement is the possibility to take into account coupling of the impurity to electronic band with an arbitrary density of states. Up to now the most promising method has been quantum Monte-Carlo (QMC). As the base of our approach, we used the so-called continuous time QMC method (see Chapter 2, sec. 2.3), which is a promising universal impurity solver.

The main target of the present work is to work out a method that can help us explain and predict properties of correlated systems. The major requirements to the method are following:

- Possibility to treat multiorbital impurity models.
- Ability to take into account complete atomic-like Coulomb interaction, including the complicated terms like spin-flips, pair hoppings, etc.
- Careful treatment of band-structure anomalies in the conduction electron density of states.

The structure of this thesis is the following. In Chapter 2, sec. 2.1 – 2.2 a brief analysis of present theoretical methods is done, current state of affairs in modern solid-state physics is discussed. In section 2.3 we describe continuous time quantum Monte-Carlo – the method we are developing and applying to correlated systems. In Chapter 3 we discuss the Kondo (one-spin) impurity embedded into a conduction band with arbitrary density of electron states. In order to do that we construct an extension of the CT-QMC method to spin operators. Chapter 4 contains technical details of the application of the CT-QMC method to the multiorbital impurity problem, taking into account full atomic-like Coulomb interaction. In this Chapter we discuss results for a realistic model, namely a cobalt atom embedded into a copper matrix. In Chapter 5 we develop the method designed to describe solids with correlated electron subsystems. We apply our mutiorbital impurity solver to a lattice problem in the dynamical mean-field approximation. We discuss the physical relevance of full Coulomb interaction on the example of real correlated solid (Sr_2RuO_4).

2 Theoretical approaches to strong correlated systems

In this Chapter we consider ”state-of-the-art” methods for theoretical description of the electrons in solids. Materials with correlated electrons exhibit one of the most intriguing phenomena in condensed matter physics. The main aim of theoretical physics is to describe and predict different properties of the novel materials, based on the electronic structure of these materials. Modern solid-state theory explains the physical properties of numerous materials, such as simple metals, important semiconductors and insulators. They can be successfully described in the framework of density functional theory (DFT, see sec. 2.1). However, the materials containing partially filled d or f electron shells, where electrons occupy narrow bands, often have unusual properties that are harder to explain and the DFT method using the independent-electron model is not accurate enough when applied to strongly correlated materials.

The many body effects, however, can be described using simplified model Hamiltonians, like the Hubbard model. But this approach also has some problems: the Hubbard model can be solved exactly only in few limit cases (either 1 or ∞ dimensionality of the system, or infinite on-site repulsion, etc.).

The recently developed Dynamical mean-field theory technique (see Chapter 5), that in fact maps a many-body lattice problem to a single-site problem with effective self-consistent parameters, allows to solve a variety of model Hamiltonians on the lattice using effective numerical techniques such as quantum Monte Carlo, numerical renormalization group, exact diagonalization, etc. (see sec. 2.2).

2.1 Density functional theory

Electronic-structure calculations of solids have considerably evolved from early approaches, such as band structure calculations in periodic model potentials, aimed at reproducing simple crystals into very sophisticated and powerful techniques. These techniques usually require no experimental input beyond the basic information on atomic composition and some structural data. This is the origin of the definitions of ab-initio, or first-principles techniques. In conjunction with the enormous increase in computer power, ab-initio methods now allow us to accurately reproduce and to predict electronic and structural properties of real materials, and not just the simplest ones. This predictive power makes a strong case in favor of ab-initio methods, whenever they are applicable, with respect to empirical or semiempirical methods.

Solving the many-body Schrödinger equation for electrons in a real material is by no means a trivial task even in the presence of simplifying assumptions (such as perfect periodicity for crystals). One of the most popular methods corresponds to the Density Functional Theory (DFT) [9], mainly in the Local Density Approximation (LDA) [10].

The DFT is a ground-state theory in which the emphasis is on the charge density as the relevant physical quantity. DFT in the LDA has proved to be highly successful in describing structural and electronic properties in a vast class of materials. Furthermore LDA is computationally very simple. For these reasons LDA has become a common tool in first-principles calculations aimed to describe and predict the properties of complex condensed matter systems (for introduction and review see e.g. [11, 12]).

We can start from the statement that an external potential $V(\mathbf{r})$ acting on a system of N interacting electrons will determine the charge density $n(\mathbf{r})$ of the ground state. This is exactly what has been proven by Hohenberg and Kohn [9]: there is only one external potential $V(\mathbf{r})$ which yields a given ground-state charge density $n(\mathbf{r})$.

DFT arises from the Hohenberg and Kohn theorem [9] : the ground state energy E is also uniquely determined by the ground-state charge density. According to this theorem, no two different potentials acting on the electrons of a given system can give rise to a same ground-state electronic charge density. This property can be used in conjunction with the standard Rayleigh-Ritz variational principle of quantum mechanics to show that such $F[n(\mathbf{r})]$ functional of the electron charge density exists, that the functional:

$$E[n(\mathbf{r})] = F[n(\mathbf{r})] + \int n(\mathbf{r})V(\mathbf{r})d\mathbf{r} \tag{2.1}$$

is minimized by the electron charge density of the ground state corresponding to the external potential $V(\mathbf{r})$, under the constraint that the integral of $n(\mathbf{r})$ equals the total number of electrons. Furthermore, the value of the minimum coincides with the ground-state energy. In this Chapter we use the atomic units: $\hbar = e = m = 1$, where e and m are the electron charge and mass respectively. The atomic unit of energy 1 a. u. $= 27.2\ eV$.

An enormous conceptual simplification of the quantum-mechanical problem of the search of the ground-state properties of a system of interacting electrons is gained by replacing the traditional description based on wave-functions with a much more tractable description in terms of the charge density. Since the first approach involves $3N$ independent variables, where N is the number of electrons, the second one depends only on 3 variables. The major problem hampering a straightforward application of this remarkably simple result is that the form of the F functional is unknown.

One year later, Kohn and Sham (KS) [10] reformulated the problem and opened the way to practical applications of DFT. First, the system of interacting electrons is mapped on to a fictitious system of non-interacting electrons having the same ground state charge density $n(\mathbf{r})$. This is performed by introducing KS orbitals $\psi_i(\mathbf{r})$ for N electrons

$$n(\mathbf{r}) = \sum_{i=1}^{N} |\psi_i(\mathbf{r})|^2 . \tag{2.2}$$

Charge conservation requires that the KS orbitals obey orthonormality condition:

$$\int \psi_i^*(\mathbf{r})\psi_j(\mathbf{r})d\mathbf{r} = \delta_{ij}. \tag{2.3}$$

Than the energy functional can be rewritten in the following form:

$$E[n(\mathbf{r})] = T_0[n(\mathbf{r})] + \frac{1}{2}\int \frac{n(\mathbf{r})n(\mathbf{r}')}{|\mathbf{r}-\mathbf{r}'|}d\mathbf{r}d\mathbf{r}' + E_{\mathrm{xc}}[n(\mathbf{r})] + \int n(\mathbf{r})V_{\mathrm{ext}}(\mathbf{r})d\mathbf{r}, \tag{2.4}$$

where $T_0[n]$ denotes the kinetic energy of noninteracting electrons with the density $n(\mathbf{r})$

$$T_0[n(\mathbf{r})] = -\frac{1}{2}\sum \int \psi_n^*(\mathbf{r})\frac{\partial^2\psi_n(\mathbf{r})}{\partial\mathbf{r}^2}d\mathbf{r}, \tag{2.5}$$

the second term is the Hartree energy, it describes the electrostatic interaction between clouds of charge. The third term is exchange-correlation energy that include all the rest of

Coulomb interaction between the electrons. The last term of Eq. (2.4) is a contribution of the external field described by the $V_{\rm ext}(\mathbf{r})$ potential.

Variation of the energy functional with respect to $n(\mathbf{r})$ with the constraint that the number of electrons is kept fixed $\int n(\mathbf{r})d\mathbf{r} = N$ leads formally to the same equation that would hold for a system of non-interacting electrons in effective potential

$$V_{eff}(\mathbf{r}) = V(\mathbf{r}) + \int \frac{n(\mathbf{r}')}{|\mathbf{r}-\mathbf{r}'|}d\mathbf{r}' + V_{xc}(\mathbf{r}), \tag{2.6}$$

where

$$V_{xc}[n(\mathbf{r})] = \frac{\delta E_{xc}[n(\mathbf{r})]}{\delta n(\mathbf{r})} \tag{2.7}$$

is a definition of the exchange-correlation potential. Other words, now we have to solve the one-electron Schrödinger equation:

$$\left(-\frac{1}{2}\frac{\partial^2}{\partial \mathbf{r}^2} + V_{eff}(\mathbf{r})\right)\psi_n(\mathbf{r}) = \varepsilon_n \psi_n(\mathbf{r}). \tag{2.8}$$

The Kohn-Sham scheme is a practical way to implement DFT, provided quite accurate approximation for the exchange-correlation energy, $E_{xc}[n(\mathbf{r})]$. Kohn and Sham [10] proposed to assume that each small volume of the system contributes the same constant exchange-correlation energy as an equal volume of a homogeneous electron gas at the same density. With this assumption, the exchange-correlation energy functional and potential read:

$$E_{xc}[n(\mathbf{r})] = \int \varepsilon_{xc}(n(\mathbf{r}))n(\mathbf{r})d\mathbf{r}, \tag{2.9}$$

$$V_{xc}(n(\mathbf{r})) = \left(\varepsilon_{xc}(n) + n\frac{d\varepsilon_{xc}(n)}{dn}\right)_{n=n(\mathbf{r})}, \tag{2.10}$$

where $\varepsilon_{xc}(n)$ is the exchange-correlation energy per particle in an homogeneous electron gas at density n. This approximation is known as the *local density approximation* (LDA).

Approximate forms for $\varepsilon_{xc}(n)$ have been known for a long time. Numerical results from nearly exact Monte-Carlo calculations for the homogeneous electron gas were obtained by Ceperley and Alder [13]. The LDA is exact in the limit of high density or of a slowly varying charge-density distribution [10]. LDA has turned out to be much more successful than expected [14]. Although it is very simple it yields a description of the chemical bond that is superior to that obtained by Hartree-Fock, and it compares well to much weightier quantum Chemistry methods.

For weakly correlated materials such as semiconductors structural and vibrational properties are accurately described: the correct structure is usually found to have the lowest energy, bond lengths, bulk moduli and phonon frequencies are accurate within a few percent [14].

LDA also has some well-known drawbacks. It overestimates the crystal cohesive energies (by $\sim 20\%$) and underestimates (by $\sim 50\%$) the band gaps in insulators. It leads to inability of proper description of strongly correlated systems, such as transition-metal oxides. In general, DFT is a ground-state theory and KS eigenvalues and eigenvectors do not have a well defined physical meaning. Nevertheless, in the lack of better and equally general methods, KS eigenvalues are often used to estimate excitation energies. The general features of the low-lying energy bands in solids obtained in this way are generally considered to be at least qualitatively correct, in spite of the fact that the LDA is known to substantially underestimate the optical gaps in insulators.

The most successful extension of the LDA allowing to treat some of correlated systems mentioned above was the LDA+U method [15]. This method includes the orbital dependence of the static self-energy operators, missing from the KS potential, in a relatively crude, pseudoatomic way, neglecting the fine details of the spatial variations of the Coulomb potential. But LDA+U does not contain true many-body physics. This approach is successful in describing long-range ordered and insulating states of correlated electronic systems, but it fails to describe strongly correlated paramagnetic states [16, 17].

To go beyond LDA+U and capture the many-body nature of the electron-electron interaction, i.e., the frequency dependence of the self-energy, the LDA+DMFT scheme have been developed [4, 5]. The essence of this scheme is to solve the Hubbard lattice model (that includes only a few degrees of freedom corresponding to strong correlated orbitals) in dynamical mean-field theory (DMFT) approximation [1, 18] (for details see Chapter 5) including interacting of the strong correlated orbitals with the rest of the electronic system obtained in framework of LDA (or LDA+U).

The LDA+DMFT approach is the only LDA extension that is able to describe the physics of strongly correlated, paramagnetic metals with well-developed upper and lower Hubbard bands and a narrow quasiparticle peak at the Fermi level. This characteristic three-peak structure is a signature of the importance of many-body effects [18, 19].

Due to the equivalence of the DMFT single-site problem and the Anderson impurity problem, a variety of approximative techniques have been employed to solve the DMFT equations,such as the iterated perturbation theory (IPT) and the non-crossing approximation (NCA) as well as numerical techniques like quantum Monte Carlo simulations (QMC), exact diagonalization (ED), or numerical renormalization group (NRG). For details of these numerical methods see sec. 2.2.

Since the mentioned above approximative analytical methods like IPT and NCA are uncontrollable approximations, we shall stress on numerical methods, especially on numerically exact continuous time QMC (CT-QMC) method.

2.2 Many-body impurity solvers

Impurity solvers play an essential role in the numerical investigation of strongly correlated electron systems. The DMFT scheme (see Chapter 5) give us a simple way to get an insight to physics of correlated solids. The solution of the impurity problem is usually the most difficult part of this scheme. Another application of an impurity solver is to obtain spectral and magnetic properties of quantum impurities such as single adatoms, chains of them, quantum dots, etc. The physical properties of these systems are caused by many-body effects, and accurate treatment of this quantum-mechanical model is essential for investigation of a such interesting phenomena as e.g. Kondo effect (for details see Chapter 3). In this section we give an overview of some of the methods, pointing out their strengths and limitations. The technical details of different impurity solvers will be explained in the following subsections.

The use of the terminology ”impurity” is due to historical reasons: this expression is used in a very general sense, namely a small interacting system (the impurity) with only a few degrees of freedom coupled to a large single-particle system (the environment or bath) with very many degrees of freedom, and where both subsystems have to be treated quantum mechanically. In the Kondo problem (see Chapter 3 and Refs. [20, 21]), the small system is a magnetic impurity, such as a cobalt ion, interacting with the conduction electrons of a nonmagnetic metal such as gold [20] (see Chapter 4). Other realizations are for example artificial impurities such as quantum dots hosting only a small number of electrons. Here, the environment is formed by the electrons in the leads.

Any theoretical method for the investigation of quantum impurity systems has to face a number of serious obstacles. First of all, because the environment typically consists of a continuum of quantum-mechanical degrees of freedom, one has to consider a wide range of energies – from a high-energy cut-off (which can be of the order of several eV) down to arbitrarily small excitation energies. On the other hand, because the impurity degrees of freedom usually form an interacting quantum-mechanical system, their coupling to a continuum of excitations with arbitrarily small energies can result in infrared divergencies in perturbational treatments. A well-known example for this difficulty is the Kondo problem (see Chapter 3): Its physics is governed by an energy scale, the Kondo temperature T_{K}, which depends non-analytically on the spin-exchange coupling J between the impurity and the conduction band of the host, $\ln T_{\mathrm{K}} \propto -1/J$ (see [20] for a detailed description of the limitations of the perturbational approach for the Kondo model and the single-impurity Anderson model).

Another motivation to study impurity solvers is, that lattice models, such as the Hubbard model, can be mapped in some approximation onto impurity models of the above type. For the Hubbard model and other lattice models of correlated electrons this is achieved via the dynamical mean-field theory (DMFT), see Chapter 5.

At the present time, there is no universal impurity solver that works efficiently and produces accurate solutions for the Green function in all regimes of parameters. Instead what we have is a large number of techniques, which are good in some regions of parameters. In many cases when there are various methods can be applied, there is a conflict between accuracy and computational cost, and in many instances one has to make a compromise between efficiency and accuracy to carry out the exploration of new complex materials (for review see e.g. Ref. [22]).

The models we are going to solve are the following: Anderson impurity model (AIM, see Chapter 4, section 4.1) and Kondo model (see Chapter 3). There are two exactly soluble limits of the multiorbital Anderson impurity model (see Chapter 4), for a general environment of non-interacting band electrons (bath). The atomic limit when the hybridization vanishes and the band limit when the interaction matrix U is zero. There are methods which are tied to expansions around each of these limits. It is straightforward to construct the perturbative expansion of the self–energy in powers of U up to second order, and resum certain classes of diagrams such as ring diagrams and ladder diagrams. This is an approach known as the fluctuation exchange approximation, and it is certainly reliable when U is less than the half–bandwidth, D. These impurity solvers are very fast since they only involve matrix multiplications and inversions. They also have good scaling, going as N^3 where N is the number of orbitals or the cluster size.

The expansion around the atomic limit is more complicated. A hybridization function with spectral weight at low frequencies is a singular perturbation at zero temperature. Nevertheless approaches based on expansion around the atomic limit are suitable for describing materials where there is a gap in the one–particle spectra, or when the temperature is sufficiently high that one can neglect the Kondo effect. This includes Mott insulating states at finite temperatures, and the incoherent regime of many transition metal oxides and heavy fermion systems. Many approaches that go beyond the atomic limit exist: direct perturbation theory in the hybridization, resummations based on equation of motion methods, such as the Hubbard approximations, resolvent methods, and slave particle techniques such as the non–crossing approximation (NCA) and their extensions. Mean–field methods are based on a functional integral representation of the partition function, and the introduction of auxiliary slave bosons [23]. The saddle point approximation [24] gives results which are very similar to those of the Gutzwiller method, and corrections to the saddle point can be carried out by a loop expansion [25]. Unfortunately the perturbative corrections to the saddle point are complicated and have not been evaluated in many cases [24]. Interpolative methods bear some resemblance to the analytic parameterizations of V_{xc} in LDA. One uses different approximations to the self–energy of the impurity model, viewed as a functional of $\Delta(i\omega)$, in different regions of frequency. The idea is to construct interpolative formulae that become exact in various limits, such as zero frequency where the value of the Green function is dictated by Luttinger theorem, high frequencies where the limiting behavior is controlled by some low–order moments, and in weak and strong coupling limits where one can apply some form of perturbation theory. This approach has been very successful in unraveling the Mott transition problem in the context of model Hamiltonians, and it is beginning to be used for more realistic studies. But all the methods described above involve some approximations. Although they give a reasonable results in some range of parameters, for some regimes (including physically interesting) results can be even qualitatively wrong, since these approximations are uncontrollable. On the other hand there are numerically exact methods, such as the Hirsch-Fye quantum Monte Carlo method (QMC) [26]. In this QMC method one introduces a Hubbard–Stratonovich fields and averages over these fields using Monte Carlo sampling. This is a controlled approximation using a different expansion parameter, the size of the mesh for the imaginary time discretization. Unfortunately, it is computationally very expensive as the number of time slices and the number of Hubbard–Stratonovich fields increases. This QMC method is described in section 2.2.3. The main problem of this method is a poor scaling with increasing number of orbitals, since the number of Hubbard–Stratonovich fields increases as the square of the number of orbitals.

Another way to solve the impurity problem is to use techniques based on exact diagonalization methods (see section 2.2.1), and their modifications such as Wilson renormalization group (NRG, see section 2.2.2) techniques and density matrix renormalization group methods. These are very powerful techniques, but due to the exponential growth of the Hilbert space, they need to be tailored to the application at hand.

2.2.1 Exact diagonalization and Lanczos's method

The expression ”Exact Diagonalization” (ED) is used to describe a number of different approaches which yield numerically exact results for a finite lattice system by directly diagonalizing the matrix representation of the system's Hamiltonian in an appropriate many-particle basis (for a short review on ED and related methods see e.g. [27]). The simplest, and the most time- and memory- consuming approach is the *complete diagonalization* of the matrix which enables one to calculate *all* desired properties. However the dimension of the basis for a strongly interacting quantum system grows exponentially with the system size, so that it is impossible to treat systems with more than a few sites or orbitals [28].

A number of software libraries provide complete diagonalization routines which take a matrix as input and return all of the eigenvalues and eigenvectors as output. Among the most useful are the routines published in *Numerical Recipes* [29] as well as the LAPACK [30] library, which in combination with an efficient implementation of the Basic Linear Algebra Subprogrammes the BLAS [31, 32] provides a very efficient implementation of linear algebra tools. Such routines can be used to diagonalize the Hamiltonian matrix of a finite quantum lattice system directly.

The approach normally used [29] is first to transform the matrix to tridiagonal form using a sequence of Householder transformations and then to diagonalize the resulting tridiagonal matrix $\mathbf{T}$ using the QL or QR algorithm, which carries out a factorization $\mathbf{T} = \mathbf{QL}$ with $\mathbf{Q}$ an orthogonal and $\mathbf{L}$ a lower triangular matrix. The computational cost of this combined approach scales as $\frac{2}{3}n^3$ if only the eigenvalues are obtained, and $\approx 3n^3$ when the eigenvectors are also calculated, where n is the dimension of the matrix.

A complete diagonalization of the Hamiltonian matrix is nevertheless useful for testing purposes: to test our CT-QMC solver we used exact diagonalization program [28, 5] designed to obtain spectral properties of multiorbital impurity in atomic limit (without connection to bath of free electrons).

Since complete diagonalization of the many-body Hamiltonian is extremely computationally expensive and in the investigation of condensed matter systems one is often interested in the low-energy properties, it is possible to reach substantially larger system sizes using iterative diagonalization procedures, which also yield results to almost machine precision in most cases. The iterative diagonalization methods allow for the calculation of ground state properties and (with some extra effort) some low-lying excited states are also accessible. In addition, it is possible to calculate dynamical properties (e.g., spectral functions, time-evolution) as well as behavior at finite temperature. Nearly every system and observable can be calculated in principle, although the convergence properties may depend on the system under investigation. For example, with the effective atomic Hamiltonian for d or f states

$$H^{at} = \sum_{mm'\sigma} \varepsilon_{mm'} c^{+}_{m\sigma} c_{m'\sigma} + \frac{1}{2} \sum_{\{\sigma m\}} U_{m_1 m_2 m_1' m_2'} c^{+}_{im_1\sigma} c^{+}_{im_2\sigma'} c_{im_1'\sigma'} c_{im_2'\sigma} \tag{2.11}$$

where m_i are orbital indices and σ is spin, we need to diagonalize the atomic many-electron problem:

$$H^{at}|\upsilon >= E^{at}_{\nu}|\upsilon > \tag{2.12}$$

and then the exact atomic Green function can be found using eigenfunctions and eigenvectors of the Hamiltonian the following way [33]:

$$G^{\sigma}_{mm'}(i\omega) = \frac{1}{Z} \sum_{\mu\nu} \frac{\langle \mu | c_{m\sigma} | \nu \rangle \left\langle \nu \left| c^{+}_{m'\sigma} \right| \mu \right\rangle}{i\omega + E_\mu - E_\nu} (e^{-\beta E_\mu} + e^{-\beta E_\nu}). \tag{2.13}$$

The basic idea of the Lanczos method [34] for effective diagonalization (search of the ground state) of Eq. (2.12) is that a special basis set can be constructed where the Hamiltonian has a tridiagonal form. This is derived iteratively as shown below. We are starting from arbitrary wave function $|\phi_0\rangle$. Than we apply the Hamiltonian H to this initial state and subtract the projection over $|\phi_0\rangle$:

$$|\phi_1\rangle = H\,|\phi_0\rangle - \frac{\langle \phi_0 | H\,|\phi_0\rangle}{\langle \phi_0\,|\phi_0\rangle} |\phi_0\rangle \tag{2.14}$$

which satisfies $\langle \phi_0\,|\phi_1\rangle = 0$. The next state that is orthogonal to both previous can be constructed the following way:

$$|\phi_2\rangle = H\,|\phi_1\rangle - \frac{\langle \phi_1 | H\,|\phi_1\rangle}{\langle \phi_1\,|\phi_1\rangle} |\phi_1\rangle - \frac{\langle \phi_1\,|\phi_1\rangle}{\langle \phi_0\,|\phi_0\rangle} |\phi_0\rangle\,. \tag{2.15}$$

The procedure can be written in the recurrent form:

$$|\phi_{n+1}\rangle = H\,|\phi_{n+1}\rangle - a_n\,|\phi_n\rangle - b_n^2\,|\phi_{n-1}\rangle \tag{2.16}$$

where $a_n = \frac{\langle \phi_n | H | \phi_n \rangle}{\langle \phi_n\,|\phi_n\rangle}$ and $b_n^2 = \frac{\langle \phi_n\,|\phi_n\rangle}{\langle \phi_{n-1}\,|\phi_{n-1}\rangle}$. Here we use $b_0 = 0$ and $|\phi_{-1}\rangle = 0$. In this basis the Hamiltonian matrix becomes tridiagonal

$$H = \begin{pmatrix} a_0 & b_1 & 0 & 0 & \dots \\ b_1 & a_1 & b_2 & 0 & \dots \\ 0 & b_2 & a_2 & b_3 & \dots \\ 0 & 0 & b_3 & a_3 & \dots \\ \vdots & \vdots & \vdots & \vdots & \ddots \end{pmatrix}, \tag{2.17}$$

where n =1,2,..etc. The matrix elements, a_n and b_n, are related to the moments of the Hamiltonian. When n increases, the lowest eigenvalue of the tridiagonal matrix approaches the ground-state energy. And the eigenfunction of this lowest eigenvalue gets closer to the ground-state wave function [35]. The Green function also can be obtained using this method in spirit of Eq. (2.13) formalism [28, 3].

Although these methods are applicable to small to moderate systems they meet some obstacles describing Kondo-systems at low temperatures. It is caused by principal discreteness of the resulting spectrum and can lead to very spiky spectral function. One can overcome this problem using Numerical renormalization group, that will be discussed in the next section.

2.2.2 Numerical renormalization group

In the beginning of the 1970's, Wilson developed the concept of a fully non-perturbative renormalization group transformation. Applied to the Kondo problem, this numerical renormalization group method (NRG) gave for the first time the full crossover from the high-temperature phase of a free spin to the low-temperature phase of a completely screened spin. It is the substantial merit of this method in comparison to ED and Lanczos methods described above. The NRG has been later generalized to a variety of quantum impurity problems, such as Anderson and Kondo impurity models [20], periodical Anderson model [36] and Holstein model [37] (for review see e.g. Ref. [21]). The applications of the NRG scheme include variants of the original Kondo problem as well as lattice systems in the framework of the dynamical mean field theory [38].

The general strategy of the NRG is the following. As specific example, let us consider the Kondo model which describes magnetic impurity with spin $\mathbf{S}$ coupled to the electrons of a single-particle conduction band via an exchange interaction of the form $J\mathbf{S}\cdot\mathbf{s}$, where $\mathbf{s}$ the spin of the conducting electrons. The NRG starts with a logarithmic discretization of the conduction band in intervals $[\Lambda^{-(n+1)}\omega_{\mathrm{c}}, \Lambda^{-n}\omega_{\mathrm{c}}]$ and $[-\Lambda^{-n}\omega_{\mathrm{c}}, -\Lambda^{-(n+1)}\omega_{\mathrm{c}}]$ ($n = 0, 1, 2, \ldots$). We shall call $\Lambda > 1$ the NRG discretization parameter. After a sequence of transformations, the discretized model is mapped onto a semi-infinite chain with the impurity spin representing the first site of the chain. The Kondo model in the semi-infinite chain form is diagonalized iteratively, starting from the impurity site and successively adding degrees of freedom to the chain. Due to the logarithmic discretization, the hopping parameters between neighboring sites fall off exponentially, i.e. going along the chain corresponds to accessing decreasing energy scales in the calculation.

In this way, Wilson achieved a non-perturbative description of the full crossover from a free impurity spin at high temperatures to a screened spin at low temperatures [39], thus solving the so-called Kondo problem as discussed in detail in [20]. After that the investigation of the single-impurity Anderson model [40], which extends the Kondo model by including charge fluctuations at the impurity site was performed. The technical details can be found in [41, 42]

In the following, the development of the NRG concentrated on the analysis of more complicated impurity models, involving either more environment or impurity degrees of freedom. The numerical calculations for these (e.g. two-channel) models are much more cumbersome because the Hilbert space grows by a factor 16 in each step of the iterative diagonalization, instead of the factor 4 in the single-channel case.

The two-impurity Kondo model as paradigm for the competition of local Kondo screening and non-local magnetic correlations was studied with NRG by [43, 44, 45]. Here, the focus was on the question, if the two regimes are connected by a quantum-phase transition or rather by a smooth crossover. Later on, such studies were extended to the two-channel situation [46].

Originally, the NRG was used to determine thermodynamic properties of quantum impurity systems. The calculation of dynamic quantities with the NRG started with the $T = 0$ absorption and photoemission spectra of the x-ray Hamiltonian [47, 48], followed by the $T = 0$ single-particle spectral function for the orbitally non-degenerate and degenerate Anderson model [49, 50]. The resulting spectral functions are obtained on all energy scales, with a resolution proportional to the frequency. Calculation of finite-temperature spectral functions $A(\omega, T)$ are more problematic since all excitations can, in principle, contribute.

Nevertheless, the NRG has been shown to give accurate results for $A(\omega, T)$, which also allows to calculate transport properties [51]. A subsequent development is the introduction of the concept of the reduced density matrix, which allows to calculate dynamic quantities in equilibrium in the presence of external fields [52]. The calculation of non-equilibrium transient dynamics requires a multiple-shell NRG procedure [53] and has been accomplished with the aid of a complete basis set and the reduced density matrix [54]. The first applications of this approach show very promising results, both for fermionic and bosonic systems [54, 55]. Another recent generalization of the NRG approach is its application to quantum impurities coupled to a bosonic bath [56].

There is no restriction on the structure of the impurity part of the Hamiltonian; it might contain, for example, a Coulomb repulsion of arbitrarily large strength. The bath, however, is required to consist of non-interacting fermions or bosons, otherwise the various mappings described below cannot be performed.

Basically all the NRG applications use the following scheme:

a) Division of the bath spectral function into a set of logarithmic intervals in energy.
b) Reduction of the continuous spectrum to a discrete set of states (logarithmic discretization).
c) Mapping of the discretized model onto a semi-infinite chain.
d) Iterative diagonalization of this chain.
e) Further analysis of the many-particle energies, matrix elements, etc., calculated during the iterative diagonalization. This yields information on static and dynamic properties of the quantum impurity model.

Parts a),b) and c) of this strategy are sketched in Fig. 2.1. The NRG discretization parameter Λ defines a set of discretization points, $\pm\Lambda^{-n}$, $n = 0, 1, 2, \ldots$, and a corresponding set of intervals. The continuous spectrum in each of these intervals (see Fig. 2.1 a) is approximated by a single state (see Fig. 2.1 b). The resulting discretized model is mapped onto a semi-infinite chain with the impurity (filled circle) corresponding to the first site of this chain. Due to the logarithmic discretization, the hopping matrix elements decrease exponentially with distance from the impurity, $t_n \propto \Lambda^{-n/2}$ [20].

Quite generally, a numerical diagonalization of Hamiltonian matrices allows to take into account the various impurity-related terms in the Hamiltonian, such as a local Coulomb repulsion, non-perturbatively. Apparently, the actual implementation of such a numerical diagonalization scheme requires some sort of discretization of the original model, which has a continuum of bath states.

The quantum impurity model in the semi-infinite chain form is solved by iterative diagonalization, which means that in each step of the iterative scheme one site of the chain is added to the system and the Hamiltonian matrices of the enlarged cluster are diagonalized numerically. As already pointed out, without taking further steps to reduce the size of the Hilbert space this procedure would have to end for chain sizes of ≈ 10. Here the renormalization group concept enters the procedure through the dependence of the hopping matrix elements on the chain length, $t_n \propto \Lambda^{-n/2}$. Adding one site to the chain corresponds to decreasing the relevant energy scale by a factor $\sqrt{\Lambda}$. Furthermore, because the coupling t_n to the newly added site falls off exponentially, only states of the shorter chain within a comparatively small energy window will actually contribute to the states of the chain with the additional site. This observation allows to introduce a very simple truncation scheme: after each step only the lowest lying N_s many-particle states are

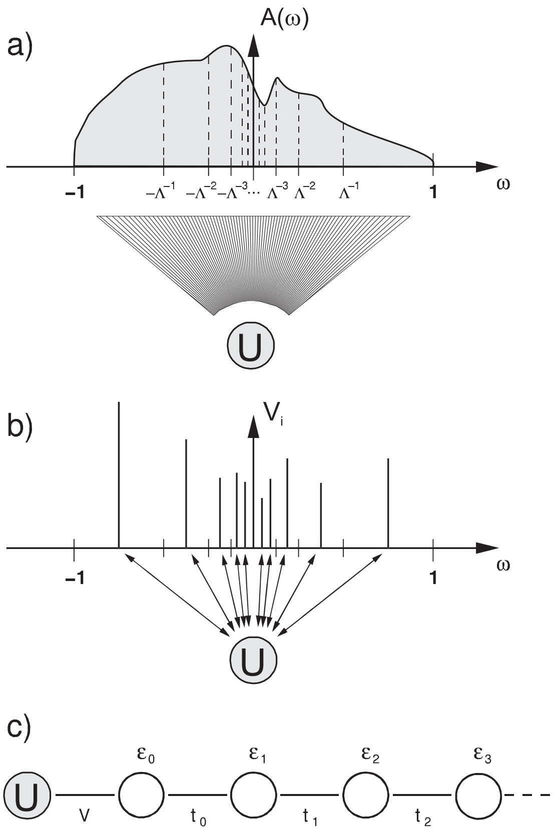

Figure 2.1: Initial steps of the NRG illustrated for the single-impurity Anderson model in which an impurity (filled circle) is coupled to a continuous conduction band with the spectral function $A(\omega)$; a) a logarithmic set of intervals is introduced through the NRG discretization parameter Λ; b) the continuous spectrum within each of these intervals is approximated by a single state with corresponding weight; c) the resulting discretized model is mapped onto a semi-infinite chain where the impurity couples to the first conduction electron site via the hybridization V; the parameters of the tight-binding model (see Ref. [21] for technical details). The figure is adapted from [21].

retained and used to build up the Hamiltonian matrices of the next iteration step, thus keeping the size of the Hilbert space fixed as one walks along the chain.

However this method also has some limitations of applicability. Since the logarithmic discretization is a principal feature of NRG this scheme accurately takes into account only the small vicinity of Fermi level. For systems with flat DOS of free electrons it works perfectly but all the fine features of bath DOS apart the Fermi level are taken into account with less precision. Another problem is, that during the NRG procedure one throws away the highest bath states that can lead to wrong spectrum of high-energy excitations.

2.2.3 Quantum Monte Carlo; Hirsch-Fye method

The quantum Monte Carlo (QMC, for review see [57]) scheme is the most universal tool for the numerical study of quantum many-body systems with strong correlations. So-called determinantal quantum Monte Carlo (QMC) scheme for fermionic systems appeared more than 20 years ago [58, 59, 60, 61]. This scheme became nowadays standard for the numerical investigation of physical models with strong interactions, as well as for the quantum chemistry and nanoelectronics. Although the first numerical attempts were made for a model Hamiltonians with local interaction, the real systems are described by the many-particle action of a general form. For example many non-local matrix elements of the Coulomb interaction do not vanish in the problems of quantum chemistry [62] and solid state physics [63]. For realistic description of Kondo impurities like cobalt atom on metallic surface it is of crucial importance to use the spin and orbital rotationally invariant Coulomb vertex in the non-perturbative investigation of electronic structure. The recently developed Dynamical Mean-Field theory (DMFT, see Chapter 5 and Ref. [3]) for correlated materials involves a non-trivial frequency-dependent bath Green function, and its extension [64] deals with an interaction that is non-local in time. Moreover, the same frequency dependent single-electron Green-function and retarded electron-electron interaction naturally appear in any electronic subsystems where the rest of system is integrated out.

The determinantal grand-canonical auxiliary-field scheme [58, 59, 60, 61] is extensively used for the interacting fermions, since other known QMC schemes (like stochastic series expansion in powers of Hamiltonian [65] or worm algorithms [66]) are suffering from sign problem for this case.

The following two points are essential for the Hirsch-Fye determinantal QMC approach: first, the imaginary time is artificially discretized, and the Hubbard-Stratonovich transformation [67] is performed to decouple the fermionic degrees of freedom. After the decoupling, fermions can be integrated out, and Monte Carlo sampling should be performed in the space of auxiliary Hubbard-Stratonovich fields. Hirsch [60] proposed a so-called discrete Hubbard-Stratonovich transformation to improve the efficiency of original scheme. It is worth to note that for a system of N atoms the number of auxiliary field scales $\propto N$ for the local (short-range) interaction and as N^2 for the long-range one. This makes the calculation rather ineffective for the non-local case. In fact the scheme is developed for the local interaction only.

The one band the single-site impurity model is specified by the imaginary time effective action

$$S_{\text{eff}} = -\int_0^\beta d\tau d\tau' \sum_\sigma c_\sigma^\dagger(\tau)\,\mathcal{G}_\sigma^{-1}(\tau-\tau')c_\sigma(\tau') + \int_0^\beta d\tau U n_\uparrow(\tau) n_\downarrow(\tau), \tag{2.18}$$

$$\mathcal{G}_\sigma^{-1}(i\omega) = i\omega + \mu - \Delta_\sigma(i\omega), \tag{2.19}$$

where $c_\sigma^\dagger(\tau), c_\sigma(\tau)$ are Grassmann variables, μ denotes the chemical potential, U is on-site repulsion and $\Delta_\sigma(i\omega)$ is a hybridization function that describes transitions into the bath and back. The task of the impurity solver is to compute the Green function

$$G(\tau-\tau') = \langle T_\tau c^\dagger(\tau) c(\tau')\rangle_{S_{\text{eff}}} = \frac{Tr\left[T_\tau e^{-S_{\text{eff}}} c^\dagger(\tau) c(\tau')\right]}{Tr\left[T_\tau e^{-S_{\text{eff}}}\right]} \tag{2.20}$$

for a given hybridization function.

The algorithm of Hirsch and Fye [26] requires a discretization of imaginary time into N slices $\Delta\tau = \beta/N$. In each time slice, the four-fermion term $Un_\uparrow n_\downarrow$ is decoupled using a discrete Hubbard-Stratonovich transformation:

$$e^{-\Delta\tau U n_\uparrow n_\downarrow + (\Delta\tau U/2)(n_\uparrow + n_\downarrow)} = \frac{1}{2}\sum_{s=\pm 1} e^{\lambda s (n_\uparrow + n_\downarrow)}, \tag{2.21}$$

where the parameter λ is defined as $\lambda = arccosh(e^{\Delta\tau U/2})$.

The Gaussian integral over the fermion fields may then be performed analytically, yielding an expression for the partition function of the form

$$Z = \sum_{\{s_i\}} \det\left[D_\uparrow(s_1,...,s_N)\right] \det\left[D_\downarrow(s_1,...,s_N)\right]. \tag{2.22}$$

Here, $D_\sigma(s_1,...,s_N)$ denotes the $N \times N$ matrix of the inverse propagator $\mathcal{G}^{-1}$ for a particular configuration of the auxiliary Ising spin variables $s_1,\ldots,s_N$ [3]. The Monte Carlo sampling then proceeds by local updates in these spin configurations. Each successful update requires the calculation of the new determinants in Eq. (2.22), at a computational cost of $O(N^2)$.

The problem with this approach is the highly non-uniform time-dependence of the (metallic) Green functions at low temperature and strong interactions. The initial drop of the Green function

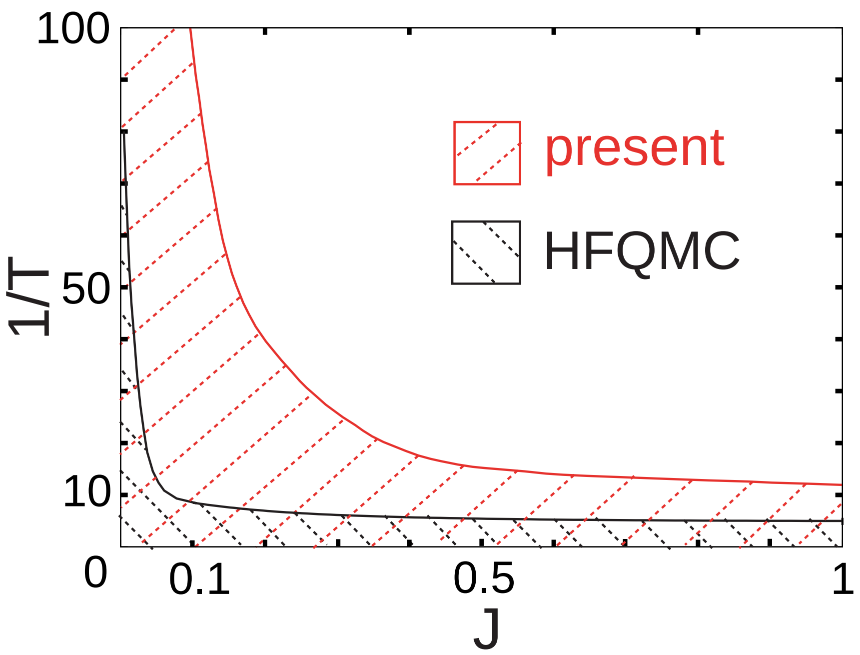

Figure 2.2: Computable regions (hatched) in the T-J parameter space that can be computed with advanced Hirsch-Fye method present in [72] and with conventional Hirsch-Fye QMC (from Ref. [73]) for the two-orbital Hubbard model with $U' = 4\ eV$ and bandwidth $W = 2\ eV$. T and J are in eV. From Ref. [72].

is essentially $\sim e^{-U\tau/2}$, from which it follows that a fine grid spacing $N \sim \beta U$ is required for sufficient resolution. As noted in Ref. [68] a resolution of at least $N = 5\beta U$ is typically needed to get systematic errors below the statistical errors of a reasonably accurate simulation.

At half filling, the matrices $D_\uparrow$ and $D_\downarrow$ are proportional and following (2.22) one can see that the Hirsch-Fye algorithm under these conditions does not suffer from a sign problem in single-orbital case. In fact, a closer analysis reveals that the sign problem is absent for any choice of μ for single-orbital impurity problem [69]. Two-orbital extension of QMC was first done by M. Rozenberg [70]. The general multiorbital QMC formalism for DMFT calculation proposed by [71]. All the mentioned above QMC schemes were using simplified interaction part of Hamiltonian containing only terms of density-density form. Including of spin-flips and pair hoppings terms to these schemes lead to sign problem (or significant reducing of allowable parameter range). Finally some improvements have been done [72], and it became possible to take into account spin-flip terms in 3-orbital AIM. However this algorithm has very limited applicability (see Fig. 2.2).

The most hampering problem arises from the time discretization: One has to take a large enough number of time slices N, or in practice to check that the results are unchanged when N is increased, which is costly since the computation time increase approximately like N^3.

The problem of systematic error due to the time discretization was addressed in several works. For bosonic quantum systems, continuous time loop algorithm [74], worm diagrammatic world line Monte Carlo scheme [66] and continuous time path-integral QMC [75] overcame this issue. Recently a continuous-time modification of the fermionic QMC algorithm was proposed [76]. It is based on a series expansion for the partition function in the powers of interaction. The scheme is free of time-discretization errors, but the Hubbard-Stratonovich transformation is still invoked. Therefore the number of auxiliary fields scales similarly to the discrete scheme, so that the scheme remains local.

Moreover the fact that the imaginary time Green function is given on discrete set of points leads to another problem: to make in continuous one has to use splines. However that for this technique to be precise, one needs to supplement the discrete Green function by the value of its derivatives at $\tau = 0, \beta$, which can be reduced to a linear combination of two–particle correlation functions computed by the QMC calculation [77]. Failure to deal with this problem accurately can lead in some calculations to large errors.

Another problem is connected to the way of discretization of the bare Green function: if a computation is made far from the particle-hole symmetric case, the Weiss function $\mathcal{G}$ can be very steep close to $\tau = 0$ or $\tau = \beta$. As a result, it is not well sampled by the regular mesh time discretization, leading to potentially large numerical error. A simple practical solution is to replace $\mathcal{G}_0$ by $\bar{\mathcal{G}}_0^{-1}(i\omega_n) \equiv \mathcal{G}_0^{-1}(i\omega_n) - \alpha$ where α is a diagonal matrix chosen as $\alpha_{\mu\mu} = \lim_{\omega\to\infty}(\mathcal{G}_0^{-1})_{\mu\mu}(\omega)$. The new impurity problem is equivalent to the initial one, if the α term (which is quadratic in d and diagonal in the indices) is simultaneously added to the interaction (or equivalently to the right hand side of the corresponding decoupling formula). In the new impurity problem however $\bar{\mathcal{G}}_0$ is less steep than $\mathcal{G}_0$ close to $\tau = 0$ or $\tau = \beta$, so the numerical error introduced by discretization is less important. The similar problem appears even in the particle-hole symmetric case if the temperature is low and U is larger than the bandwidth: the $\mathcal{G}(\tau)$ becomes very steep close to $\tau = 0, \tau = \beta$ and in almost all interval $[0, \beta]$ it has a very small values. To overcome this circumstance one can use Projective QMC [78]. The main idea of this method is the following: the non-interacting Green function $\mathcal{G}(\tau, \tau')$ is truncated to $0 \le \tau, \tau' \le \theta$, where θ is cut-off parameter. It means that we have all the time slices exactly in the most important region of $\mathcal{G}(\tau,\tau')$ function. Then the limit $\theta \to \infty$ is taken and the result for ground state is obtained, so it is a zero-temperature method. This method was actively discussed [79, 80] but found to be completely applicable for the half-filled systems. Nevertheless some problems related to Anderson nonorthogonality catastrophe can appear in non-half-filled case [79].

Recently, a new class of continuous-time QMC impurity solvers (CT-QMC) has been developed [81, 68, 82]. These methods do not suffer from the problems mentioned above. Both these diagrammatic QMC approaches rely on an expansion of the partition function into diagrams and the resummation of diagrams into determinants. A local update Monte Carlo procedure is then used to sample these determinants stochastically. The two approaches are complementary in the sense that the weak coupling method [81] uses a perturbation expansion in the interaction part, while the hybridization expansion method [68, 82] treats the local interactions exactly and expands in the impurity-bath hybridization. In the weak-coupling case, the determinantal formulation, which eliminates or at least greatly alleviates the sign problem, originates from Wick's theorem. In the hybridization expansion, when starting from a Hamiltonian formulation, the determinants emerge naturally from the trace over the bath states [82]. The CT-QMC scheme will be described in section 2.3.

2.3 Continuous time quantum Monte Carlo solver

2.3.1 Perturbation expansion

Recently, A. Rubtsov proposed a new approach for solving quantum impurity models [81]. That continuous-time method is a diagrammatic QMC algorithm which can be regarded as an extension of ideas originally introduced in Ref. [66] to fermionic systems. The algorithm is based on a diagrammatic expansion of the partition function in the interaction term and a stochastic sampling of the resulting diagrams (see Fig. 2.3). This scheme is suitable for non-local time-dependent interaction, but in this section we shall discuss only the simplest case: one-site impurity model with the local in time interaction term of the form $Un_{\uparrow}(\tau)n_{\downarrow}(\tau)$. The action (2.18) can be splitted into two parts: unperturbed action S_0 of a Gaussian form

$$S_0 = -\int_0^\beta d\tau d\tau' \sum_\sigma c^\dagger_\sigma(\tau)\mathcal{G}_\sigma^{-1}(\tau-\tau')c_\sigma(\tau') \tag{2.23}$$

and an interaction part

$$S_{int} = \int_0^\beta d\tau U n_\uparrow(\tau) n_\downarrow(\tau). \tag{2.24}$$

The weak coupling expansion of $Z = TrT_\tau e^{-(S_0+S_{int})}$ in powers of U then reads

$$\begin{aligned} Z &= \sum_k \frac{(-1)^k}{k!} \int d\tau_1 \dots d\tau_k TrT_\tau e^{-S_0} \\ &\quad \times U^k n_\uparrow(\tau_1) n_\downarrow(\tau_1) ... n_\uparrow(\tau_k) n_\downarrow(\tau_k). \end{aligned} \tag{2.25}$$

Wick's theorem leads to $2k!$ terms for each perturbation order, and their combined weight is the determinant of the matrix product $D_\uparrow(\tau_1,...,\tau_k)D_\downarrow(\tau_1,...,\tau_k)$. The (i,j) element of these $k \times k$ matrices can be found using the mean field function (2.19)

$$D_\sigma^{i,j} = \mathcal{G}_\sigma(\tau_i - \tau_j). \tag{2.26}$$

Notice, that the perturbation order (and, as a consequence the M_σ matrix size) for different spins can be different in both weak-coupling and strong-coupling approaches. In this section this dependence is omitted for simplicity. Then the partition function reads

$$Z = \sum_k \frac{(-U)^k}{k!} \int d\tau_1 \dots d\tau_k \det\left[D_\uparrow\right] \det\left[D_\downarrow\right] \tag{2.27}$$

and the Monte Carlo sampling proceeds by local updates (random insertions/removals of vertices). At first sight, it appears that the term $(-U)^k$ would lead to a bad sign problem for repulsive interactions. A. Rubtsov found a way to get around this problem by redefining the interaction term S_{int} with a small negative constant α as

$$\begin{aligned} S_{int}^\alpha &= \frac{U}{2} \int d\tau \Big[(n_\uparrow(\tau) - \alpha)(n_\downarrow(\tau) - (1-\alpha)) \\ &\quad + (n_\uparrow(\tau) - (1-\alpha))(n_\downarrow(\tau) - \alpha) \Big] \end{aligned} \tag{2.28}$$

and the quadratic term S_0 in a way to compensate for this change [81]. The detailed description of this procedure is presented in sec. 2.3.4.

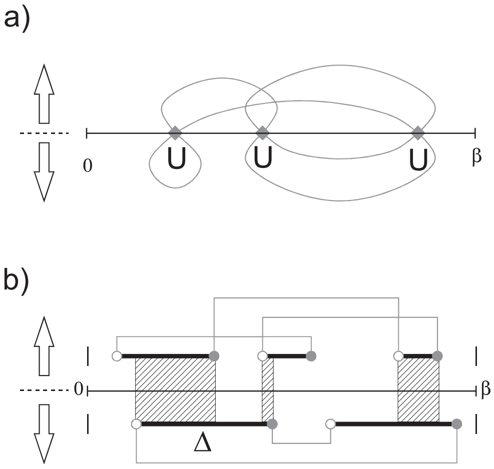

Figure 2.3: Illustration of the diagrams generated by the continuous-time impurity solvers. a) Weak-coupling method: third order diagram consisting of three vertices (diamonds) $Un_\uparrow(\tau)n_\downarrow(\tau)$ linked by lines representing the function $\mathcal{G}_\sigma(\tau_i-\tau_j)$. b) Hybridization expansion method: here, the orders of the diagrams for up- and down-spins can be different. Each creation operator $c^\dagger_\sigma(\tau_s)$ (empty dot) is connected to an annihilation operator $c_\sigma(\tau_e)$ (full dot) by a line representing the hybridization function $\Delta_\sigma(\tau_e-\tau_s)$. The black lines correspond to a particle number 1, empty spaces to particle number 0, so the overlaps between the lines for up- and down-spins yield the potential energy. In both approaches, the diagrams corresponding to different connecting $\mathcal{G}$ or Δ lines are summed up into a determinant and these determinants are sampled by a Monte Carlo procedure [83]. The figure is adapted from Ref. [83].

Strong coupling continuous-time algorithm (see Fig. 2.3) is obtained by expanding in the hybridization functions Δ_σ, while treating the chemical potential and interaction terms exactly. This approach has been worked out in Refs. [68, 82]. For the hybridization expansion, one decomposes the effective action (2.18) into the hybridization part

$$S_\Delta = -\int_0^\beta d\tau d\tau' \sum_\sigma c_\sigma(\tau)\Delta_\sigma(\tau-\tau')c^\dagger_\sigma(\tau') \tag{2.29}$$

and the local part

$$S_L = \sum_\sigma \int_0^\beta d\tau c^\dagger_\sigma(\tau)\left(\frac{\partial}{\partial\tau}-\mu\right)c_\sigma(\tau) + U\int_0^\beta d\tau n_\uparrow(\tau)n_\downarrow(\tau). \tag{2.30}$$

Expanding the partition function $Z = TrT_\tau e^{-(S_\Delta + S_L)}$ in powers of Δ_σ leads to

$$\begin{aligned} Z &= TrT_\tau e^{-S_L} \prod_\sigma \sum_k \frac{1}{k!} \int_0^\beta d\tau_1 ... d\tau_k \int_0^\beta d\tau'_1 ... d\tau'_k \\ &\times \Big[c_\sigma(\tau_1) \Delta_\sigma(\tau_1 - \tau'_1) c^\dagger_\sigma(\tau'_1) \dots \\ &\dots c_\sigma(\tau_k) \Delta_\sigma(\tau_k - \tau'_k) c^\dagger_\sigma(\tau'_k) \Big]. \end{aligned} \tag{2.31}$$

The individual terms in this series can have positive or negative sign, but as shown in Ref. [68], it is possible to express the combined weight of the $k!$ diagrams corresponding to a given set $\{c^\dagger_\sigma(\tau'_i), c_\sigma(\tau_i)\}_{i=1,...,k}$ of creation and annihilation operators as the determinant of a matrix $M_{F,\sigma}$, whose entries are the Δ-functions,

$$M^{i,j}_{F,\sigma} = \Delta_\sigma(\tau_i - \tilde{\tau}_j). \tag{2.32}$$

The partition function finally reads

$$\begin{aligned} Z &= TrT_\tau s_{T_\tau} e^{-S_L} \prod_\sigma \sum_{k_\sigma} \int_0^\beta d\tau'_1 \int_{\tau'_1}^\beta d\tau_1 \dots \\ &\dots \int_{\tau'_{k-1}}^\beta d\tau'_k \int_{\tau'_k}^{\circ\tau'_1} d\tau_k \det D_{F,\sigma}\, s_\sigma \\ &\times c_\sigma(\tau_k) c^\dagger_\sigma(\tau'_k) \dots c_\sigma(\tau_1) c^\dagger_\sigma(\tau'_1), \end{aligned} \tag{2.33}$$

where $\circ\tau$ denotes an upper integral bound which ”winds around” the circle of length β. If the last segment winds around, the sign s_σ is -1 and otherwise $+1$, whereas s_{T_τ} compensates for any sign change produced by the time ordering operator. The trace finds an easy and intuitive interpretation in terms of configurations of segments marking the times where a particle of spin σ is present [68]. In such a representation, the μ-part of S_L is determined by the total length of the segments while the interaction is given by the total overlap between segments of opposite spin (see Fig. 2.3).

On Fig. 2.4 one can see the advantage of both CT-QMC methods over Hirsch-Fye one. However Hybridization expansion method scales slower with lowering the temperature (for performance comparison between theese methods see Ref. [83]). But it is very nontrivial to use the hybridization expansion method in case of multi-orbital impurity. At the moment this solver has been extended to 2-orbital model [82] a complex way that involves explicit trace over $\{c^\dagger_\sigma(\tau'_i), c_\sigma(\tau_i)\}_{i=1,...,k}$ operators (2.33), whereas in the weak-coupling CT-QMC method the extension to multi-orbital problems can be done straightforward way (see section 2.3.3). With

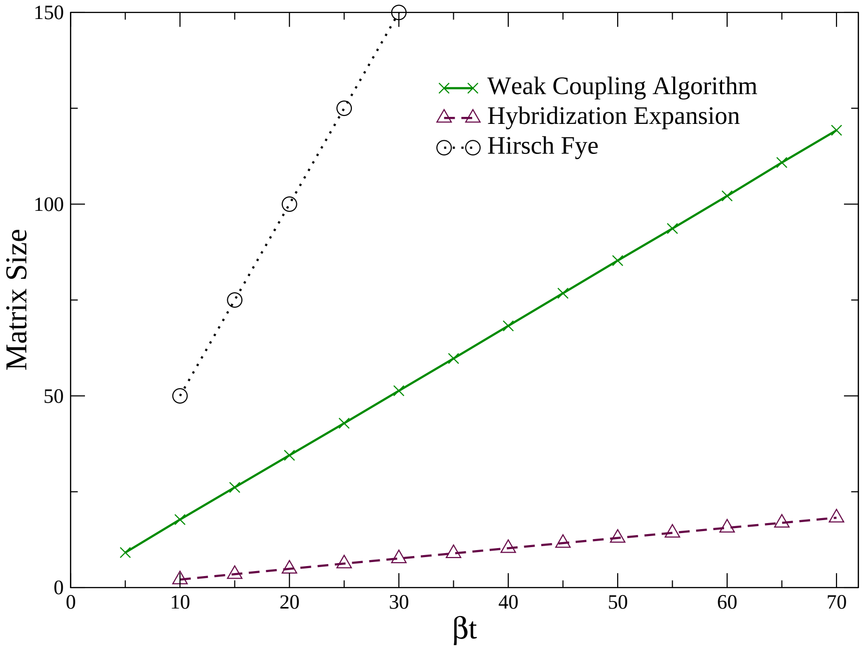

Figure 2.4: Scaling of the matrix size with inverse temperature and interaction strength. Temperature dependence for $U/t = 4$. In the case of Hirsch-Fye, the resolution $N = \beta U$ has been chosen as a compromise between reasonable accuracy and acceptable speed, while the average matrix size is plotted for the continuous-time solvers [83]. From Ref. [83].

regard to the main aim of this work, namely developing and application of multi-orbital impurity solver, we shall use weak coupling CT-QMC method.

2.3.2 Weak coupling CT-QMC, detailed description

As far as the weak coupling CT-QMC method is the most simple to be extended to the multiorbital systems, we shall use it as the main method in our study. In this section we start to describe this method in details.

First we consider the one-orbital model with on-site interaction that is non-local in time: $U^{\tau_1'\tau_2'}_{\tau_1\tau_2} c^\dagger(\tau_1')c(\tau_1)c^\dagger(\tau_2')c(\tau_2)$. We have no explicit spin indices here, but effectively the first pair of operators $c^\dagger(\tau_1')c(\tau_1)$ corresponds to one spin specie and $c^\dagger(\tau_2')c(\tau_2)$ to another one [81].

Then the partition function (2.25) reads:

$$Z=\sum_{k=0}^{\infty}Z_k=\sum_{k=0}^{\infty}\int_0^{\beta}d\tau_1\int_0^{\beta}d\tau_1'...\int_0^{\beta}d\tau_{2k}\int_0^{\beta}d\tau_{2k}'\Omega_k(\tau_1,\tau_1',...,\tau_{2k},\tau_{2k}'), \tag{2.34}$$
$$\Omega_k=Z_0\frac{(-1)^k}{k!}U_{\tau_1\tau_2}^{\tau_1'\tau_2'}...U_{\tau_{2k-1}\tau_{2k}}^{\tau_{2k-1}'\tau_{2k}'}D_{\tau_1'\tau_2'...\tau_{2k}'}^{\tau_1\tau_2...\tau_{2k}}.$$

Here $Z_0=\mathrm{Tr}\,(Te^{-S_0})$ is the partition function for the unperturbed system and

$$D_{\tau_1'...\tau_{2k}'}^{\tau_1...\tau_{2k}}=<Tc^{\dagger}(\tau_1')c(\tau_1)...c^{\dagger}(\tau_{2k}')c(\tau_{2k})> \tag{2.35}$$

is a fermionic determinant. Hereafter the triangle brackets denote the average over the unperturbed system: $<A>=Z_0^{-1}\mathrm{Tr}(TAe^{-S_0})$. Since S_0 is Gaussian, one can apply Wick theorem to decouple the average (2.35). Thus similar to Eq. (2.19) $D_{\tau_1'...\tau_{2k}'}^{\tau_1...\tau_{2k}}$ is a determinant of $2k\times 2k$ matrix which consists of the bare two-point Green functions $\mathcal{G}(\tau',\tau)=<Tc^{\dagger}(\tau')c(\tau)>$:

$$D^{(2k)}\equiv D_{\tau_1'\tau_2'...\tau_{2k}'}^{\tau_1\tau_2...\tau_{2k}}=\det|\mathcal{G}(\tau_i',\tau_j)| \tag{2.36}$$

Now we can express the interacting two-point Green function for the system (2.18) using the perturbation series expansion (2.34). It reads:

$$G(\tau',\tau)\equiv Z^{-1}<Tc^{\dagger}(\tau')c(\tau)e^{-W}>=Z^{-1}\sum_k\int d\tau_1\int d\tau_1'...\int d\tau_{2k}'G^{(2k)}(\tau',\tau)\Omega_k(\tau_1,\tau_1',...,\tau_{2k}') \tag{2.37}$$

where $G^{(2k)}(\tau',\tau)$ denotes the Green function for a current term of series:

$$G^{(2k)}(\tau',\tau)=\frac{<Tc^{\dagger}(\tau')c(\tau)c^{\dagger}(\tau_1')c(\tau_1)...c^{\dagger}(\tau_{2k}')c(\tau_{2k})>}{<Tc^{\dagger}(\tau_1')c(\tau_1)...c^{\dagger}(\tau_{2k}')c(\tau_{2k})>}$$

This is nothing else that the ratio of two determinants: $D^{(2k+1)}/D^{(2k)}$. Similarly, one can write formulas for other averages, for example the two-particle Green function which is related to four-point correlation functions and contains important information about magnetic excitations (see sec. 2.3.5):

$$\chi(\tau,\tau',\tau'',\tau''')\equiv Z^{-1}<Tc^{\dagger}(\tau')c(\tau)c^{\dagger}(\tau''')c(\tau'')e^{-W}>$$
$$=Z^{-1}\sum_k\int d\tau_1\int d\tau_1'...\int d\tau_{2k}'\chi^{(2k)}(\tau,\tau',\tau'',\tau''')\Omega_k(\tau_1,\tau_1',...,\tau_{2k}'), \tag{2.38}$$

where

$$\chi^{(2k)}(\tau,\tau',\tau'',\tau''') = \frac{< Tc^\dagger(\tau')c(\tau)c^\dagger(\tau''')c(\tau'')c^\dagger(\tau'_1)c(\tau_1)...c^\dagger(\tau'_{2k})c(\tau_{2k}) >}{< Tc^\dagger(\tau'_1)c(\tau_1)...c^\dagger(\tau'_{2k})c(\tau_{2k}) >}$$

is the ratio of two determinants: $D^{(2k+2)}/D^{(2k)}$.

An important property of the above formulas is that the integrands stay unchanged under the permutations $\tau_i,\tau_{i'},\tau_{i+1},\tau_{i'+1} \leftrightarrow \tau_j,\tau_{j'},\tau_{j+1},\tau_{j'+1}$ with any i,j. Therefore it is possible to introduce a quantity K, which we call ”state of the system” and that is a combination of the perturbation order k and an unnumbered set of k points. Now, denote $\Omega_K = k!\Omega_k$, where the factor $k!$ reflects all possible permutations of the arguments. For the Green functions, $k!$ in the nominator and denominator cancel each other, so that $G_K = G_k$. In this notation

$$Z = \int \Omega_K D[K], \tag{2.39}$$

$$\tag{2.40}$$

$$G(\tau',\tau) = Z^{-1}\int G_K\Omega_K D[K],$$

where $\int D[K]$ means the summation over k and integration over all possible realizations of the above-mentioned unnumbered set at each k.

The important notice is that the series expansion for an exponent *always* converges for the finite fermionic systems. Mathematically rigorous proof can be constructed for the Hamiltonian systems. Indeed, many-body fermionic Hamiltonians H_0 and W have a finite number of eigenstates that is 2^N_{orb}, where N_{orb} is the total number of electronic orbitals in the system. Now one can observe that $\Omega_k < const \cdot W^k_{max}$, where W_{max} is the eigenvalue of W with a maximal modulus. This proofs a convergence of (2.34), because $k!$ in the denominator grows faster than the nominator. In calculations for the non-Hamiltonian systems, no indications of divergence were observed [81].

Although formula (2.39) looks rather formal, it exactly corresponds to the idea of the proposed QMC scheme. A Markov random walk in a space of all possible K is performed. A probability density to visit each state is $P_K \propto |\Omega_K|$. If such a simulation is organized, one can extract the sign of each term:

$$G(\tau',\tau) = \overline{sG(\tau',\tau)}/\bar{s}$$

Overline here means a Monte Carlo averaging over the random walk, and $\bar{s} = \overline{\Omega_K/|\Omega_K|}$ is an average sign. Two kinds of the trial steps are necessary: one should try either to increase or to

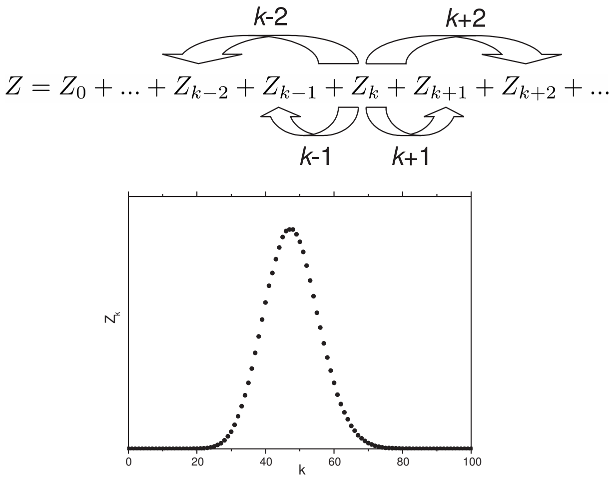

Figure 2.5: Schematic picture of random walks in the space of perturbation order k according to perturbation series expansion (2.34) (upper panel) and an example of the histogram for the perturbation order k (lower panel). From Ref. [81]

.

decrease k by 1, and, respectively, to add or to remove the corresponding tetrad of "coordinates". Then the standard Metropolis acceptance criterion can be constructed using the ratio

$$\frac{||w||}{k+1} \cdot \left| \frac{D^{2k+2}}{D^{2k}} \right| . \tag{2.41}$$

for the incremental steps and its inverse for the decremental ones.

In general, one may want also to add-remove several tetrades simultaneously. Thus organized random walk is illustrated by Fig. 2.5, upper panel. The lower panel of the figure presents a typical distribution diagram for a perturbation order k in the QMC calculation.

The most time consuming operation of the algorithm is a calculation of the ratio of determinants and Green-function matrix. It's necessary for calculation of MC weights as well as for Green function. There exist so called fast-update formulas for calculation of the ratio of determinants and Green-function matrix. Usual procedure takes N^3 operations, while the fast-update technique allows one to perform N^2 or less operations, where N is a matrix size. Usually, the two considered types of steps ($k \to k+1$ and $k \to k-1$) are sufficient. However, the steps $k \to k \pm 2$ can be also employed in certain cases and is useful for two-particle Green functions.

The only matrix which one need to keep during MC steps is the inverse matrix of the bare Green functions: $M_{(2k)} = g_{(2k)}^{-1}$. In the following formulae matrix $M_{(2k)}$ is extended to be $(2k+$

$1) \times (2k+1)$ matrix with $M_{2k+1,2k+1} = 1$ and $M_{2k+1,i} = 0$, $M_{i,2k+1} = 0$, which does not change the ratio of determinants.

It is easy to obtain fast-update formulas for the step $k \to k+1$. The expressions for the matrix $M^{(2k+1)}$ has the following form [81]:

$$M_{(2k+1)} = \begin{pmatrix} \cdots & \cdots & \cdots & -L_{1,2k+1}\lambda^{-1} \\ \cdots & M'_{i,j} & \cdots & \cdots \\ \cdots & \cdots & \cdots & -L_{2k,2k+1}\lambda^{-1} \\ -\lambda^{-1}R_{2k+1,1} & \cdots & -\lambda^{-1}R_{2k+1,k} & \lambda^{-1} \end{pmatrix}$$

where $M'_{i,j} = M^{(2k)}_{i,j} + L_{i,2k+1}\lambda^{-1}R_{2k+1,j}$, $R_{i,j} = \sum_n g_{i,n}M^{(2k)}_{n,j}$ and $L_{i,j} = \sum_n M^{(2k)}_{i,n}g_{n,j}$ and λ is equal to the ratio of two determinants:

$$\frac{\det D_{(2k+1)}}{\det D_{(2k)}} = g_{2k+1,2k+1} - \sum_{i,j=1}^{2k} g_{2k+1,i}M^{(2k)}_{i,j}g_{j,2k+1} = \lambda.$$

For the step $k \to k-1$ (remove of the column and row n) the fast update formulas for matrix $M^{(2k-1)}$ and the ratio of determinants are as follows:

$$M^{(2k-1)}_{i,j} = M^{(2k)}_{i,j} - \frac{M^{(2k)}_{i,n}M^{(2k)}_{n,j}}{M^{(2k)}_{n,n}}, \tag{2.42}$$
$$\frac{\det D_{(2k-1)}}{\det D_{(2k)}} = M^{(2k)}_{n,n}.$$

One can also obtain fast-update formulas in the same manner for steps ±2 [81]. Let's introduce a 2×2 matrix λ:

$$\lambda_{q,q'} = g_{q,q'} - \sum_{i,j=1}^{2k} \mathcal{G}_{q,i}M^{(2k)}_{i,j}\mathcal{G}_{j,q'}, \tag{2.43}$$

where $\{q,q'\} = 2k+1, 2k+2$. Then, for example, the ratio of two determinants is equal to

$$\frac{\det D_{(2k+2)}}{\det D_{(2k)}} = \det|\lambda|.$$

Using the fast update formula for M [81], the Green function can be obtained both in imaginary time and at Matsubara frequencies:

$$G(\tau,\tau') = \mathcal{G}(\tau,\tau') - \sum_{i,j} \mathcal{G}(\tau,\tau_i) M_{i,j} \mathcal{G}(\tau_j,\tau') \tag{2.44}$$

$$G(\omega) = \mathcal{G}(\omega) - \mathcal{G}(\omega) \left[\frac{1}{\beta} \sum_{i,j} M_{i,j} e^{i\omega(\tau_i - \tau_j)} \right] \mathcal{G}(\omega). \tag{2.45}$$

Here $\mathcal{G}(\tau',\tau)$ and $\mathcal{G}(\omega)$ are the bare Green functions in imaginary time and Matsubara frequencies correspondingly.

2.3.3 Multiorbital formalism

The impurity action (2.18) can be rewritten in the general multiorbital form with general time-independent Coulomb interaction the following way:

$$\begin{aligned} S_{imp} = S_0 + S_{int} = & - \sum_{ij\sigma} \int_0^\beta \int_0^\beta c^\dagger_{i\sigma}(\tau) \mathcal{G}^{-1}_{ij}(\tau - \tau') c_{j\sigma}(\tau') d\tau d\tau' \\ & + \frac{1}{2} \sum_{ijkl\sigma\sigma'} \int_0^\beta U_{ijkl} c^\dagger_{i\sigma}(\tau) c^\dagger_{j\sigma'}(\tau) c_{k\sigma'}(\tau) c_{l\sigma}(\tau) d\tau, \end{aligned} \tag{2.46}$$

where i,j,k,l are orbital indices, σ,σ' - spin indices, $\mathcal{G}_{ij}$ local non-interacting Green function for correlated orbitals and U_{ijkl} is Coulomb interaction matrix element:

$$U_{ijkl} = \langle i_1 j_2 | V^{ee}_{12} | k_2 l_1 \rangle \tag{2.47}$$

here $i_1 \equiv \psi_i(\mathbf{r}_1)$ is local orthogonal wave function for correlated orbitals and V^{ee}_{12} is screened spin-independent Coulomb pair interaction between electrons at the coordinates $\mathbf{r}_1$ and $\mathbf{r}_2$. We used standard quasiatomic LDA+U parametrization of Coulomb matrix for d-electron via effective Slater parameters [15] or equivalently via two parameters: screened Coulomb integral U and Hund exchange integral J, keeping ratio of multipole parameters equal to atomic values [15]. We choose the orbital basis related to spherical harmonics to be sure that magnetic orbital quantum number in U_{ijkl} matrix satisfied the following sum roule: $i+k = j+l$. In this case we will get rid of so-called three site terms like U_{ijkk} with $i \neq j$ which produce a large sign problem in the case of real cubic harmonics. For details of construction of the interaction part see sec. 4.2.

Following the general idea of the weak coupling CT-QMC [81] we expand the partition function around the Gaussian part of our multiorbital action (2.46):

$$\frac{Z}{Z_0} = \sum_n \frac{(-1)^n}{n!2^n} \sum_{\{ijkl\sigma\sigma'\}} \int_0^\beta d\tau_1 ... \int_0^\beta d\tau_n \left\langle U_{i_1 j_1 k_1 l_1} c^\dagger_{i_1\sigma_1} c^\dagger_{j_1\sigma'_1} c_{k_1\sigma'_1} c_{l_1\sigma_1} ... U_{i_n j_n k_n l_n} c^\dagger_{i_n\sigma_n} c^\dagger_{j_n\sigma'_n} c_{k_n\sigma'_n} c_{l_n\sigma_n} \right\rangle_0 ,$$

where we define the average over Gaussian part of the action as:

$$\langle ... \rangle_0 = Z_0^{-1} \int D[c^\dagger c] ... e^{S_0}.$$

The integrating over the Gaussian action gives the fermionic determinant over the non-interacting Green functions with the rank $2n$:

$$\frac{Z}{Z_0} = \sum_n \frac{(-1)^n}{n!2^n} \sum_{\{ijkl\sigma\sigma'\}} \int_0^\beta d\tau_1 ... \int_0^\beta d\tau_n U_{i_1 j_1 k_1 l_1} ... U_{i_n j_n k_n l_n} \det \mathcal{G}^{2n\times 2n}. \tag{2.48}$$

In order to minimize the number of different interaction vertices we group the different matrix elements of multiorbital Coulomb interaction which have the similar structure of fermionic operators. Since U_{ijkl} matrix elements are spin independent, to generate all terms for the interaction in the action (2.46), one should look over all possible combinations of orbital and spin indices. Some combinations can violate the Pauli principle and should not be taken into account. For CT-QMC algorithm it is useful to transfer interaction part in the following form: $U_{ijkl} c^\dagger_{i\sigma} c_{l\sigma} c^\dagger_{j\sigma'} c_{k\sigma'}$.

The interaction terms can be transformed to the desired form, depending on relations between spin and orbital indices:

a) if $\sigma \neq \sigma'$, we can just commute $c_{l\sigma}$ and $c_{k\sigma'}$ and then $c_{l\sigma}$ and $c^\dagger_{j\sigma'}$. Another combination of indices, that allows the same commutation, is the following: $\sigma = \sigma'$, $i \neq j$ and $k \neq l$ (the later is following from the Pauli principle), and also $j \neq l$. These terms we can transform to the following desirable representation:

$$H_{int1} = U_{ijkl} c^\dagger_{i\sigma} c_{l\sigma} c^\dagger_{j\sigma'} c_{k\sigma'}. \tag{2.49}$$

b) in the case when $\sigma = \sigma'$ and $j = l$ we can commute $c_{k\sigma'}$ and $c^{\dagger}_{j\sigma'}$, since in this case $i \neq j$ and $k \neq l$ due to the Pauli principle:

$$H_{int2} = -U_{ijkl} c^{\dagger}_{i\sigma} c_{k\sigma} c^{\dagger}_{j\sigma} c_{l\sigma} \tag{2.50}$$

After generating all this terms it is necessary *symmetrize* all the terms with equivalent quantum numbers (for example, $U_{ijkl} c^{\dagger}_{i\sigma} c_{j\sigma} c^{\dagger}_{k\sigma'} c_{l\sigma'}$ and $U_{klij} c^{\dagger}_{k\sigma'} c_{l\sigma'} c^{\dagger}_{i\sigma} c_{j\sigma}$). Then all the procedures described in sec. 2.3.2 are performed without any modifications and Green functions of interacting system can be extracted from the M matrix similar to (2.46):

$$G_{ij}(\tau, \tau') = \mathcal{G}_{ij}(\tau, \tau') - \sum_{n,m}^{K} \mathcal{G}_{ij_n}(\tau, \tau_n) M_{n,m} \mathcal{G}_{i_m j}(\tau_m, \tau') \tag{2.51}$$

$$\tag{2.52}$$

$$G_{ij}(\omega) = \mathcal{G}_{ij}(\omega) - \frac{1}{\beta} \sum_{n,m}^{K} \mathcal{G}_{ij_n}(\omega) M_{n,m} e^{i\omega(\tau_n - \tau_m)} \mathcal{G}_{i_m j}(\omega), \tag{2.53}$$

where i, j are orbital indices and n, m are running indices corresponding to summation over all the perturbation orders up to the current one K. The indices j_n and i_m denotes orbital numbers corresponding to the part of interaction field containing imaginary time point τ_n and τ_m respectively.

2.3.4 Sign problem. Choice of α parameters

In order to reduce and in many cases avoid the sign problem in CT-QMC, we introduce additional quantities α, which can be in principle a function of time, spin and number of lattice site (orbital). Thus up to an additive constant we have the new separation of the action (2.46), see Ref. [81]:

$$S_0 = \sum_{ij\sigma} \int_0^{\beta} \int_0^{\beta} \left(-\mathcal{G}^{-1}_{ij}(\tau - \tau') + \frac{1}{2} \sum_{\{kl\sigma'\}} \alpha^{\sigma'}_{kl} (U_{ilkj} + U_{lijk}) \delta_{\tau\tau'} \right) c^{\dagger}_{i\sigma} c_{j\sigma} d\tau d\tau' \ , \tag{2.54}$$

$$\tag{2.55}$$

$$S_{int} = \frac{1}{2} \sum_{\{ijkl\sigma\sigma'\}} \int_0^{\beta} U_{ijkl} (c^{\dagger}_{i\sigma} c_{l\sigma} - \alpha^{\sigma}_{il})(c^{\dagger}_{j\sigma'} c_{k\sigma'} - \alpha^{\sigma'}_{jk}) d\tau.$$

One can see, that the first item of (2.54) in Matsubara space corresponds to bare Green's function

$$\mathcal{G}^{-1}_{ij} = (i\omega_n + \mu)\, \delta_{ij} - \Delta_{ij}(\omega_n), \tag{2.56}$$

here Δ is hybridization matrix. The second term is just a constant which we can absorb to the new chemical potential $\tilde{\mu}$. Therefore we can rewrite the bare Green function in the following matrix form:

$$\tilde{\mathcal{G}}^{-1} = (i\omega_n + \tilde{\mu})\,\mathbf{1} - \Delta. \tag{2.57}$$

The optimal choice of prarmeters α^{σ}_{ij} would lead to effective reduction of interaction terms in the action Eq. (2.54) and minimization of average perturbation oder in Eq. (2.48).

Using the fact that $U_{ilkj} = U_{lijk}$ following from the definition of the Coulomb matrix elements (2.47) and Eq. (2.54), the relation between $\tilde{\mathcal{G}}$ and $\mathcal{G}$ can be represented in the following spin and orbital matrix form:

$$\tilde{\mathcal{G}}^{-1} = \mathcal{G}^{-1} - \left\langle \hat{\alpha}\hat{U} \right\rangle. \tag{2.58}$$

Now we can discuss a simple system: 1-band isolated ($\Delta = 0$) Hubbard atom at half-filling. In order to arrive half-filling in interacting system the chemical potential should be $\mu = U/2$. Thus the bare Green function (2.56) at U of order of bandwidth have an occupancy close to 1. (figures with 2 types of chem. potential, $\mathcal{G}(\tau)$) It leads to difficulties with numerical evaluating of $\mathcal{G}(\tau)$, because on almost all the segment $[0,\beta]$ it has very small values and all the details of initial bath DOS become concentrated in small vicinities of $\tau = 0$ and $\tau = \beta$. Since we use uniformal sampling of τ points in $[0,\beta]$ range, accumulating of sufficient number of points near $\tau = 0$ and $\tau = \beta$ takes unreasonable long time. Therefore from computational reasons we should keep the occupancy of bath Green function unchanged.

In this case we need to put the many-body chemical potential not to the bath Green function but into the interaction part of Hamiltonian. In order to do this we have to choose the α in a propper parameters. For the concerned case of isolated Hubbard atom at half-filling we can put $\alpha_1 + \alpha_2 = 1$, that give us (According to (2.58)) $\tilde{\mu} = 0$ for half-filled case at any U because of cancellation of μ in $\mathcal{G}^{-1}$ and $\left\langle \hat{\alpha}\hat{U} \right\rangle = (\frac{\alpha_1+\alpha_2}{2})U = \frac{U}{2}$, that corresponds to half-filling. However the simplest choice $\alpha_1 = \alpha_2 = \frac{1}{2}$ leads to rejecting of steps $k \pm 1$ since the ratio of correspondent determinants is exactly zero.

We also need to minimize the fermionic sign problem which finally lead us to such expression for diagonal alpha's parameters:

$$\alpha^{ii}_{\sigma} + \alpha^{jj}_{\sigma'} = \bar{\alpha} \tag{2.59}$$

where $\bar{\alpha}$ has to be found iteratively in order to get a proper occupation number of correlated electrons. In the case of half-filled one-band Hubbard model $\bar{\alpha} = 1$ leads to the correct chemical potential shift of the $\frac{U}{2}$ and average $\alpha = \frac{1}{2}$ which corresponds to the Hartree-Fock substraction. The diagonal alpha corresponds to the following interaction fields $U_{ijji} n_{i\sigma} n_{j\sigma'}$. For non-diagonal alpha's which corresponds to the fields of general form $U_{ijkl} c^{\dagger}_{i\sigma} c_{l\sigma} c^{\dagger}_{j\sigma'} c_{k\sigma'}$, where $i \neq l$ and $j \neq k$ we find the following optimal condition:

$$\alpha^{ij}_{\sigma} + \alpha^{kl}_{\sigma'} = 0 \tag{2.60}$$

Since we symmetrize the interaction U matrix it is needed to extend the definition of $\hat{\alpha}$ matrix in order to keep all the terms in the interaction part of initial action (the last item in Eq. (2.54)). It can be done the following way [81, 84]: for every U_{ijkl} field in 50% of updates we deliver the α parameters as

$$\alpha^{il} = \alpha_{diag}, \;\; \alpha^{jk} = \bar{\alpha} - \alpha_{diag},$$

and in another 50% as

$$\alpha^{il} = \bar{\alpha} - \alpha_{diag}, \;\; \alpha^{jk} = \alpha_{diag}$$

for the case of $i = l$ and $j = k$. For non-diagonal fields, i.e. $i \neq l$ and $j \neq k$

$$\alpha^{il} = \alpha_{nd}, \;\; \alpha^{jk} = -\alpha_{nd},$$

with 50% probablility and

$$\alpha^{il} = -\alpha_{nd}, \;\; \alpha^{jk} = \alpha_{nd}$$

otherwise. It was found that the sign problem is eliminated in the case when $\alpha_{diag} < 0$ and $\bar{\alpha} \geq 1$ for occupancy $n \geq \frac{1}{2}$ per orbital and $\alpha_{diag} > 0$, $\bar{\alpha} < 1$ otherwise. The optimal choice of $|\alpha_{diag}|$ parameter is few percent of $|\bar{\alpha}|$ to keep minimal average perturbation order. Another problem is a proper choice of non-diagonal α_{nd} parameter. It is easy to see that α_{nd} is proportional to acceptance probability of non-diagonal field in the case where the bare green function $\mathcal{G}_{jk} = 0$. Since these processes are unphysical, the natural choice is $\alpha_{nd} = 0$. But it leads to division on zero in the updating the inverse Green function matrix [81]. On the other hand increasing α_{nd} parameter cause the sign problem. We find the reasonable choice of α_{nd} to be of the order of 10^{-4}. Moreover for some special cases like atomic limit, where $\mathcal{G}_{mm}(\tau) = 0.5$ a small noise should be added to all the α parameters to avoid numerical divergency.

If it is not the case (for example if the choice of α parameters described in (2.59) and (2.60) leads to the sign problem in some particular form of interaction part of Hamiltonian) the bare Green function is corrected according to (2.61).

For the general choice of the α parameters the corresponding new bare Green function can be written in the following schematic form:

$$\tilde{\mathcal{G}}^{-1} = (i\omega_n + \tilde{\mu}) - \Delta - \left\langle \left(\hat{\alpha} - \overline{\alpha}\hat{1}\right) \hat{U} \right\rangle . \tag{2.61}$$

If we choose the α parameters in the above mentioned optimal way, then the last term in Eq. (2.61) vanish automatically.

2.3.5 Four-point correlators

The most interesting quantity for spin systems is the magnetic susceptibility. Studying it give us insight to low temperature behavior of correlated impurities and other physically interesting systems.

Let us consider the behavior of impurity model in magnetic field. The z-component of the magnetization operator is given by

$$M_{tot} = M_a + M_c = -g\mu_B(S_z + s_z), \tag{2.62}$$

where g is Lande factor (it is the same for impurity and bath electrons), M_{tot} is total system magnetization, M_a and M_c – magnetization of the impurity and band electrons respectively, S_z s_z are correspondingly z-components of the spin operator on impurity and the spin of the band electrons:

$$S_z = \frac{1}{2}(n_{a\uparrow} - n_{a\downarrow}), \;\; s_z = \int d\mathbf{r} s_z(\mathbf{r}), \tag{2.63}$$

$$n_{a\sigma} = a^{\dagger}_{\sigma} a_{\sigma}, \tag{2.64}$$

where $a^{\dagger}_{\sigma}$ and a_{σ} are creation and annihilation operators acting on impurity state respectively, σ denotes spin. The definition of total susceptibility χ_{tot} of the system in homogeneous magnetic field $\mathbf{B}$ is the following [20]:

$$\chi_{tot} = \frac{d}{dB} \langle M_{tot} \rangle \bigg|_{B=0} = \chi_a + \chi_c, \tag{2.65}$$

$$\chi_a = \frac{d}{dB} \langle M_a \rangle \bigg|_{B=0}, \tag{2.66}$$

$$\chi_c = \frac{d}{dB} \langle M_c \rangle \bigg|_{B=0}, \tag{2.67}$$

where M_a is the impurity magnetization and M_c is a magnetization of conduction electrons, χ_a and χ_c are corresponding susceptibilities. Note, that χ_c is not a susceptibility of pure system without impurity. The susceptibility of the system of free electrons without impurity

$$\chi_{pure} \equiv \chi_c^0 = \frac{d}{dB} \left\langle M_c \right\rangle_{pure} \Big|_{B=0} \tag{2.68}$$

is just a Pauli susceptibility of pure metal. Therefore the spin susceptibility due to impurity χ_{imp} can be expressed as a difference between susceptibility of the complete system and the Pauli one:

$$\chi_{imp} = \chi_{tot} - \chi_{pure} = \chi_a + \chi_c - \chi_c^0, \tag{2.69}$$

where The total susceptibility χ_{tot} can be obtained by the linear response theory [85]. One can show that χ_a and χ_c can be expressed by retarded spin-spin correlation functions:

$$\chi_a = -(g\mu_B)^2 \left[\chi_{aa}^{(R)}(\omega = 0) + \chi_{ac}^{(R)}(\mathbf{k} = 0, \omega = 0) \right], \tag{2.70}$$

$$\chi_c = -(g\mu_B)^2 \left[\chi_{cc}^{(R)}(\mathbf{k} = 0, \mathbf{k}' = 0, \omega = 0) + \chi_{ca}^{(R)}(\mathbf{k} = 0, \omega = 0) \right], \tag{2.71}$$

where $\chi^{(R)}$ - are results of the Fourier transform of the following retarded response functions:

$$\chi_{aa}^{(R)}(t - t') = -i\theta(t - t') \left\langle \left[S_z(t), S_z(t') \right] \right\rangle, \tag{2.72}$$

$$\chi_{ac}^{(R)}(\mathbf{k}, t - t') = -i\theta(t - t') \sqrt{\Omega} \left\langle \left[S_z(t), s_z(\mathbf{k}, t') \right] \right\rangle, \tag{2.73}$$

$$\chi_{ca}^{(R)}(\mathbf{k}, t - t') = -i\theta(t - t') \sqrt{\Omega} \left\langle \left[s_z(\mathbf{k}, t), S_z(t') \right] \right\rangle, \tag{2.74}$$

$$\chi_{cc}^{(R)}(\mathbf{k}, \mathbf{k}', t - t') = -i\theta(t - t') \Omega \left\langle \left[s_z(\mathbf{k}, t), s_z(\mathbf{k}', t') \right] \right\rangle. \tag{2.75}$$

Here $s_z(\mathbf{k})$ is - Fourier transform of the spin density $s_z(\mathbf{r})$, and Ω is volume of the system. Because the statistical averages in (2.72)-(2.75) are taken without external fields, the averages are commutators of the spin operators in Heisenberg representation. It is known that retarded response functions can be obtained as analytical continuation of a corresponding temperature correlation functions [33].

So the local property of the impurity is $chi_{aa} \equiv \chi_{\mathrm{loc}}$, which is proportional to the local correlation function of the impurity spin. The susceptibility has a smooth temperature dependence (see e.g. Fig. 3.10). For a system with constant band DOS (flat-band) χ_{loc} coincides with the impurity susceptibility, χ_{imp}, which is obtained as the difference between the susceptibility of the electron system with the impurity and without it (see Eq. (2.69) and Ref. [39]). Wilson defined the Kondo temperature as the crossover temperature where $T_K\chi_{\text{imp}}(T_K) = 0.0701$ [39, 86]. For the system with strongly non-constant band DOS, e.g. disordered system, $T\chi_{\text{imp}}(T)$ can strongly deviate from the universal scaling curve of the clean system [87]. It turns out, however, that this is an artefact of the definition of χ_{imp}, since the susceptibility of the electronic system fluctuates strongly and can result in negative values of χ_{imp} [88]. Therefore, we use instead the local static magnetic susceptibility, $\chi_{\text{loc}} \equiv \chi_{aa}$. The temperature response function in imaginary time reads

$$\chi_{aa}(\tau) = \chi_{loc}(\tau) = \langle T_\tau S^z(\tau) S^z(0)\rangle, \tag{2.76}$$

where T_τ is time ordering operator. In Matsubara space it has the following form:

$$\chi_{loc}(i\omega_B) = \int_0^\beta e^{i\omega_B\tau}\chi_{loc}(\tau)d\tau, \tag{2.77}$$

where $\omega_B = 2n\pi/\beta$ is a bosonic Matsubara frequency (n is an integer number, $\beta = 1/k_BT$ - inverse temperature) [85].

Since our method is based on perturbation theory with expansion in powers of interaction, the magnetic susceptibility can be expressed as an expansion in powers of H_{int}. For example the $\langle S_z S_z\rangle$ correlator according to (2.63) can be expanded the following way [89, 90]:

$$\begin{aligned}
\langle S_z S_z\rangle &= \frac{1}{Z}\left\langle \frac{1}{4}(n_\uparrow - n_\downarrow)(n_\uparrow - n_\downarrow)\right\rangle \\
&= \frac{1}{\beta}\sum_{n=1}^{\infty}\frac{(-1)^n}{n!}\frac{1}{2}(g\mu_B)^2 U^n \int_0^\beta d\tau_1 \ldots d\tau_{n+2} \\
&\quad \Big[D^{\uparrow}_{n+2}(1,2,\ldots n+2) D^{\downarrow}_{n}(2,3,\ldots n+1) \\
&\quad - D^{\uparrow}_{n+1}(1,2,\ldots n+1) D^{\downarrow}_{n+1}(2,3,\ldots n+2)\Big].
\end{aligned} \tag{2.78}$$

Therefore we have to calculate products of determinants of the form $D_{n+2}D_n$ and $D_{n+1}D_{n+1}$ where the index denotes size of the determinant. But we already can calculate such a ratios of determinants (they are used to perform the fast updates of inverse propagators matrix [81]).

We could start from the definition (2.76), but from the computational point of view it is more convenient to calculate the susceptibilities on Matsubara frequencies. As it was already mentioned in sec. 2.3.2, the CT-QMC method is suitable for calculating not only two-point correlators (local and non-local Green functions) but also four-point correlators of a general form $\chi_{ijkl} = \langle T_\tau c_{i\sigma} c_{j\sigma'} c^\dagger_{k\sigma''} c^\dagger_{l\sigma'''} \rangle$, that contains important information about magnetic excitations in the system:

$$\chi^{rr''}_{r'r'''} \equiv Z^{-1} < T c^\dagger_{r'} c^r c^\dagger_{r'''} c^{r''} > = Z^{-1} \sum_k \int dr_1 \int dr'_1 ... \int dr'_{2k} \chi^{rr''}_{r'r'''}(r_1, r'_1, ..., r'_{2k}) \Omega_k(r_1, r'_1, ..., r'_{2k}), \tag{2.79}$$

where

$$\chi^{rr''}_{r'r'''}(r_1, r'_1, ..., r'_{2k}) = \frac{< T c^\dagger_{r'} c^r c^\dagger_{r'''} c^{r''} c^\dagger_{r'_1} c^{r_1} ... c^\dagger_{r'_{2k}} c^{r_{2k}} >}{< T c^\dagger_{r'_1} c^{r_1} ... c^\dagger_{r'_{2k}} c^{r_{2k}} >}$$

is the ratio of two determinants: $D_{(2k+4)}/D_{(2k)}$ and in principle is equivalent to Eq. (2.78).

Now we consider calculation of the $\chi^{+-}_{loc}(\tau) = \langle T_\tau S^+(\tau) S^-(0) \rangle$ correlation function, where $S^+(\tau) = c^\dagger_\uparrow(\tau) c_\downarrow(\tau)$ and $S^-(\tau) = c^\dagger_\downarrow(\tau) c_\uparrow(\tau)$. We can express the $D_{(2k+4)}/D_{(2k)}$ ratio of determinants by the combination of $D_{(2k+2)}/D_{(2k)}$ terms:

$$\frac{\left\langle c^\dagger_1 c_2 c^\dagger_3 c_4 \dots \right\rangle}{\langle \dots \rangle} = \frac{\left\langle c^\dagger_1 c_2 \dots \right\rangle}{\langle \dots \rangle} \frac{\left\langle c^\dagger_3 c_4 \dots \right\rangle}{\langle \dots \rangle} - \frac{\left\langle c^\dagger_1 c_4 \dots \right\rangle}{\langle \dots \rangle} \frac{\left\langle c^\dagger_3 c_2 \dots \right\rangle}{\langle \dots \rangle}, \tag{2.80}$$

where ”...” is the same set of fermionic operators emerging from the raising of H_{int} in power of the perturbation order. Fourier transforms are determined the following way:

$$G(\omega) = \int_0^\beta G(\tau) e^{-i\omega\tau} d\tau, \tag{2.81}$$

$$G(\tau) = \frac{1}{\beta} \sum_{\omega=-\infty}^{\infty} G(\omega) e^{i\omega\tau} \tag{2.82}$$

for function of one variable and

$$G(\omega,\omega') = \frac{1}{\beta}\int_0^\beta d\tau \int_0^\beta d\tau' G(\tau,\tau') e^{-i\omega\tau + i\omega'\tau'}, \tag{2.83}$$

$$G(\tau,\tau') = \frac{1}{\beta}\sum_{\omega,\omega'=-\infty}^{\infty} G(\omega,\omega') e^{i\omega\tau - i\omega'\tau'} \tag{2.84}$$

for function of two variables. We need it because the ”momentary” Green functions (obtained according to Eq. 2.46, but not averaged over the Monte-Carlo process) used to construct the four-point correlators (see sec. 2.3.6) essentially depends on two variables. Therefore the $\chi^{+-}(\Omega)$ dynamical susceptibility can be calculated on Matsubara frequencies following way [19]:

$$\begin{aligned}
\chi^{+-}(\Omega) &= \frac{1}{\beta}\int_0^\beta d\tau \int_0^\beta d\tau' G_\uparrow(\tau,\tau') G_\downarrow(\tau',\tau) e^{-i\Omega(\tau-\tau')} \\
&= \frac{1}{\beta}\int_0^\beta d\tau \int_0^\beta d\tau' \frac{1}{\beta^2} \sum_{\omega_1,\omega_2,\omega_3,\omega_4=-\infty}^{\infty} G_\uparrow(\omega_1,\omega_2) G_\downarrow(\omega_3,\omega_4) e^{i(\omega_1\tau - \omega_2\tau' + \omega_3\tau') - \omega_4\tau + \Omega\tau - \Omega\tau'} \\
&= \frac{1}{\beta}\sum_{\omega_1,\omega_2=-\infty}^{\infty} G_\uparrow(\omega_1+\Omega, \omega_2+\Omega) G_\downarrow(\omega_2,\omega_1),
\end{aligned} \tag{2.85}$$

Note, that in Eq. (2.85) $G_\sigma(\tau,\tau')$ denotes not the Green function in the commonly used sense but tho ”momentary” product of the $c^\dagger_\sigma(\tau)c_\sigma(\tau')$ operators, that have not been averaged statistically over the Monte-Carlo process. The same way we can derive

$$\chi^{ij}_{loc_{zz}}(\tau) = \langle T_\tau S^i_z(\tau) S^j_z(0)\rangle, \tag{2.86}$$

where

$$S^i_z = \frac{n^i_\uparrow - n^i_\downarrow}{2} \tag{2.87}$$

is operator of the z projection of spin on the i-th orbital. Using the (2.87) definition we can rewrite the average (2.86) in the following form:

$$\langle S^i_z(\tau) S^j_z(\tau')\rangle = \frac{1}{4}\left(\left\langle n^i_\uparrow(\tau) n^j_\uparrow(\tau')\right\rangle + \left\langle n^i_\downarrow(\tau) n^j_\downarrow(\tau')\right\rangle - \left\langle n^i_\uparrow(\tau) n^j_\downarrow(\tau')\right\rangle - \left\langle n^i_\downarrow(\tau) n^j_\uparrow(\tau')\right\rangle\right). \tag{2.88}$$

In this calculation we assume $\tau > \tau'$. Using Eq. (2.80) we can rewrite the items of (2.88) in terms of ”momentary” Green functions:

$$
\begin{aligned}
&\frac{\left\langle n^i_\sigma(\tau) n^j_\sigma(\tau')\ldots\right\rangle}{\langle\ldots\rangle} = \\
&= \frac{\left\langle c^{i\dagger}_\sigma(\tau) c^i_\sigma(\tau)\ldots\right\rangle}{\langle\ldots\rangle}\frac{\left\langle c^{j\dagger}_\sigma(\tau') c^j_\sigma(\tau')\ldots\right\rangle}{\langle\ldots\rangle} - \frac{\left\langle c^{i\dagger}_\sigma(\tau) c^j_\sigma(\tau')\ldots\right\rangle}{\langle\ldots\rangle}\frac{\left\langle c^{j\dagger}_\sigma(\tau') c^i_\sigma(\tau)\ldots\right\rangle}{\langle\ldots\rangle} = \\
&= G^{ii}_\sigma(\tau,\tau) G^{jj}_\sigma(\tau',\tau') - G^{ij}_\sigma(\tau,\tau') G^{ji}_\sigma(\tau',\tau),
\end{aligned}
\tag{2.89}
$$

$$
\frac{\left\langle n^i_\sigma(\tau) n^j_{\bar\sigma}(\tau')\ldots\right\rangle}{\langle\ldots\rangle} = \frac{\left\langle c^{i\dagger}_\sigma(\tau) c^i_\sigma(\tau)\ldots\right\rangle}{\langle\ldots\rangle}\frac{\left\langle c^{j\dagger}_{\bar\sigma}(\tau') c^j_{\bar\sigma}(\tau')\ldots\right\rangle}{\langle\ldots\rangle} = G^{ii}_\sigma(\tau,\tau) G^{jj}_{\bar\sigma}(\tau',\tau'). \tag{2.90}
$$

Using (2.89) and (2.90) we can rewrite (2.88) as

$$
\begin{aligned}
&\langle S^i_z(\tau) S^j_z(\tau')\rangle = \\
= \;\; & \frac{1}{4}\Big(G^{ii}_\uparrow(\tau,\tau) G^{jj}_\uparrow(\tau',\tau') - G^{ij}_\uparrow(\tau,\tau') G^{ji}_\uparrow(\tau',\tau) + G^{ii}_\downarrow(\tau,\tau) G^{jj}_\downarrow(\tau',\tau') - G^{ij}_\downarrow(\tau,\tau') G^{ji}_\downarrow(\tau',\tau) \\
& - G^{ii}_\uparrow(\tau,\tau) G^{jj}_\downarrow(\tau',\tau') - G^{ii}_\downarrow(\tau,\tau) G^{jj}_\uparrow(\tau',\tau')\Big).
\end{aligned}
\tag{2.91}
$$

Finally we can write down $\chi^{ij}_{loc_{zz}}$ in the Matsubara space. To do that, we perform Fourier transform (2.83) of Eq. (2.91):

$$
\begin{aligned}
&\chi^{ij}_{loc_{zz}}(\Omega) = \\
= \;\; & \frac{1}{4\beta}\sum_{\omega_1,\omega_3=-\infty}^{\infty}\Big[G^{ii}_\uparrow(\omega_1,\omega_1+\Omega) G^{jj}_\uparrow(\omega_3,\omega_3-\Omega) + G^{ii}_\downarrow(\omega_1,\omega_1+\Omega) G^{jj}_\downarrow(\omega_3,\omega_3-\Omega) \\
- \;\; & G^{ii}_\uparrow(\omega_1,\omega_1+\Omega) G^{jj}_\downarrow(\omega_3,\omega_3-\Omega) - G^{ii}_\downarrow(\omega_1,\omega_1+\Omega) G^{jj}_\uparrow(\omega_3,\omega_3-\Omega)\Big] \\
- \;\; & \frac{1}{4\beta}\sum_{\omega_1,\omega_2=-\infty}^{\infty}\Big[G^{ij}_\uparrow(\omega_1+\Omega,\omega_2+\Omega) G^{ji}_\uparrow(\omega_2,\omega_1) + G^{ij}_\downarrow(\omega_1+\Omega,\omega_2+\Omega) G^{ji}_\downarrow(\omega_2,\omega_1)\Big].
\end{aligned}
\tag{2.92}
$$

In order to get the dynamical susceptibility (2.92) in this relatively simple form we made some ”shifting” of the running indices (for example, $\omega_3 \to \omega_3 - \Omega$) to reduce the number of variables. We can do it because of translation invariance of time and therefore we have only 3 independent parameters in Fourier transform. The summation in (2.92) is formally done over all the frequencies ω_n, from $n = -\infty$ to $n = \infty$, therefore we can add some constant to the running indices.

2.3.6 Practical implementation of the susceptibilities calculation

To calculate for example dynamical susceptibility $\chi^{+-}(\Omega)$ (2.85) we need 2-frequencies Green functions $G(\omega_i, \omega_j)$. They can be obtained from the $G(\tau, \tau') = \mathcal{G} - \sum_{i,j=0}^{K} \mathcal{G}(\tau, \tau_i) M_{ij} \mathcal{G}(\tau_j, \tau)$ by Fourier transform (2.83). First we calculate the ”exact” part of the susceptibility according to (2.85) (Fig. 2.6, blocks a). Since we have not so many Matsubara frequencies, we need to include asymptotics. The first correction to our result is ”head-tail” contribution (Fig. 2.6, blocks b). Here we have exact values of first ”momentary Green function” and only asymptotics $1/i\omega_n$ for the second one (as we know, the Green functions in Matsubara space have the $1/i\omega_n$ asymptotics at $\omega_n \to \infty$). The tail-tail asymptotics (Fig. 2.6, blocks c) for the positive frequencies is defined as

$$\sum_{n=n_{max}+N+1}^{\infty} \frac{1}{\omega_n} \frac{1}{\omega_{n+N}} = \sum_{n=0}^{\infty} \frac{1}{\omega_n} \frac{1}{\omega_{n+N}} - \sum_{n=0}^{n_{max}+N} \frac{1}{\omega_n} \frac{1}{\omega_{n+N}} = \frac{\beta^2}{8} - \sum_{n=0}^{n_{max}+N} \frac{1}{\omega_n} \frac{1}{\omega_{n+N}}. \tag{2.93}$$

From symmetry reasons we have to add (2.93) twice, because we have a sum over all the Matsubara frequencies ω_n, from $n = -\infty$ to $n = \infty$. Here we used the fact that $\omega_{-n} = -\omega_{n-1}$, if the Matsubara frequencies are defined as $\omega_n = (2n+1)\frac{\pi}{\beta}$. Note that only diagonal (where both frequencies are equal) elements of ”momentary Green functions” have well-defined asymptotics. Moreover, only diagonal elements survive after the averaging of Green function over the Monte-Carlo process.

Finally we compared the CT-QMC results for static susceptibility $\chi^{+-} = \chi^{+-}(\Omega)|_{(\Omega=0)}$ to the exact solution for one-orbital Anderson impurity model in the atomic limit (see Fig. 2.8; analytical solution is derived in Appendix). A good agreement between CT-QMC and exact results within broad temperature range is found. However below some critical temperature the system becomes ”trapped” in one of the local energy minima (in this particular case of one-orbital AIM the impurity just become magnetized) and loose ergodicity. It leads to considerable

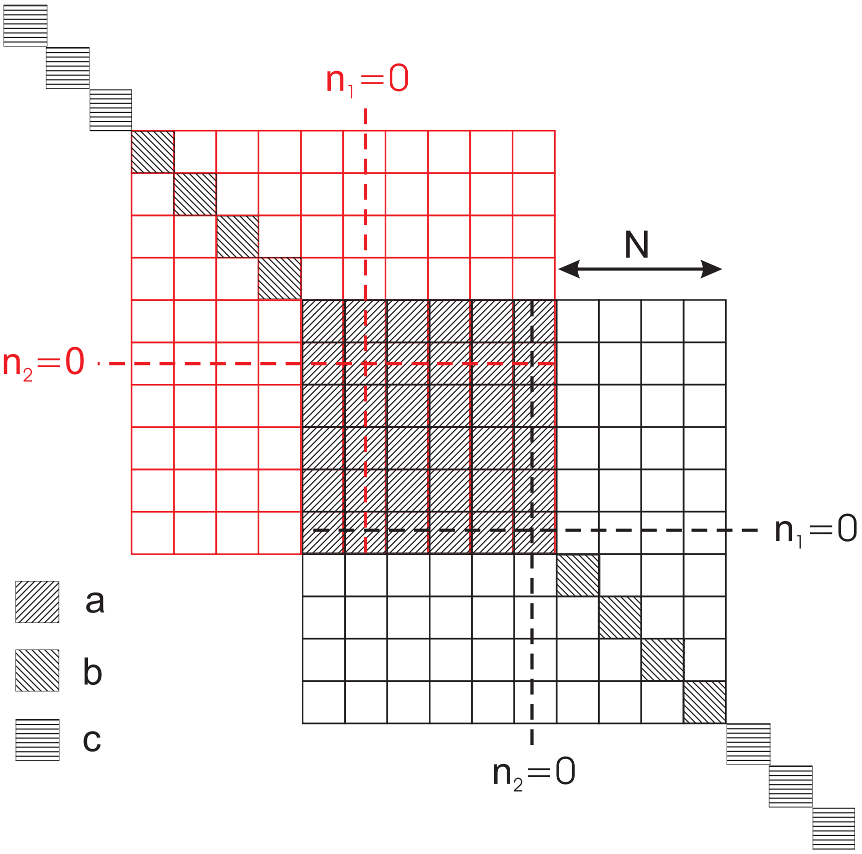

Figure 2.6: Calculation of susceptibility $\chi^{+-}(\Omega)$ (2.85). a - head-head part, calculated exactly; b - head-tail part, unknown diagonal values of Green function supposed to be equal to $1/i\omega_n$; c - tail-tail part calculated analytically according to Eq. (2.93). The indices n_1, n_2 and N corresponds to frequencies ω_1, ω_2 and Ω (see Eq. (2.85)) respectively.

underestimation of the susceptibility, although the statistical error of the QMC process is still quite small.

2.3.7 Analytic continuation

The quantum Monte Carlo simulation yields the Green function in imaginary time $G(\tau)$. For the study of the spectral properties, transport or optics, Green function on real axis are needed and therefore the analytic continuation is necessary. This in practice amounts to solving the following integral equation [22]:

$$G(\tau) = \int d\omega f(-\omega) e^{-\tau\omega} A(\omega), \tag{2.94}$$

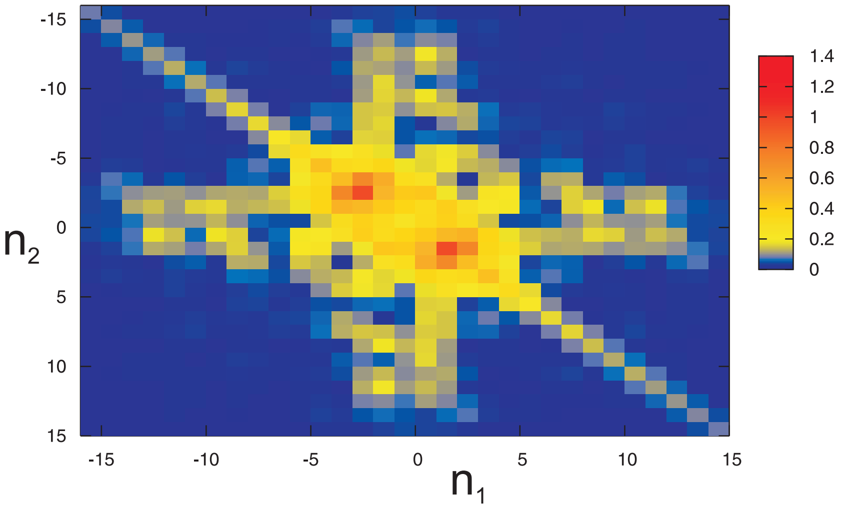

Figure 2.7: Typical form of the module of the ”momentary Green function”. The Kondo model in Abrikosov’s representation (see Chapter 3) is used. The model parameters are: exchange coupling strength $J = -0.2\ eV$, inverse temperature $\beta = 15\ eV^{-1}$, on-site constrain $U_c = 0.5\ eV$. The indices n_1 and n_2 corresponds to frequencies ω_1 and ω_2 (see Eq. (2.85)) respectively.

where $A(\omega)$ is the unknown spectral function, and $f(\omega)$ is the Fermi function. This is a numerically ill-posed problem because $G(\tau)$ is insensitive to the spectral density at large frequencies. Most often this problem is solved using the maximum entropy method (MEM) [91].

A new functional $Q[A]$, which is to be minimized, is constructed as follows

$$Q[A] = \alpha S[A] - \frac{1}{2}\chi^2[A] \tag{2.95}$$

where

$$\chi^2[A] = \sum_{ij=1}^{L} (\bar{G}(\tau_i) - G(\tau_i))[C^{-1}]_{ij}(\bar{G}(\tau_j) - G(\tau_j)) \tag{2.96}$$

measures the distance between the QMC data, averaged over many QMC runs ($\bar{G}_i$) and the Green function $G(\tau_i)$ that corresponds to the given spectral function $A(\omega)$ according to equation Eq. (2.94). The C_{ij} is the covariant matrix containing the information about statistical errors of the QMC data. In A. Sandvik’s algorithm [92] we are using, this is a diagonal matrix. Then Eq. (2.96) can be rewritten as

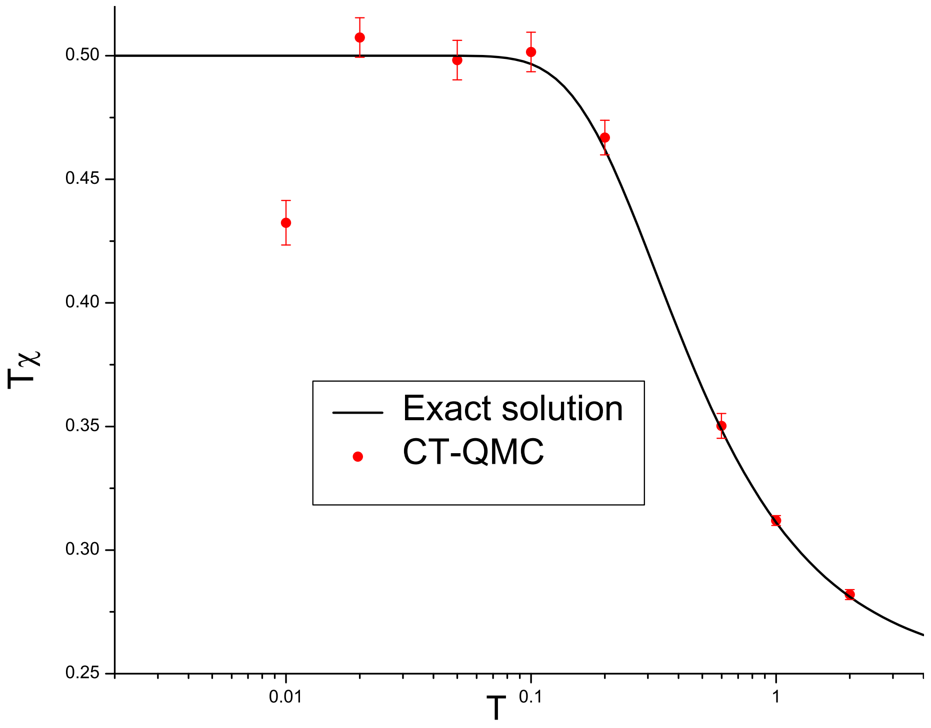

Figure 2.8: Magnetic susceptibility $T\chi^{+-} = T\chi^{+-}(\Omega)|_{(\Omega=0)}$ of one-orbital Anderson impurity model in atomic limit at half-filling. On-site Coulomb repulsion $U = 1\ eV$, $T\chi$ in $(g\mu_B)^2$, T in eV. Comparison of exact solution (solid line) and CT-QMC results (red dots). Error bars denotes statistical error of the QMC process.

$$\chi^2[A] = \sum_{i=1}^{L} (\bar{G}(\tau_i) - G(\tau_i))^2/\sigma_i^2 \tag{2.97}$$

where σ_i^2 is a statistical error of $\bar{G}(\tau_i)$. The entropy term, $S[A]$, takes the form

$$S[A] = \int (A(\omega) - m(\omega) - A(\omega)\ln[A(\omega)/m(\omega)])\,, \tag{2.98}$$

where $m(\omega)$ is the so-called default model, that defines the zero of the entropy and to which the spectrum reduces in the absence of data, in our case it is constant.

For each value of the parameter α, numeric minimization of Q gives as the corresponding spectral function $A^{\alpha}(\omega)$. If α is too large, the solution will not move far from the default model, while small α leads to unphysical oscillations caused by over-fitting the noisy QMC data.

In the so-called historic MEM, the parameter α is chosen such that $\chi^2 = N$, where N is the

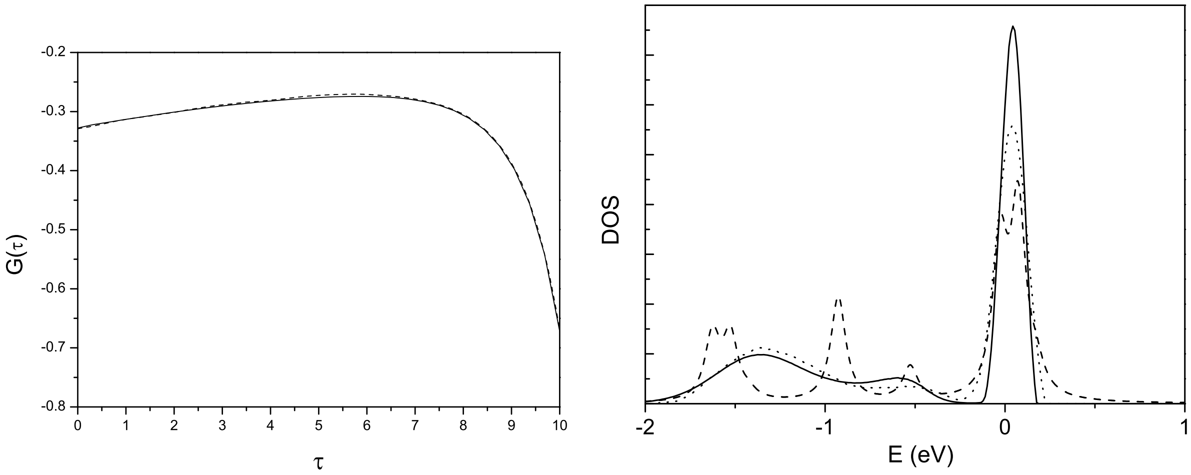

Figure 2.9: Left panel: Green function $G(\tau)$ for 3-orbital degenerated AIM in atomic limit away from half-filling, τ in eV^{-1}. Solid line – CT-QMC, dash – exact diagonalization. Right panel: DOS for 3-orbital degenerated AIM in atomic limit away from half-filling. Solid line – analytical continuation of the CT-QMC, dash line – exact diagonalization results obtained on real energy axis, dot line – analytical continuation of the exact diagonalization results obtained in imaginary time. The model parameters are following: $U = 1\ eV$, $J = 0.3\ eV$, $T = 0.1\ eV$, $\bar{n} = \frac{2}{3}$ pro orbital ($n_{tot} = 4$ electrons).

total number of real frequency points at which $A(\omega)$ is being determined. In many cases, this gives already a reasonable spectral functions, however, in general the historic method tends to underfit the data and makes the resulting $A(\omega)$ too smooth.

In the ”classical” MEM we are using, the parameter α is determined from the following algebraic equation

$$-2\alpha S(\alpha) = Sp\left\{\Lambda(\alpha)\left[\alpha I + \Lambda(\alpha)\right]^{-1}\right\} \tag{2.99}$$

where $S(\alpha)$ is the value of the entropy in the solution A^{α}, which minimizes Q and $\Lambda(\alpha)$ is

$$\Lambda(\alpha)_{ij} = \sqrt{A_i^{\alpha}}\left[K^T C^{-1} K\right]_{ij}\sqrt{A_j^{\alpha}}. \tag{2.100}$$

Here K_{ij} is the discretized kernel $K_{ij} \equiv K(\tau_i, \omega_j)$ and A_i is the discretized spectral function $A_i = A(\omega_i)d\omega_i$ and C_{ij} is the above defined covariant matrix.

In applications of DMFT to real materials, the quasiparticle peak can have a complex structure since at low temperature we need to reproduce renormalized LDA bands around the Fermi-level, i.e., the spectral function approaches the LDA density of states contracted for the quasiparticle renormalization amplitude Z, $A(\omega) = \rho(\omega/Z + \mu_0)$. The MEM has a tendency to smear out this complex structure because of the entropy term.

From practical point of view for obtaining DOS from Green function given on imaginary times or Matsubara frequencies it means the following: MEM gives quite smooth DOS, and (especially at high temperatures) it can overlook fine DOS features, don't resolve peaks if their positions are of order of width, etc. As an example we can use the results of a test for 3-orbital AIM in the atomic limit (see section 4.1). The model parameters are: $U = 1\ eV$, $J = 0.3\ eV$, $T = 0.1\ eV$, $\bar{n} = \frac{2}{3}$ pro orbital. For this case we have exact DOS obtained by exact diagonalization method. The $G(\tau)$ interacting Green function obtained by CT-QMC (solid line) and exact diagonalization (dash line) are presented on Fig. 2.9, left panel. One can see that the results are in good agreement, but not in coincedence. The Fig. 2.9, right panel demonstrates exact DOS of the interacting system (dash line), DOS obtained by MEM from the exact $G(\tau)$ Green function (dot line) and from CT-QMC resulting Green function (solid line).

3 Kondo impurity problem with an arbitrary density of conducting electron states

The numerically exact determinantal continuous time QMC method has been applied to calculate properties of a Kondo impurity coupled to a band of conducting electrons with an arbitrary density of states (DOS). This approach allows to calculate spin susceptibilities as well as Green functions, accurately taking into account all the features of the conducting electron DOS. The method was applied to a Kondo impurity embedded into different environments: ultrasmall grain, Anderson alloy model (lattice with random on-site energy levels) and a two-dimensional lattice, where the DOS has a van Hove singularity. The CT-QMC method was used to check the applicability of Numerical Renormalization Group (NRG) to Kondo impurities embedded into environment with very nonuniformal DOS and to find out how the shape of bath DOS influence on screening of impurity magnetic moment. All the NRG calculations mentioned in the current Chapter were performed by A. Zhuravlev [88].

3.1 Kondo effect

Although the Kondo effect is a well known and widely studied phenomenon in condensed matter physics, it continues to capture the imagination of experimentalists and theorists alike. Interest in the Kondo effect has therefore persisted because it provides clues to understanding the electronic properties of a wide variety of materials where the interactions between electrons are particularly strong, for instance in heavy-fermion materials and high temperature superconductors. In fact, interest in the Kondo effect has recently peaked thanks to new experimental techniques from the rapidly developing field of nanotechnology, which have given us unprecedented control over Kondo systems. The short introduction to the problem can be found in Ref [93].

This effect was discovered in the 1930s [94] while measuring the resistance of gold samples

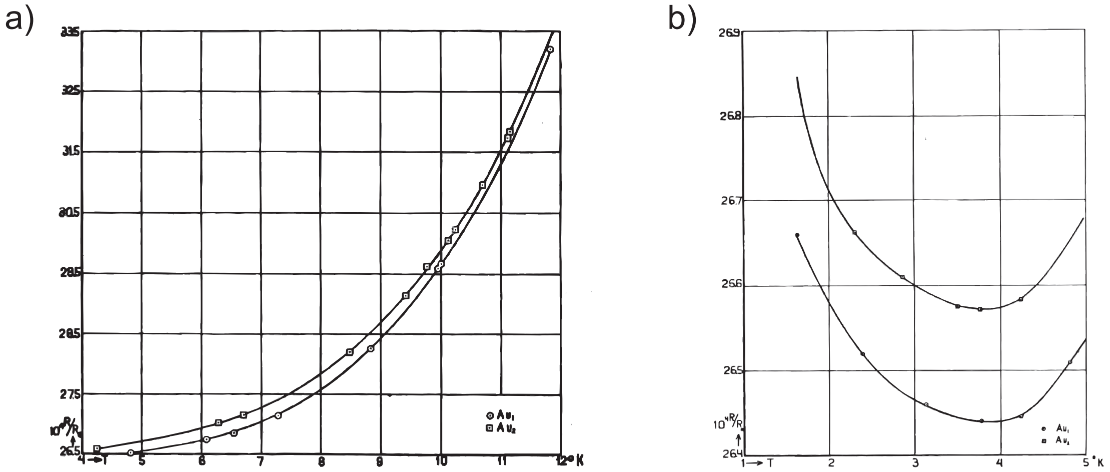

Figure 3.1: Resistance of *Au* at low temperatures. On the right panel the resistance minimum at $T \approx 4\ K$ is shown. The figures were adapted from [94].

at very low (up to 1.63K) temperatures. It was found that with the lowering temperature below some point the resistance start to increase (see Fig. 3.1). The Kondo effect originates from screening of the spin of a magnetic impurity (opened d or f shell of the impurity atom with non-zero total spin of all the electrons) by conduction band electrons of the host metal.

The simplest model of a magnetic impurity, which was introduced by Anderson [40] (see fig. 3.2 a) has only one electron level with energy ε_0. In this picture, the impurity has a spin of $1/2$ and its z-component is fixed as either ”spin up” or ”spin down”. However, so-called exchange processes can take place that effectively flip the spin of the impurity from spin up to spin down, or vice versa, while simultaneously creating a spin excitation in the Fermi sea. Figure 3.2 (a–c) illustrates what happens when an electron is taken from the localized impurity state and put into an unoccupied energy state just above the Fermi level. The energy needed for such a process is large, between about 1 and 10 eV for magnetic impurities. Classically, it is forbidden to take an electron from the impurity without putting energy into the system. In quantum mechanics, however, the Heisenberg uncertainty principle allows such a configuration to exist for a very short time around $h/|\varepsilon_0|$, where h is the Planck constant. Within this timescale, another electron must tunnel from the Fermi sea back towards the impurity. However, the spin of this electron can be opposite to the initial one. This spin exchange qualitatively changes the energy spectrum of the system (fig. 3.2 d) forming a strong peak in the impuritys density of states near the Fermi level [20].

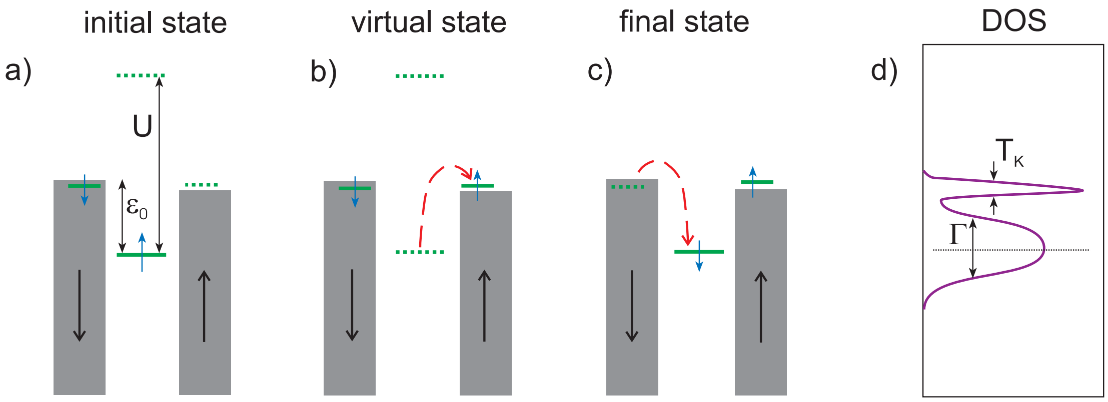

Figure 3.2: The Anderson impurity model assumes that it has one electron level with energy ε_0 below the Fermi energy (a). This level is occupied by one spin-up electron. Adding another electron is prohibited by the Coulomb energy, U, while it would cost at least $|\varepsilon_0|$ to remove the electron. Being a quantum particle, the spin-up electron may tunnel out of the impurity site to briefly occupy a classically forbidden ”virtual state” (b) outside the impurity, and then be replaced by an electron from the metal. This can effectively flip the spin of the impurity (c). Many such events combine to produce the Kondo effect, which leads to the appearance of an extra resonance at the Fermi energy (d). Since transport properties, such as conductance, are determined by electrons with energies close to the Fermi level, the extra resonance can dramatically change the conductance. The figure was adapted from [93]

.

Such a resonance is very effective at scattering electrons with energies close to the Fermi level. Since the same electrons are responsible for the low-temperature conductivity of a metal, the strong scattering contributes greatly to the resistance and leads to increasing the resistance at low temperatures.

This many body resonance also can be observed explicitly using the scanning tunneling spectroscopy (STS) technique: on single magnetic adatoms [95, 96, 97], in artificial nanostructures such as quantum corrals [98], and for molecules [99]. In STS spectra, it shows up as a feature which can be described by a Fano line shape [100, 101, 102]. From a fit, the peak width is obtained which is the characteristic energy scale – the Kondo temperature T_K of the impurity system. For the Kondo scenario of a single magnetic impurity on a nonmagnetic metal surface a simple semi-empirical model has been proposed by P. Wahl et al. [103].

3.2 Abrikosov's representation of the Kondo model

The main difference of the Kondo impurity model to the Anderson one (see Chapter 4) is that the only one electron with spin **S** supposed to occupy the impurity site. Therefore interaction of the impurity with conduction band electrons due to the Heisenberg exchange can be written as $H_{K_{int}} = -2J\mathbf{Ss}$, where **S** is impurity spin and **s** is spin of the conduction band electron. The general description of this model is so-called $s-d$ Hamiltonian [20]:

$$H_{sd} = \sum_{\mathbf{k}\sigma} \varepsilon_{\mathbf{k}} c^{\dagger}_{\mathbf{k}\sigma} c_{\mathbf{k}\sigma} - \sum_{\mathbf{kk'}} J_{kk'} \left[S^{+} c^{\dagger}_{\mathbf{k}\downarrow} c_{\mathbf{k'}\uparrow} + S^{-} c^{\dagger}_{\mathbf{k}\uparrow} c_{\mathbf{k'}\downarrow} + S_z \left(c^{\dagger}_{\mathbf{k}\uparrow} c_{\mathbf{k'}\uparrow} - c^{\dagger}_{\mathbf{k}\downarrow} c_{\mathbf{k'}\downarrow} \right) \right]. \tag{3.1}$$

It describes the single-spin impurity **S** with spin operators S_z and $S^{\pm} = S_x \pm iS_y$, coupled to the band of conduction electrons ($c^{\dagger}_{\mathbf{k}\sigma}$ and $c_{\mathbf{k}\sigma}$ operators) within Heisenberg exchange $J_{kk'}$.

Since the CT-QMC method was originally designed for fermionic systems i.e. systems, where Wick theorem takes place (for Gaussian action), we use the fermionic description of Kondo problem. Following approach of Wilson [39] we approximate the $J_{kk'}$ exchange by the constant J, but keep exact DOS from conduction electron spectrum $\varepsilon_{\mathbf{k}}$. To use this method for Kondo systems we replace spin operators to fermionic one by Abrikosov's transformation [104]:

$$S^{+} = a^{\dagger}_{\uparrow} a_{\downarrow},\ \ S^{-} = a^{\dagger}_{\downarrow} a_{\uparrow},\ \ S_z = \frac{1}{2}(a^{\dagger}_{\uparrow} a_{\uparrow} - a^{\dagger}_{\downarrow} a_{\downarrow}). \tag{3.2}$$

Therefore in fermionic operators the interaction part of $s-d$ Hamiltonian (3.1) reads

$$\begin{aligned} H_{Ab} = & \quad -2J(S^z s^z + 1/2(S^{+} s^{-} + S^{-} s^{+})) \\ = & \quad -J/2 \left[(n^a_{\uparrow} n^c_{\uparrow} + n^a_{\downarrow} n^c_{\downarrow}) + (n^a_{\uparrow} n^c_{\downarrow} + n^a_{\downarrow} n^c_{\uparrow}) \right. \\ & \quad \left. + 2(a^{\dagger}_{\uparrow} c_{\uparrow} c^{\dagger}_{\downarrow} a_{\downarrow} + c^{\dagger}_{\uparrow} a_{\uparrow} a^{\dagger}_{\downarrow} c_{\downarrow}) \right], \end{aligned} \tag{3.3}$$

where

$$n^a_{\sigma} = a^{\dagger}_{\sigma} a_{\sigma},\ \ n^c_{\sigma} = c^{\dagger}_{\sigma} c_{\sigma}$$

and σ is a spin index. To avoid double occupancy of the impurity we need to include additional "constrain" term:

$$H = H_{Ab} + U_a (n^a_{\downarrow} + n^a_{\uparrow} - 1)^2. \tag{3.4}$$

Rewritten in Abrikosov's fermionic operators the (3.4) model can be represented as effective two-site AIM (see Fig. 3.3) without on-site Coulomb interaction on the "auxiliary" site 2. The

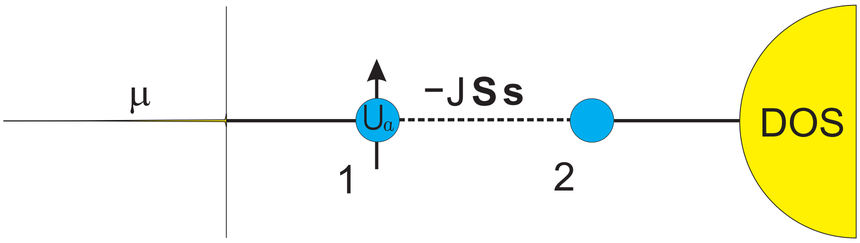

Figure 3.3: The $s-d$ model in fermionic representation (3.4) is equivalent to 2-site AIM without on-site Coulomb repulsion on the auxiliary site 2. The auxiliary site 2 is coupled to the bath of conduction electrons with known DOS (yellow), the "target" site 1 has no hybridization term, its bare Green function reads $\mathcal{G}_1(i\omega) = \frac{1}{i\omega+\mu}$. Site 1 corresponds to a operators in (3.3) and 2 – to c correspondingly.

"impurity" site 1 has no explicit hybridization to the bath of conduction electrons, its bare Green function on Matsubara frequencies reads $\mathcal{G}_1(i\omega) = \frac{1}{i\omega+\mu}$. This site is coupled to the auxiliary site 2 via Heisenberg exchange J. Because of absence of on-site Coulomb repulsion U on the site 2, its local DOS is the same as a DOS of the conduction electrons bath. Formally we have to take $U_a \to \infty$, but the tests (performed by NRG [88], see Fig. 3.4) shows that relatively small value of U_a (of order of $|J|$) is enough to avoid the double occupancy even at high-temperature regime. Hereafter in this Chapter under "high temperatures" we assume $T >> T_K$.

3.3 Kondo impurity in piecewise-constant DOS, benchmarks

We consider the piecewise-constant DOS because it is the simplest case of non-uniformal density of conduction electron states that can be relevant to realistic models. It is well known that the Kondo temperature T_K of the impurity coupled to the conduction electron bath with constant DOS (so called "flat band") scales as

$$T_K \propto De^{-\frac{1}{2J\rho(E_F)}}, \tag{3.5}$$

where $D = W/2$ is half of the width of conduction band, J is a strength of Heisenberg coupling between the impurity and conduction electrons and $\rho(E_F)$ is a bath DOS at Fermi level [20]. Therefore keeping the $J \times \rho(E_F)$ product constant we obtaining the same Kondo temperature as well as the spin susceptibility of the impurity [20]. The interesting question is, what kind of scaling takes place if the Kondo impurity is embedded into bath of conduction electrons with non-constant DOS.

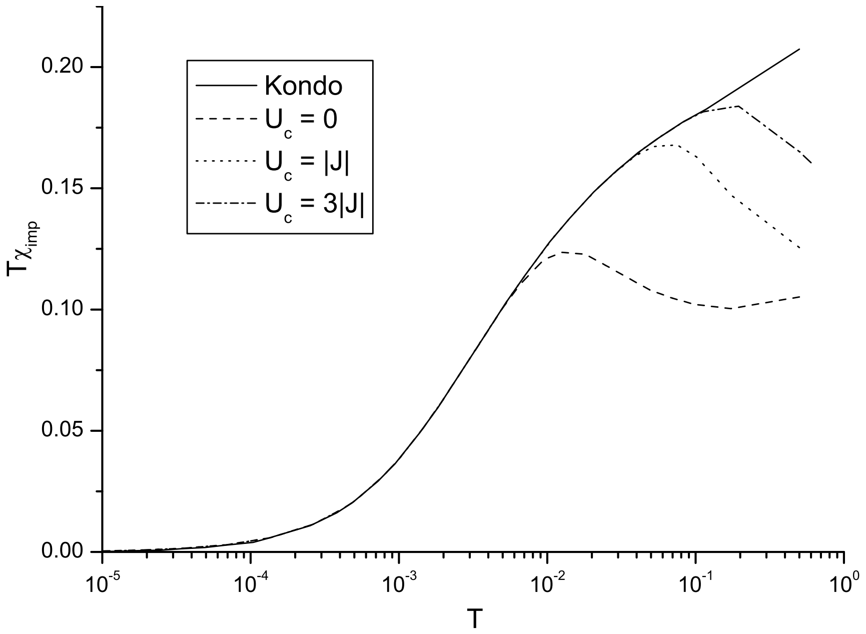

Figure 3.4: Comparing of the impurity magnetic susceptibility (2.76) of the impurity described by $s-d$ Hamiltonian (”Kondo”, solid line) and its fermionic representation (3.4) with different values of the constrain U_a. The impurity is coupled to bath with constant density of states (bandwidth $D = 2$ eV), exchange parameter $J = -0.3$ eV, $T\chi$ in $(g\mu_B)^2$, T in eV [88].

The Numerical Renormalization group (NRG) method is known to be an appropriate tool to solve an impurity problem with uniform bath DOS. Also this method has much less computational effort than QMC in physically interesting case of low temperatures, but it is unclear whether the NRG can be used for treating impurity problems with strongly non-uniform bath DOS.

In this section we check the reliability of the NRG and CT-QMC results in case of Kondo impurity embedded into band with piecewise-constant DOS. The bath DOS of the systems studied in this section are shown on Fig. 3.5, insets. The bandwidth $W = 2$ eV in both cases, the band DOS at the Fermi level are $\rho_{peak}(E_F) = 3/4$ and $\rho_{dip}(E_F) = 1/3$ in case of peak or dip at the Fermi level correspondingly. The width of the peak (and dip) $\Delta = 0.2$ eV is of order of $|J|$.

Intuitively one can presume that at low temperatures the impurity can ”feel” band DOS $\rho(E)$ only in some vicinity of E_F (of order of $|J|$) and at high temperatures the system’s behavior is determined only by some average $\bar{\rho}(E) = 1/W$. To check this assumption we performed two series of auxiliary NRG calculations: the Kondo impurity was coupled to flat-band bath DOS with $D = 1\ eV$. The exchange coupling parameter values were $J = -0.2\ eV$ and $J = -0.3\ eV$. The local susceptibility (2.76) of these systems is presented on Figs. 3.5, 3.6 with blue and red dash lines correspondingly. Fig. 3.5 gives an impression on behavior of the local susceptibility

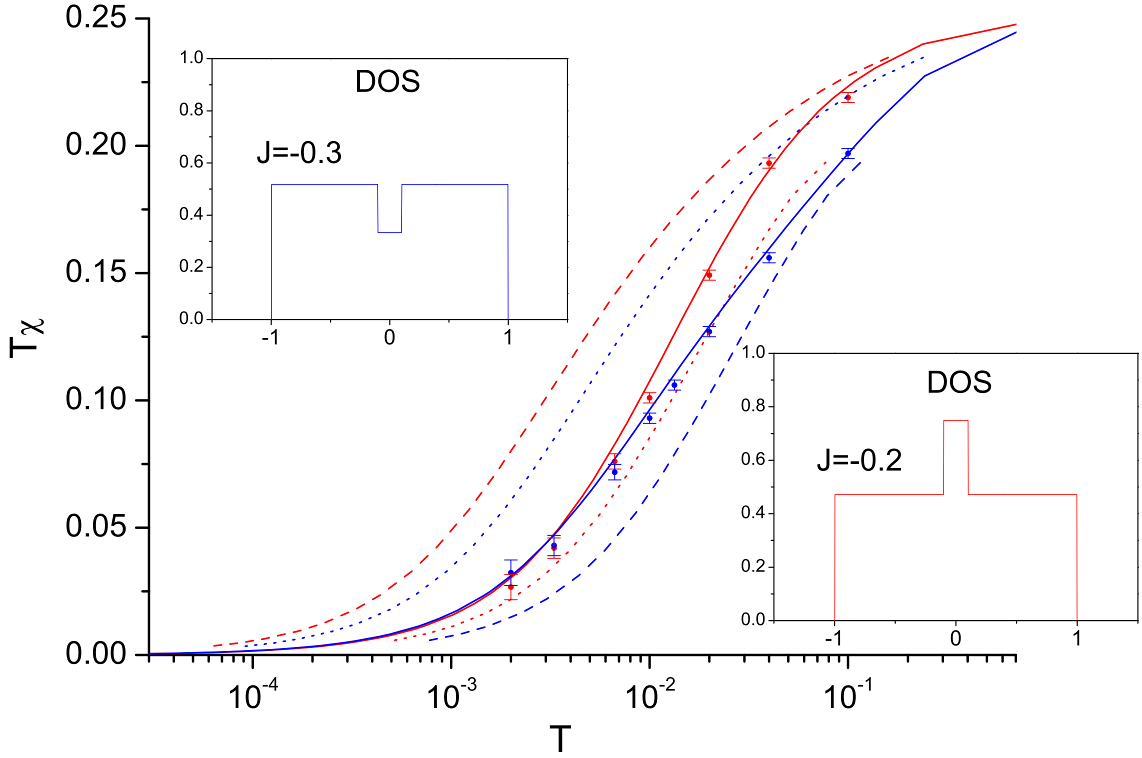

Figure 3.5: Non-universal behavior of $T\chi$ obtained by CT-QMC (dots) and NRG (solid lines) for the Kondo impurity embedded to band with piecewise-constant DOS.

The non-uniform (piecewise-constant) bath DOS are shown on the insets. They have either dip (for $J = -0.3\ eV$) or peak ($J = -0.2\ eV$) of the width of $0.2\ eV$ at the Fermi level. The bath DOS at Fermi level are $\rho_{dip}(E_F) = 1/3\ eV^{-1}$ and $\rho_{peak}(E_F) = 3/4\ eV^{-1}$ correspondingly.

Main graph: statical susceptibility $T\chi$ in $(g\mu_B)^2$, T in eV. Dots and solid lines are results of CT-QMC and NRG calculations correspondingly. Red color hereafter denotes $J = -0.2\ eV$ and blue $J = -0.3\ eV$. The following NRG results for flat-band bath DOS are shown for the reference.

Dash lines: $J = -0.2\ eV, W = 2\ eV$ (red); $J = -0.3\ eV, W = 2\ eV$ (blue).

Red dot line: $J = -0.2\ eV, W = 4/3$ ($\rho(E_F) = 3/4 = \rho_{peak}(E_F)$, as in peak on the right inset);

Blue dot line: $J = -0.3\ eV, W = 3\ eV$ ($\rho(E_F) = 1/3 = \rho_{dip}(E_F)$, as in dip on the left inset).

At the *high temperature* limit $T\chi$ the systems with piecewise-constant bath DOS have the *same* asymptotic as one for the flat-band case with the same bandwidth $D = 1\ eV$.

in all the temperature range, one can also estimate the Kondo temperature, according to Ref. [20] $T\chi(T_K) \approx 0.07$. The next Fig. 3.6 show us the low temperature behavior of susceptibility itself (without the T factor) and allow us to compare the low-temperature asymptotic of different systems.

Next, according to relation (3.5), we performed a linear scaling (see Ref. [20]) of these results to get the susceptibilities for the following reference systems: $J = -0.2\ eV$, $D = 4/3\ eV$, $\rho(E_F) = 3/4 = \rho_{peak}(E_F)$ and $J = -0.3\ eV$, $D = 3/2\ eV$, $\rho(E_F) = 1/3 = \rho_{dip}(E_F)$ that

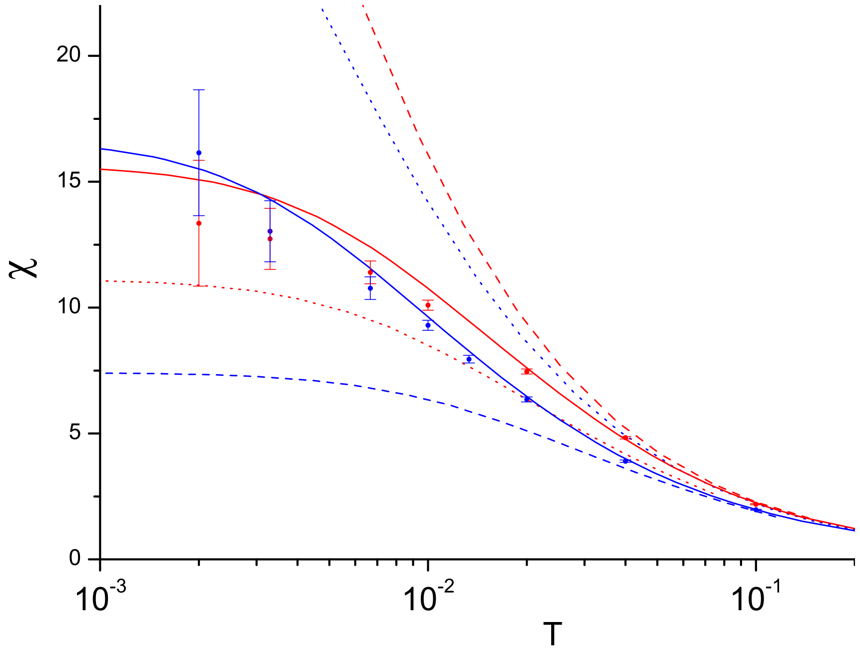

Figure 3.6: Non-universal behavior of χ obtained by CT-QMC (dots) and NRG (solid lines).
The statical susceptibility χ in $(g\mu_B)^2/eV$, T in eV. Dots and solid lines are results of CT-QMC and NRG calculations for Kondo impurity embedded into piecewise-constant bath DOS. The Non-uniform (piecewise-constant) bath DOS is the same as in previous figure, see Fig. 3.5, insets. Red color hereafter denotes $J = -0.2\ eV$ and blue $J = -0.3\ eV$.
The following NRG results for flat-band bath DOS are shown for the reference.
Dash lines: $J = -0.2\ eV$, $W = 2\ eV$ (red); $J = -0.3\ eV$, $W = 2\ eV$ (blue).
Red dot line: $J = -0.2\ eV$, $W = 4/3$ ($\rho(E_F) = 3/4 = \rho_{peak}(E_F)$, as in peak on the right inset);
Blue dot line: $J = -0.3\ eV$, $W = 3\ eV$ ($\rho(E_F) = 1/3 = \rho_{dip}(E_F)$, as in dip on the left inset).
The *low-temperature* behavior is *different* from the flat-band one with the same $\rho(E_F)$ (dot lines). We have a qualitative agreement between NRG ant CT-QMC up to quite low temperatures ($T = 0.002\ eV \approx 20\ K$)

corresponds to flat-band systems with the same bath DOS at the Fermi level as the piecewise-constant DOS under consideration. The susceptibilities of these reference systems are shown on the Figs. 3.5, 3.6 using red and blue dot lines correspondingly.

Finally we performed CT-QMC and NRG calculations of local susceptibility (2.76) for the Kondo impurity embedded to the band of free electrons with piecewise-constant DOS (see Fig. 3.5, insets). The results are shown on Figs. 3.5, 3.6 using dots (CT-QMC) and solid lines (NRG) correspondingly. Red and blue colors corresponds to systems with $J = -0.2$ and $J = -0.3$ accordingly.

The assumption to check was the following: At high temperatures ($T \tilde{>} D$) the impurity ”feels” only some average DOS of conduction electrons bath. One can see exactly this dependence on Fig. 3.5. But at low temperatures the susceptibility demonstrates strongly non-universal behavior, i.e. it cannot be reproduced by simple linear scaling of results for corresponding flat-band bath. On the Fig. 3.6 one can see that at low temperatures asymptotic of susceptibilities of the Kondo impurities coupled to piecewise-constant bath DOS (dots for CT-QMC an solid lines for NRG) do not tends to one for the flat-band problem with the same $\rho(0)$ (dot lines): the results for piecewise-constant DOS have completely different low-temperature asymptotic comparing to any of the reference flat-band systems. It is related to the fact that the bath DOS has a features near the Fermi level and the impurity ”feels” the band DOS features situated closer than $\approx |J|$ from the Fermi level.

The conclusion is following: simple scaling that keeps the product $J\rho(E_F) = constant$ works only for constant bath DOS (flat-band) and it is completely non-applicable for the systems that have bath DOS anomalies at the energies of order of $|J|$ near the Fermi level. This calculation showed good agreement between NRG and CT-QMC in broad range of temperatures, and the CT-QMC method found to be applicable to this kind of systems.

3.4 Kondo impurity in realistic systems

Atomic clusters, small particles, and nanostructures derived from them constitute a vast research area with multiple subfields and a truly interdisciplinary character. One of the most interesting and challenging subjects in cluster physics is the study of many-body phenomena and their dependence on size, composition and local atomic environment. On the one side, one aims to identify the effects that are specific to small particles and that differentiate them from molecules and condensed matter. On the other side, one would like to understand how the physical properties are modified in the finite-size regime, particularly in order to link the behavior of different atoms and macroscopic solids. From the cluster perspective the latter can be regarded as the limits of a much richer and often quite complex dependence of many physical properties as a function of the number of atoms. In general one may distinguish a small-size or microscopic regime, where the changes of the physical properties with size are very strong, a large-size or mesoscopic regime, where statistical and scaling concepts apply, and in between a more or less extended crossover region. Cluster magnetism is a problem of central importance in this context.

During past decades, most of the experimental and theoretical studies in the field have been concerned with transition-metal (TM) clusters which motivate remarkable fundamental and technological interests. One of the main goals of these investigations is to understand how the magnetic behavior evolves as the valence electrons of an isolated atom start to delocalize throughout the cluster and how the itinerant magnetism characteristic of TM-solids is achieved. In this case the hybridization among the d shells and the resulting d-band formation play a dominant role. Consequently, electronic-structure contributions such as size, geometry, and composition dependence leading to band narrowing, local environment, and proximity effects have attracted considerable attention [105].

While cluster magnetism has been intensively studied from this itinerant or band perspective, much less is known about clusters containing magnetic atoms with localized states [106, 107, 108, 109]. Therefore, it is very interesting to investigate TM or rare-earth (RE) impurities in metallic clusters in order to elucidate the magnetic behavior of localized moments in finite metallic systems, as well as the modifications that are induced in confined conduction electrons by a magnetic impurity.

In solids, TM and RE systems are known to present remarkable properties, such as Kondo, intermediate- valence, or heavy-fermion behavior, which are intrinsically related to the localized character of the d or f electrons and to their interactions with the conduction-band states [110, 111]. The unconventional properties of such strongly-correlated systems reflect the competition between the tendency of electrons to delocalize in order to form chemical bonds or energy bands, and the resulting local charge fluctuations, which increase the Coulomb-repulsion energy and favor the occupation of localized states. A typical manifestation of this interplay is the presence of small (Kondo) energy scales in the excitation spectrum that lead to striking low-temperature properties. Clearly, the reduction of size in clusters can drastically modify and

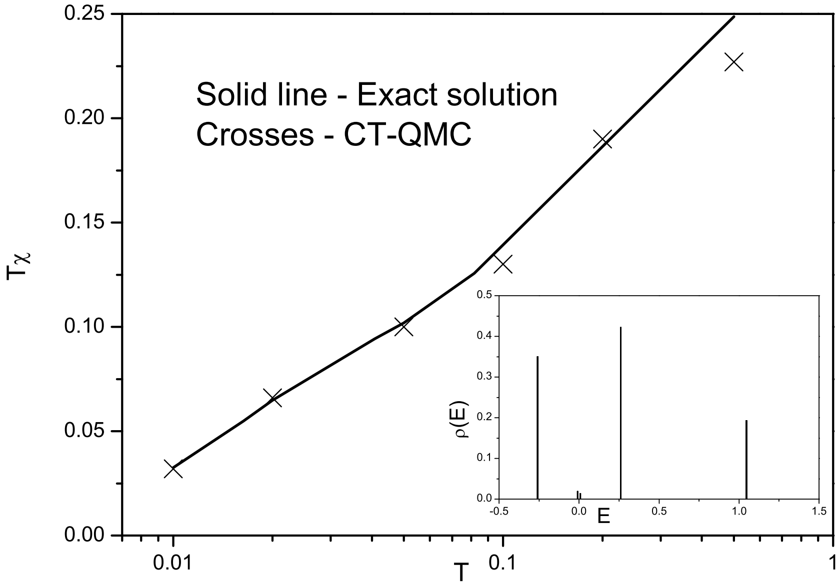

Figure 3.7: Main plot: Comparison of the magnetic susceptibility $T\chi$ obtained by CT-QMC with the exact solution, $T\chi$ in $(g\mu_B)^2$, T and E in eV. Inset: conduction electron states with energies E_k and hybridization strength V_k (see Eq. (3.6)). Exchange interaction strength $J = -0.35\ eV$.

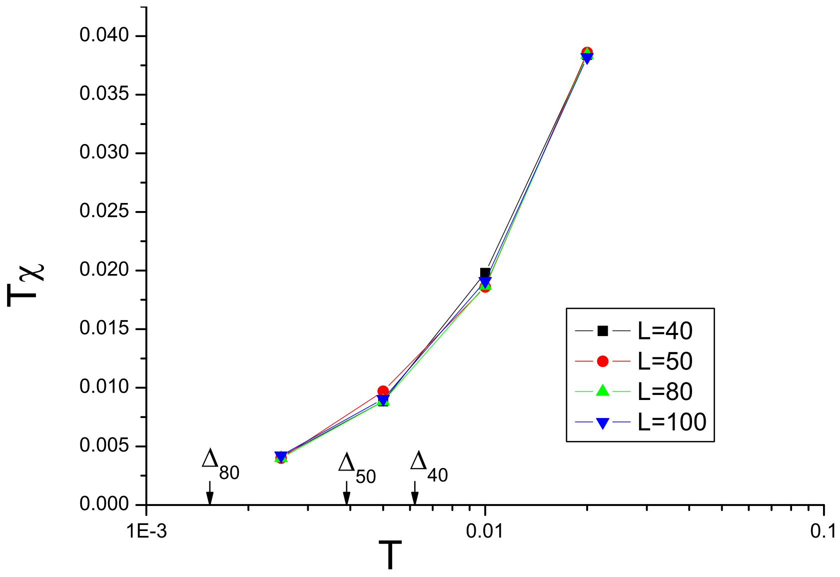

Figure 3.8: Comparison of $T\chi$ on finite 2D lattices of different size (40x40) to (100x100) in low temperature region ($T << T_K$). The exchange coupling strength is $J = -0.3\ eV$, $T\chi$ in $(g\mu_B)^2$, T in eV. The CT-QMC method shows a good precision at temperatures below both Kondo temperature T_K and the mean level spacing Δ.

eventually suppress these phenomena, as a result of the discreteness of the energy spectrum, due to a reduction of the number of electronic states near the Fermi level, or even as a consequence of a change in the lattice structure.

In the case of a magnetic impurity in a finite-size metallic environment, the formation of a Kondo singlet [112, 20, 113] may be significantly affected if the number of conduction-electron states is so small, that the mean level spacing is larger than the temperatures $k_B T$. The consequence of that is not complete screening of the impurity magnetic moment.

To check applicability of our method to this class of systems we performed a benchmark on exactly diagonalizable system: the conduction electrons have only 5 states. The ED program was written by A. Zhuravlev [88]. The bath Green function on Matsubara frequencies for CT-QMC calculation was obtained by discrete Hilbert transform

$$\mathcal{G}(i\omega_n) = \sum_{k=1}^{N} \frac{V_k^2}{i\omega_n - E_k}, \tag{3.6}$$

where V_k is a hybridization strength between the impurity and k-th level of bath and E_k is a position of that level. This benchmark (Fig. 3.7) shows that CT-QMC method is suitable for systems with discrete spectra such as small clusters, grains, etc. The CT-QMC shows a good precision even at the temperatures much lower than mean level spacing $\Delta \approx 0.3\ eV$.

Another interesting case is Kondo impurity on infinite two-dimensional lattice. Since of van Hove singularity at the Fermi level (and as a consequence infinite DOS at E_F) one cannot estimate Kondo temperature using $T_K \propto e^{-\frac{1}{2J\rho(E_F)}}$ formula from Ref. [20].

Since our aim is to study realistic models, including impurities coupled to systems with discrete spectrum of non-interacting electrons, we have to pay attention to the effects caused by finite level spacing. In order to do it we performed a number of benchmark calculations for Kondo impurity embedded into finite two-dimensional lattice. The exchange coupling strength is $J = -0.3\ eV$. First we checked how the size of lattice (and a mean level spacing) affect the results. On Fig. 3.8 we plot magnetic susceptibility for a low-temperature region ($T << T_K$). The results for different lattice sizes (from 40x40 to 100x100) are almost coinciding even at the temperatures below the mean level spacing of the corresponding lattice states. Than we performed a benchmark calculation of magnetic susceptibility for Kondo impurity coupled to finite (200x200) two-dimensional lattice. It can be considered as a reference system for Kondo impurity placed on infinite two-dimensional lattice, since the finite-size effects does not play a role in the temperature range we study, see Fig. 3.8. The results were compared to the NRG

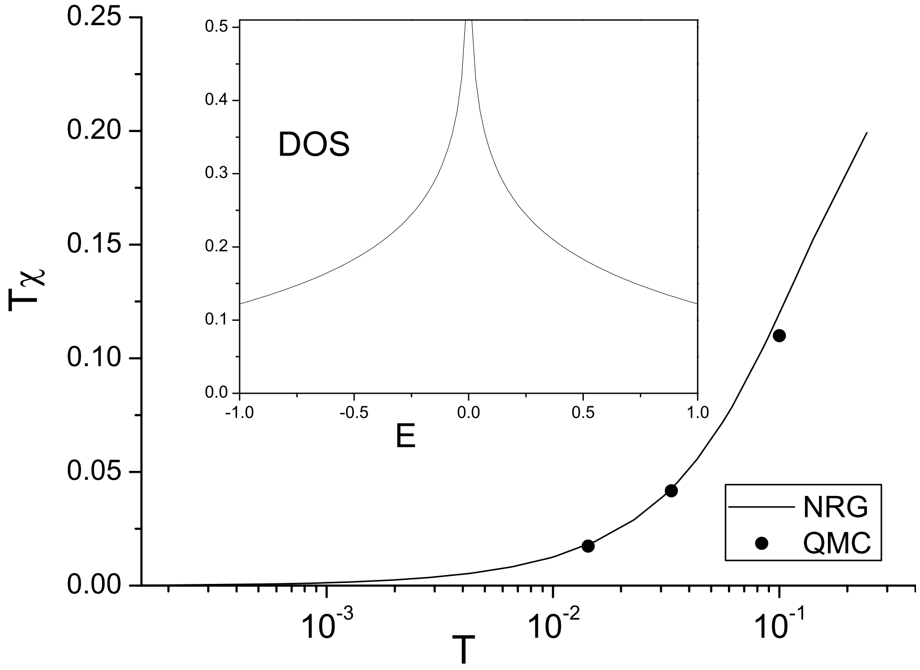

Figure 3.9: Main plot: Comparison of CT-QMC results (dots) with NRG [88] (solid line) on finite 2D lattice (200x200). Exchange coupling strength is $J = -0.3$ eV, $T\chi$ in $(g\mu_B)^2$, T in eV. The inset gives the local density of states on the arbitrary lattice site for infinite 2D lattice. The non-interacting DOS have van Hove logarithmic singularity on the Fermi energy. In this case Kondo temperature $T_K \approx 0.05$ eV is much lager than in case of flat-band DOS ($T_{K_{FB}} \approx 0.01$ eV see Fig. 3.5).

data [88], see Fig. 3.9. These two methods show very good agreement. Comparing Figs. 3.5 and 3.9 one can conclude that in case of infinite two-dimensional lattice the Kondo temperature $T_K \approx 0.05$ eV is much lager than in case of flat-band DOS of bandwidth $W = 2$ eV ($T_{K_{FB}} \approx 0.01$ eV, see Fig. 3.5).

Another attractive testing ground for the new numerical method is Kondo impurity on disordered 2D lattice [114]. This model is relevant to disordered metals and Kondo alloys. On Fig. 3.10 we plot the local impurity spin susceptibility, multiplied by temperature T for some given realization of the disorder, obtained in tight-binding model [114]. Here dots denotes the results obtained with the continuous time quantum Monte Carlo (CT-QMC) method and solid lines – results of the modified version of NRG [114, 88]. For temperatures close to the Kondo temperature both methods agree well.

In this chapter we described the Kondo impurity embedded into conduction electrons bath with arbitrary DOS. We show that the CT-QMC method can be applied to a variety of interesting systems. It can treat Kondo impurity problems with arbitrary density of conduction electron states taking into account all its features. This is related to the exact character of Hilbert transform that is used to convert bath DOS to non-interacting Green function $\mathcal{G}$. The local magnetic susceptibility χ of such systems have been studied. We found non-universal behavior of the local magnetic susceptibility even in such a simple systems as Kondo impurity embedded into conduction electrons bath with piecewise-constant DOS. We showed applicability of the new computational method to such an interesting systems as Kondo impurity embedded to disordered 2D lattice, ultra small grain and infinite 2D lattice with van-Hove singularity in the bath DOS.

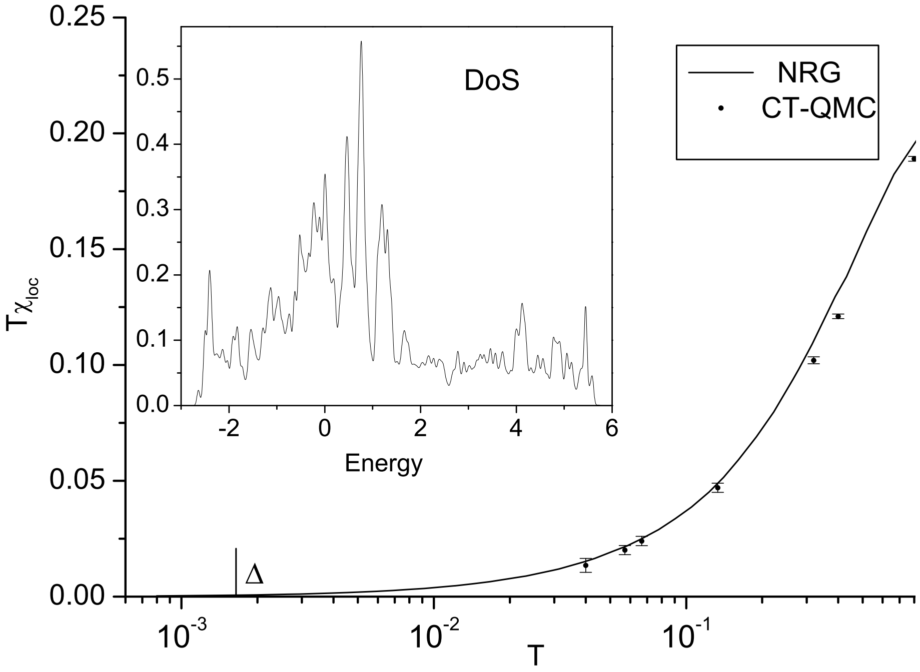

Figure 3.10: The impurity susceptibility as function of temperature calculated with the NRG method for $J/D = 0.35$, $W/t = 2$, $L = 70$, $T\chi$ in $(g\mu_B)^2$, T in eV [88]. The calculation is done at the site where T_K is maximal. Our results based on the CT-QMC simulation (discrete points) is included. The inset shows the local density of states, where $E = 0$ denotes the Fermi energy. The mark indicates the mean level spacing Δ [114].

4 Multiorbital impurity problem for general Coulomb interaction

In this Chapter we shall discuss application of the CT-QMC impurity solver to multiorbital Anderson model for the most general case. The tests with known solutions obtained by exact diagonalization method are performed. Two-, three- and five-orbital impurity models are discussed. Realistic model of cobalt impurity embedded into copper matrix is studied. A brief analysis of effects emerging due to the spin-flip processes have been made.

4.1 2- and 3-orbital Anderson impurity model

The Anderson impurity model (AIM) play a key role in several recent developments in the theory of strongly correlated electron systems. For example, the Dynamical Mean-Field Theory (DMFT) maps spatially extended system representing correlated solid to Anderson impurity model with a self-consistently determined bath of conduction electrons [3] (see Chapter 5). Therefore AIM is also essential to our understanding of local moment formation in metals, and to that of heavy-fermion materials, particularly in the mixed valence regime [20]. It is therefore important to have at our disposal quantitative tools allowing calculation of physical quantities associated with the AIM. The quantity of interest depends on the specific context. Many recent applications require a calculation of the local Green function (or spectral function), and of some two-particle correlation functions (e.g. magnetic susceptibilities, see Chapters 2, sec. 2.3.5 and Chapter 3).

Multiorbital Anderson impurity model is one of the great challenges in many-body theoretical physics. Whereas single-orbital AIM can be solved with reasonable precision different ways (NRG, Hirsh-Fye QMC, etc.), two-orbital model is much more complicated to solve. The two-orbital AIM with arbitrary hybridization to the bath of free electrons can be solved using

NRG (with some problems concerning to logarithmic discretization of the bath DOS and growing Hilbert space), multi-orbital Hirsh-Fye QMC (without spin-flip terms in the interaction, else the sign problem emerges and hamper the calculations at lower temperatures). Three-orbital AIM is extremely hard problem for NRG and in Hirsh-Fye QMC including of spin-flip terms leads to very strong limitation for temperature and Hund exchange parameter (see Chapter 2, sec. 2.2.3). Five-orbital model with arbitrary DOS of the band electrons can be solved by Hirsh-Fye QMC only with Coulomb interaction of density-density type.

From the point of view of application to real physical systems, two- and three-orbital AIM are interesting because 5-fold degenerated atomic d orbitals in cubic crystal field splits to double degenerated e_g and the triple degenerated t_{2g}. Then, if the splitting between these levels (t_{2g} and e_g) is large enough, one of them becomes empty (or fully occupied) and in order to find low energy excitation spectra we have to solve the problem involving only two (e_g) or three (t_{2g}) orbitals (for review see Ref. [115]). One of such interesting systems, namely strontium ruthenate Sr_2RuO_4 is considered in Chapter 5.

For two- and three-orbital AIM discussed in this chapter we used general rotationally invariant Hamiltonian [116]. Its local part reads:

$$
\begin{aligned}
H_{imp}^{loc} = -\sum_{\substack{\sigma \\ i\neq j}} t_{ij} c_{i\sigma}^{\dagger} c_{j\sigma} + \frac{U}{2} \sum_{i,\sigma} n_{i\sigma} n_{i\bar{\sigma}} + U' \sum_{\substack{\sigma \\ i\neq j}} n_{i\sigma}^{\dagger} n_{j\bar{\sigma}} \\
+ (U'-J) \sum_{\substack{\sigma \\ i\neq j}} n_{i\sigma} n_{j\sigma} + J \sum_{\substack{\sigma \\ i\neq j}} \left(c_{i\sigma}^{\dagger} c_{j\bar{\sigma}}^{\dagger} c_{i\bar{\sigma}} c_{j\sigma} + c_{i\sigma}^{\dagger} c_{i\bar{\sigma}}^{\dagger} c_{j\sigma} c_{j\bar{\sigma}} \right),
\end{aligned}
\tag{4.1}
$$

where $U' = U - 2J$ and $i,\ j$ are the orbital indices. The first term represents interorbital hoppings, second – diagonal Coulomb repulsion in case of double occupancy of $i-th$ orbital, third and forth are interorbital repulsion and the last one includes spin-flip and pair-hopping terms. All the models discussed in this section have full spin and orbital degeneracy. All the densities of states are normalized by one, i.e. represents partial DOS of one particular orbital.

The main goal of the CT-QMC method is a possibility to treat multiorbital impurities with Coulomb interaction of arbitrary form, coupled to band of non-interacting electrons with arbitrary DOS. Thus our primary intention was to reveal the effects arising in multiorbital systems due to spin-flip and pair-hopping processes. First, to benchmark our method we performed a

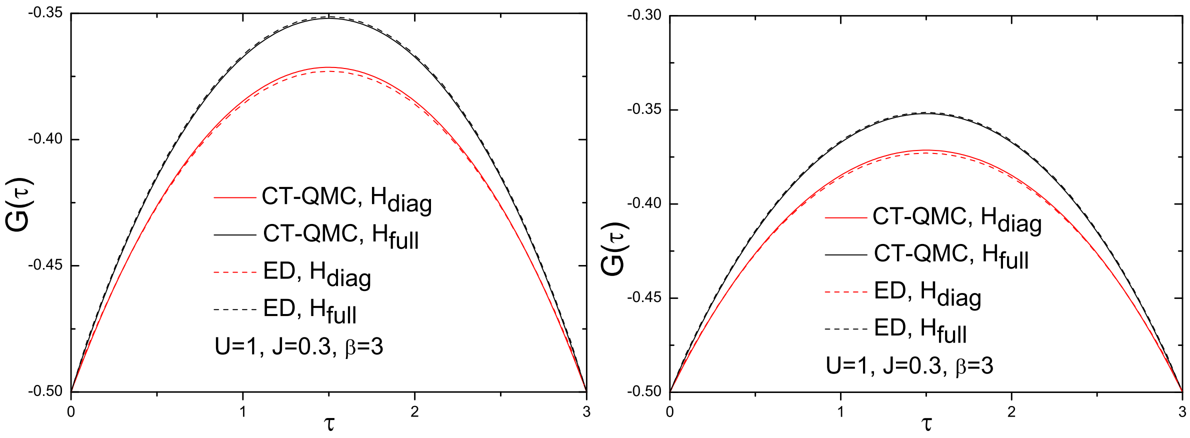

Figure 4.1: Imaginary time interacting Green functions of the two-orbital (left panel) and three-orbital (right panel) AIM in atomic limit at half-filling, τ in eV^{-1}. Interaction parameters are the same for the both models: $U = 1\ eV$, $J = 0.3\ eV$, $\beta = 3\ eV^{-1}$. Solid lines denotes CT-QMC results, dash – exact diagonalization (ED). Black color corresponds to full Coulomb interaction, red – to density-density one.

number of tests in atomic limit (when impurity has no hybridization to the band of conduction electrons). In this limit AIM can be solved exactly using Exact diagonalization (ED) method [28, 5]. The resulting imaginary time Green functions are shown on Fig. 4.1. The Green functions on imaginary time axis show almost perfect coincidence between CT-QMC and ED results for both (full and density-density) interaction parts of Hamiltonian.

To get an impression what are the qualitative changes of the impurity DOS caused by including of non-diagonal Coulomb interaction terms, we show the impurity DOS corresponding to $G(\tau)$ from Fig. 4.1, left panel on the Fig. 4.2, left panel. Note that here we have relatively large temperature of order of 0.3 eV that leads to significant broadening. Another test also performed by ED demonstrates the behavior of three-orbital AIM away from half-filling: the occupancy corresponds to 2 electrons in t_{2g} orbitals (see Fig. 4.2, right panel). In comparison to two-band half-filled model it is more sensitive to the form of interaction Hamiltonian.

Next we performed a series of CT-QMC calculations for three-orbial AIM (see Fig. 4.3). The system under consideration was the following: three-orbital impurity with occupancy $n = 4$ electrons in t_{2g} orbitals. The impurity is either coupled to band of free electrons with semielliptical DOS (SC) or has no coupling to bath (i.e. AIM in atomic limit, also so-called thermal bath, TB). The parameters of the Coulomb interaction were the same as in the previous test, namely $U = 1\ eV$, $J = 0.3\ eV$, but the inverse temperature was increased to $\beta = 10\ eV^{-1}$ ($T \approx 1200K$). Comparing imaginary time interacting Green functions of AIM in atomic limit (see Fig. 4.3 left

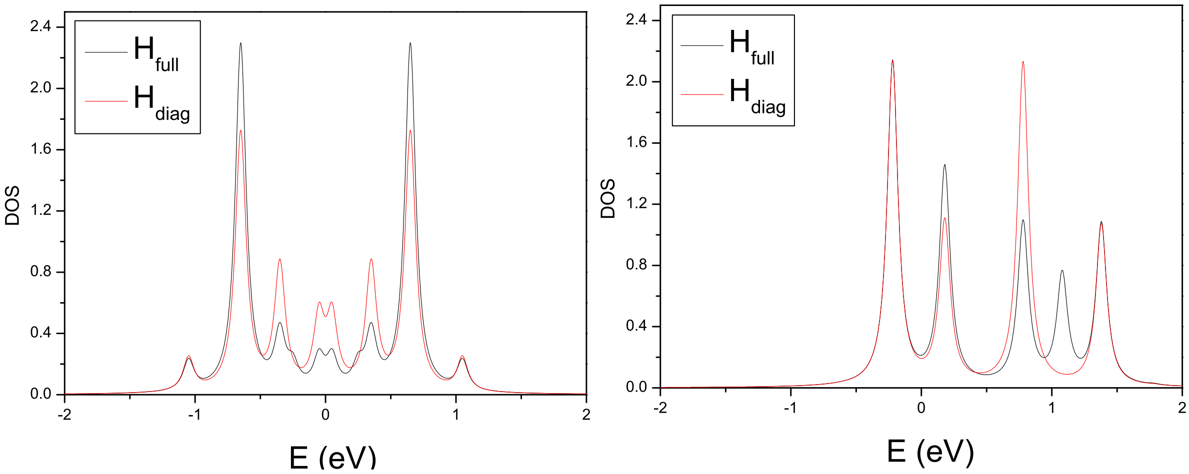

Figure 4.2: ED results for DOS of the AIM in atomic limit. Left panel: two-orbital AIM at half-filling, this DOS corresponds to $G(\tau)$ from Fig. 4.1, left panel. Right panel: three-orbital AIM with occupancy $n = 2$ per all 3 orbitals. Interaction parameters are the same for the both models: $U = 1\ eV$, $J = 0.3\ eV$, $\beta = 3\ eV^{-1}$. Black lines corresponds to full Coulomb interaction, red – density-density one.

panel, red and black solid lines corresponds to CT-QMC results for diagonal and full Coulomb interaction; red and black dash lines demonstrates ED results for the same models) we can find that CT-QMC and ED results are in good agreement. The spectral functions of the systems mentioned above are shown on Fig. 4.3, right panel. The difference between full and density-density Coulomb interaction for the case of atomic limit (see Fig. 4.3, right panel, black and red dash lines) is much smaller than at higher temperature (see Fig. 4.2, right panel). This effect of decaying the spin-flip effects with lowering the temperature *in atomic limit* can also be observed in two- and five-orbital cases.

Another question we would like to discuss is: how coupling of the impurity to the bath of conduction electrons change the effects caused by non-diagonal interaction terms. The resulting imaginary time Green functions for AIM coupled to the narrow bath with semielliptical DOS of the width $W = 2D = 0.2\ eV$ are shown on the Fig. 4.3, left panel with brown (full Coulomb interaction) and orange (density-density one) lines. These systems exhibit almost the same behavior as AIM in atomic limit: brown line (full vertex) almost coincides with the atomic limit solution (black lines) and the orange one (diagonal vertex) also has the same trend as the exact solution for atomic limit (red dash line). Coupling of this system to the broad ($W = 2D = 1\ eV$) band with semielliptical DOS (i.e. without any fine structure near the Fermi level) leads to almost complete decaying of the spin-flip effects (see Fig. 4.3, blue lines denotes full Coulomb interac-

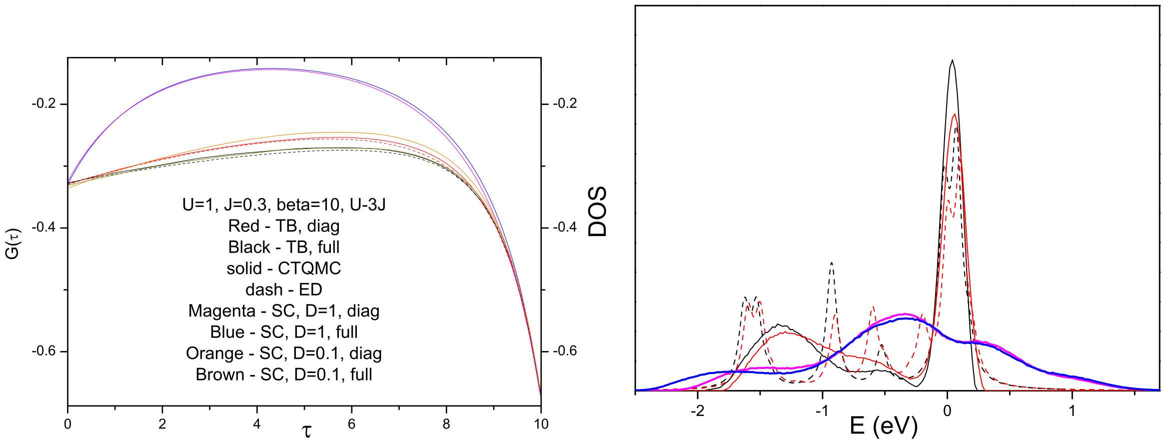

Figure 4.3: Imaginary time interacting Green functions (left panel, τ in eV^{-1}) and local densities of states (right panel) of 3-orbital AIM away from half-filling. Dash lines denotes ED results, solid – CT-QMC. Red lines corresponds to AIM in atomic limit with density-density Coulomb interaction, black – atomic limit and full interaction vertex. Orange and brown lines (shown only on the left panel) – $G(\tau)$ for AIM coupled to narrow ($W = 0.2\ eV$) bands and diagonal and full interaction correspondingly. Magenta and blue lines denotes results for impurity hybridized with broad ($W = 2\ eV$) bands and diagonal and full interaction respectively.

tion, magenta – diagonal one). The only small changes in $G(\tau)$ around $\tau \approx 0.8\ eV^{-1}$ corresponds to difference in high energy behavior of the DOS around $-2\ eV$.

In order to check whether the spin-flip effects are sensitive to bath DOS features near the Fermi level, we performed a number of CT-QMC calculations for three-orbital AIM. The interaction parameters were following: $U = 3.1\ eV$, $J = 0.7\ eV$ and the inverse temperature was $\beta = 10\ eV^{-1}$ ($T \approx 1200K$). The band DOS was of very specific form: It was $2\ eV$ wide and 20% (or 50%) of bath states were concentrated in the peak positioned in the middle of initial rectangular DOS. Occupancy was constrained to be $n = 4$ electrons per all 3 orbitals, that led to shifting the whole bath DOS and the mentioned above peak moved slightly below (or at) the Fermi level, see Figs. 4.4, 4.5, green lines. We were varying the peak width Γ between $0.1\ eV$ and $0.2\ eV$ and the weight of this peak W_P was either 20% (see Figs. 4.4, 4.5, left panels) or 50% (see Figs. 4.4, 4.5, right panels).

One of the advantages of the CT-QMC method we use is a possibility to include spin-flip terms. It is reasonable that spin-flip terms could play important role if there are some anomaly of bath DOS near the Fermi level on scales of order of exchange J. To check this assumption

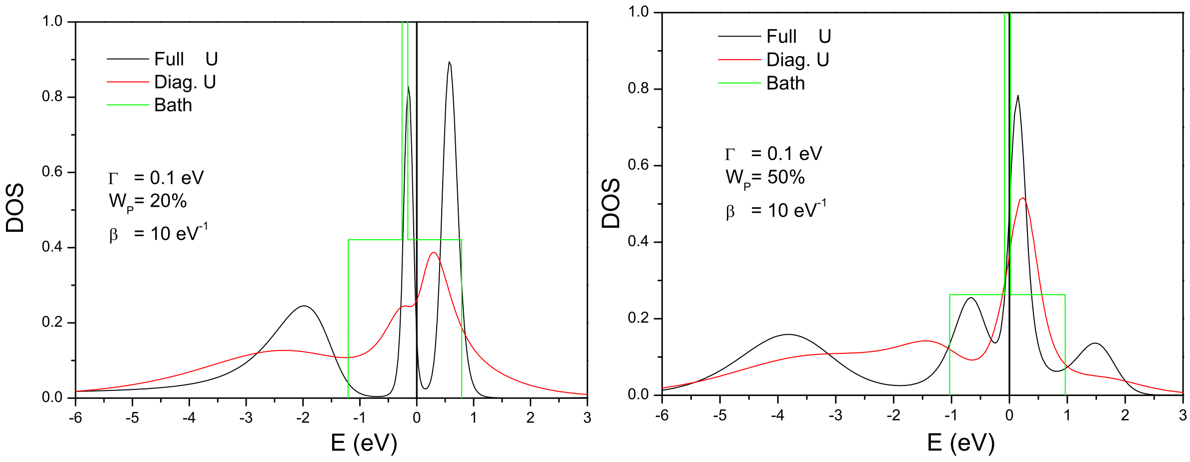

Figure 4.4: DOS of AIM hybridized to the bath with a sharp feature near (or at) the Fermi level. Left panel: the peak of bath DOS is of width $\Gamma = 0.1\ eV$ and contains $W_P = 20\%$ of bath states and lie below the Fermi level. Right panel: the peak of bath DOS is of width $\Gamma = 0.1\ eV$ and contains $W_P = 50\%$ of bath states and crosses the Fermi level. Green line denotes bath DOS, black and red – resulting impurity DOS obtained using full and diagonal interaction vertex correspondingly. Interaction parameters: $U = 3.1\ eV$, $J = 0.7\ eV$. Inverse temperature: $\beta = 10\ eV^{-1}$ ($T \approx 1200K$).

we performed a number of test calculations using described above piecewise-constant bath DOS with a peak below (see Figs. 4.4, 4.5, left panels), or at the Fermi level (see Figs. 4.4, 4.5, right panels).

The results are following: if the peak weight make up 20% (and it is completely under the Fermi level, see Figs. 4.4, 4.5, left panels) we have essential difference between impurity density of states obtained using diagonal (red lines) and full (black lines) Coulomb interaction: in case of full vertex (black) the impurity has pronounced tendency to rise the peak of the density of states exactly at position of the original bath DOS peak, whereas diagonal interaction (red) hardly exhibit this feature.

In the situation, when the peak weight make up 50%, the constrain on the occupancy lead to shifting the whole bath DOS, and its peak becomes located at the Fermi level, see Figs. 4.4, 4.5, right panels. In this case we also observe prominent difference between impurity densities of states obtained using full and density-density Coulomb interaction respectively. In contrast to the previous case, the structure of impurity DOS near the Fermi level is almost the same, only the Hubbard bands differs significantly.

Note that in both cases the effects caused by spin-flips are much more pronounced than in

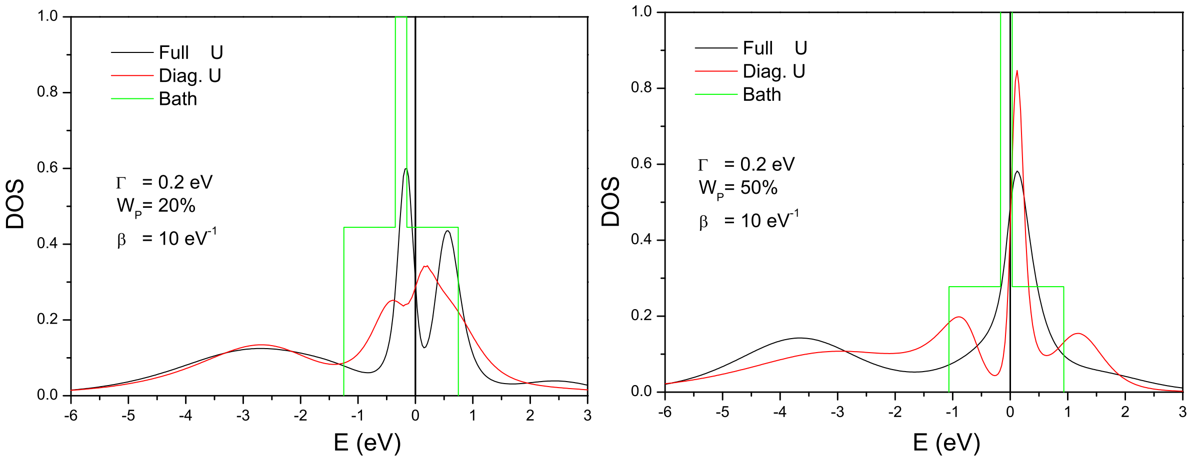

Figure 4.5: DOS of AIM hybridized to the bath with a sharp feature near (or at) the Fermi level. Left panel: the peak of bath DOS is of width $\Gamma = 0.2\ eV$ and contains $W_P = 20\%$ of bath states and lie below the Fermi level. Right panel: the peak of bath DOS is of width $\Gamma = 0.2\ eV$ and contains $W_P = 50\%$ of bath states and crosses the Fermi level. Green line denotes bath DOS, black and red – resulting impurity DOS obtained using full and diagonal interaction vertex correspondingly. Interaction parameters: $U = 3.1\ eV$, $J = 0.7\ eV$. Inverse temperature: $\beta = 10\ eV^{-1}$ ($T \approx 1200K$).

the case of smooth bath DOS. (see e.g. Fig. 4.3 right panel, blue and magenta lines: the impurity DOS exhibit almost no dependence on form of the interaction).

4.2 5-orbital Anderson impurity model

The five-orbital model is relevant to $3d$ and $4d$ transition metals, that displays a variety of interesting magnetic properties. Scanning tunneling microscopy (STM) has become one of the most basic tools for the manipulation of matter at the atomic scale. Although this experimental technique making a big progress, the detailed theoretical understanding of experimental data is still incomplete. One of the most famous examples of atomic manipulation is associated with the surface Kondo effect observed when transition metal ions (like Co) are placed on a metallic surface (such as $Cu\ (111)$) [95]. The surface Kondo effect is the basis for the observation of surprising phenomena such as quantum mirages [98], and has attracted a lot of attention and interest in the last few years. The current understanding of these observations is based on the assumption that only surface states of $Cu\ (111)$ are involved in the scattering of electron waves by the Co adatoms [117, 118, 119]. Nevertheless, recent experiments with Co atoms on the Cu (100) surface (that does not have any surface state) [97], or in Cu (111) but close to atomic surface steps (that affect the surface states) [120] have indicated that bulk states are behind the surface Kondo effect. Although the last decade experiments made considerable progress, all the model calculations done were either used effective one-orbital impurity model [121] or included only diagonal part of Coulomb interaction [71, 122, 22], even with realistic hybridization functions obtained in LDA.

Therefore in order to have a possibility to treat these physically interesting multiorbital systems accurately, the further development of existing impurity solvers is needed.

We start from multi-orbital Hubbard Hamiltonian, for a general case it can be written in the following form:

$$H = -\sum_{\langle ij\rangle\sigma} t c^{\dagger}_{i\sigma} c_{j\sigma} + \frac{1}{2} \sum_{\substack{\langle ijkl\rangle \\ \sigma\sigma'}} U_{ijkl} c^{\dagger}_{i\sigma} c^{\dagger}_{j\sigma'} c_{k\sigma'} c_{l\sigma}, \tag{4.2}$$

where i, j, k, l are orbital indices, σ, σ' – spin indices, t_{ij} is hopping amplitude between orbitals i and j and U_{ijkl} is coulomb interaction matrix element.

Here we use Slater parametrization of U matrix. It is based on the multipole expansion of Coulomb potential:

$$\frac{1}{|\mathbf{r}-\mathbf{r}'|} = \sum_{kq} \frac{4\pi}{2k+1} \cdot \frac{r^k_<}{r^{k+1}_>} Y^*_{kq}(\widehat{r}) Y_{kq}(\widehat{r}'). \tag{4.3}$$

Then matrix elements of Coulomb interaction in basis of spherical harmonics (Y_{lm}) can be represented in the following form:

$$< mm'|U|m''m''' >= \sum_k a_k(m, m'', m', m''') F^k, \tag{4.4}$$

where the angular part

$$a_k(m, m', m''', m''') = \sum_{q=-k}^{k} (2l+1)^2 (-1)^{m+q+m'} \begin{pmatrix} l & k & l \\ 0 & 0 & 0 \end{pmatrix}^2 \begin{pmatrix} l & k & l \\ -m & -q & m' \end{pmatrix} \begin{pmatrix} l & k & l \\ -m'' & q & m''' \end{pmatrix} \tag{4.5}$$

is represented by 3j-symbols and

$$F^k = e^2 \int_0^{\infty} r^2 dr |\varphi_d(r)|^2 \int_0^{\infty} (r')^2 dr' |\varphi_d(r')|^2 \frac{r^k_<}{r^{k+1}_>} \tag{4.6}$$

are Slater integrals. Here φ_d is atomic d orbital, $r_<^k$ ($r_>^k$) is the smallest (largest) value of r and r', k corresponds to all even numbers $k \leq 2l$.

Since we have to deal only with outer electronic shell, we will take into account screened part of Coulomb interaction. In order to do that we determine Coulomb matrix elements according to Eq. (4.4) using renormalized F^k parameters instead of Eq. (4.6). The Coulomb U and exchange J constants can be expressed as

$$U = \frac{1}{(2l+1)^2} \sum_{mm'} U_{mm'} = F^0, \tag{4.7}$$

$$J = \frac{1}{(2l+1)^2} \sum_{mm'} J_{mm'} = \sum_{k \neq 0} \begin{pmatrix} l & k & l \\ 0 & 0 & 0 \end{pmatrix}^2 F^k. \tag{4.8}$$

In case of d electrons Eq (4.8) reads $J = (F^2 + F^4)/14$ and the atomic-like ratio $F^2/F^4 = 0.625$ [15]. For d electrons only non-zero Slater parameters are F^0, F^2 and F^4. Using the above formulas we can extract effective Slater integrals F^k via U and J parameters, that can be calculated using constrained LDA technique (see e.g. Ref. [123, 15]). Note that the value of intra-atomic (Hund) exchange interaction J is not sensitive to the screening and approximately equals to $0.7 - 0.9$ eV in different estimations [15].

Since U_{ijkl} matrix elements are spin independent, to generate all terms for the interaction, one should look over all possible combinations of orbital and spin indices. Some combinations can violate Pauli principle and shouldn't be taken into account (for details of this procedure see Chapter 2, sec. 2.3.3).

For the particular problem, namely Co impurity in the copper matrix, the basis set of spherical harmonics Y_{lm} is used. In this basis the interaction part of the hamiltonian contains only terms of the following form:

$$H_{int}^{diag} = U_{iijj} n_{i\sigma} n_{j\sigma'}, \tag{4.9}$$

where $n_{i\sigma} = c_{i\sigma}^\dagger c_{i\sigma}$ and

$$H_{int}^{nd} = U_{ijkl} c_{i\sigma}^\dagger c_{j\sigma'} c_{k\sigma'}^\dagger c_{l\sigma}, \tag{4.10}$$

where $i \neq j$ and $k \neq l$. Note that in this basis we have no terms of the $U_{iikl} n_{i\sigma} c_{k\sigma'}^\dagger c_{l\sigma}$ ($i \neq j$ and $k \neq l$) form, that hampers the calculation leading to sign problem.

The (4.9) terms are so-called diagonal ones, and the Coulomb matrix for the d electron shell in the basis of complex harmonics contains 45 non-equivalent terms of this kind. The terms of the (4.10) form can be further classified to a spin-flips, where $i = l,\ j = k$ and the less symmetric general fur-indices vertex, where this condition is not fulfilled. Notice, that pair-hopping terms $(i = k,\ j = l)$ in basis of spherical harmonics are restricted by symmetry. Finally for d electron system in addition to 45 diagonal terms we have 20 non-equivalent spin-flips and 64 terms of the most general form. To get an understanding of the role of non-diagonal terms of interaction we performed some tests. Since the exact solution for AIM in the atomic limit can be found using exact diagonalization (ED) method, we compared CT-QMC results with ED. On Fig. 4.6, left panel we compared Green function on imaginary time obtained using full interaction part of the Hamiltonian and reduced one (with only density-density terms). The model parameters are following: $U = 1\ eV,\ J = 0.4\ eV;\ \beta = 2\ eV^{-1}$. Since $G(0) = G(\beta) = -0.5$ the system is at half-filling (according to Eq. (2.20) at $\tau = 0,\ \tau' = 0^+$). First, there is a very good agreement between ED and CT-QMC results, especially in case of density-density type interaction. Also it is worth mentioning that the $G(\tau)$ function is symmetric with respect to $\tau = \beta/2$, that means the particle-hole symmetry of the system is perfectly described by the CT-QMC method. In the case of full interaction (including terms of the form 4.10) the agreement is still good but not perfect anymore. It can be attributed to significant increasing of the number of ”fields”: from 45 terms of the form (4.9) in diagonal case to 129 with full d orbital atomic Coulomb interaction. Therefore much more MC steps are needed to reach convergence of the Green function. Also the deviation of the CT-QMC result from the exact solution is non-uniform on the $[0,\beta]$ range: in vicinity of $\tau = 0$ and $\tau = \beta$ (short time correlations) the coincidence is very good, and the biggest deviation can be observed near the $\tau = \beta/2$ point. The reason of such behavior is that short time correlations are caused mostly by the ”fields” with the biggest magnitude, i.e. density-density ones. Whereas the long time correlations (and, as a consequence, behavior of $G(\tau)$ function near $\tau = \beta/2$ and the spectral function near the Fermi level) are more affected by the terms of interaction of order of J. Since the most of these small terms are of the non-diagonal form in the interaction vertex (e.g. the interaction part of Hamiltonian in case of f electrons consists of 91 density-density term and 286 non-diagonal ones), the largest error in $G(\tau)$ can be found in the $\tau \approx \beta/2$ region.

Next we performed a test of 5-orbital AIM in atomic limit away from half-filling with the interaction parameters $U = 2\ eV,\ J = 0.7\ eV,\ \beta = 3.7\ eV^{-1}$. The results are shown on Fig. 4.6, right panel. Since the system is fully degenerated over all orbital and spin degrees of freedom, the overall occupancy of the impurity is equal to $5\ orbitals \times 2\ spins \times (1-G(0^+))$ (see Eq. (2.20) at $\tau = 0$, $\tau' = 0^+$) and in this case makes up 8 electrons.

The difference between Green function of the interacting system with full Coulomb interaction and density-density one is visible on the $G(\tau)$. The agreement between CT-QMC and ED results is worse than in the half-filled case, because the system away from half-filling is related to larger average perturbation order in Monte-Carlo sampling.

Lowering the temperature to $T \approx 1200\,K$ ($\beta = 10\ eV^{-1}$) in the *atomic limit* leads to decaying of the Green function features caused by non-diagonal part of Coulomb interaction (see Fig. 4.7). The results for diagonal and full Coulomb interaction are completely coinciding in half-filled case. An interesting point is, that agreement between CT-QMC and ED becomes better even at temperatures lower than in the previous case (see Fig. 4.6). Note that this ”freezing” of non-diagonal terms of the interaction happens *only in atomic limit for the half-filled case*, since the non-degenerate ground state for d^5 configuration.

As it was already mentioned in sec. 2.3.2, increasing of Coulomb interaction strength as well as decreasing temperature leads to increase of the average perturbation order of our expansion, Eq. (2.25). Typical distribution of the perturbation order for 5-orbital AIM is shown on Fig. 4.8, main plot. The model parameters are following: $n = 7$ electrons, $U = 4\ eV$, $J = 0.7\ eV$, $\beta = 10\ eV^{-1}$. Dash line denotes the perturbation order during accepted steps that involved non-diagonal fields. The coincidence of distributions maxima of both histograms demonstrate that the acceptance rate mostly depends on diagonal interactions.

On the inset of the Fig. 4.8 we show distribution of the non-diagonal terms, i.e. contribution of the Coulomb fields of the form (4.10) to the resulting Green function. The zero entry of this histogram counts the number of steps when all the fields contributing to the fermionic determinant (2.35) were of density-density type (4.9). The entry with index 2 show us the number of steps where the average (2.35) was containing two spin-flip type fields (4.10).

4.3 Realistic system: cobalt atom embedded in copper matrix

The magnetic properties of nanostructures play essential role in the design of miniaturized spin-based devices. One of the key parameters is the magnetic interaction between the constituent atoms of a nanostructure. This interaction can be due to direct or indirect coupling as well as mediated via a supporting substrate or host. Depending on the strength and sign of the ex-

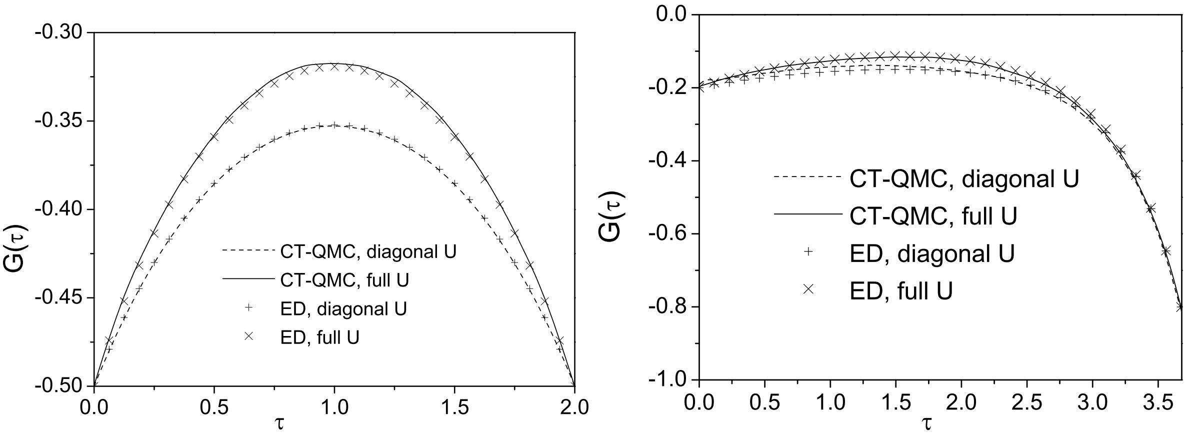

Figure 4.6: Interacting Green function on imaginary time for 5-orbital AIM at the atomic limit, τ in eV^{-1}. Solid and dash lines denotes CT-QMC results for full and density-density Coulomb interaction correspondingly, ”x” and ”+” symbols – ED results for the same systems respectively. Left panel:$U = 1\ eV,\ J = 0.4\ eV;\ \beta = 2\ eV^{-1}$, 5-orbital impurity at half-filling Right panel: $U = 2\ eV,\ J = 0.7\ eV$, $\beta = 3.7\ eV^{-1}$, 5-orbital impurity with 8 electrons.

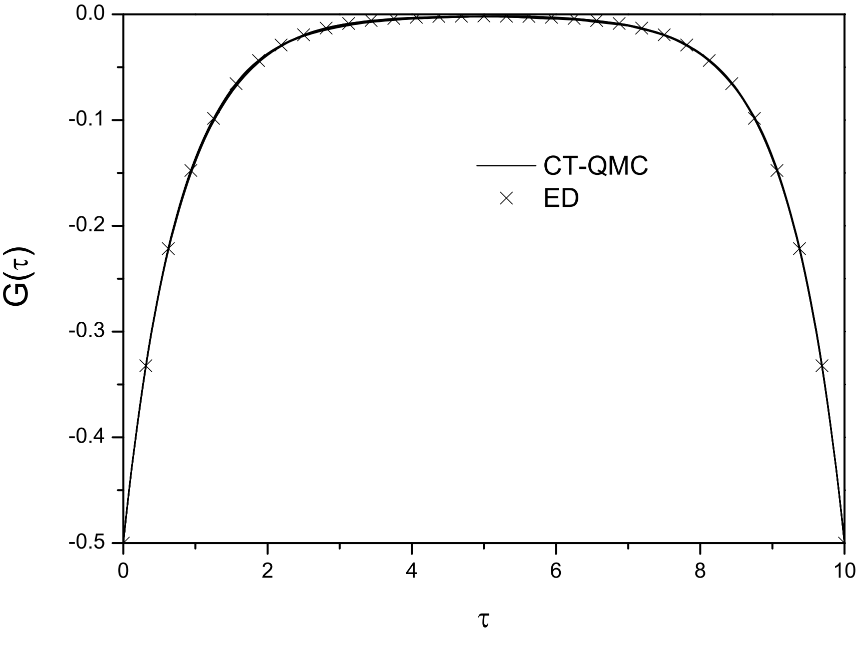

Figure 4.7: Interacting Green function on imaginary time for 5-orbital AIM at the atomic limit. Model parameters: $U = 1\ eV$, $J = 0.4\ eV$; $\beta = 10\ eV^{-1}$, τ in eV^{-1}. Solid line denotes $G(\tau)$ obtained by CT-QMC, ”x” symbols – ED one. Results for full and density-density Coulomb interaction completely coincides.

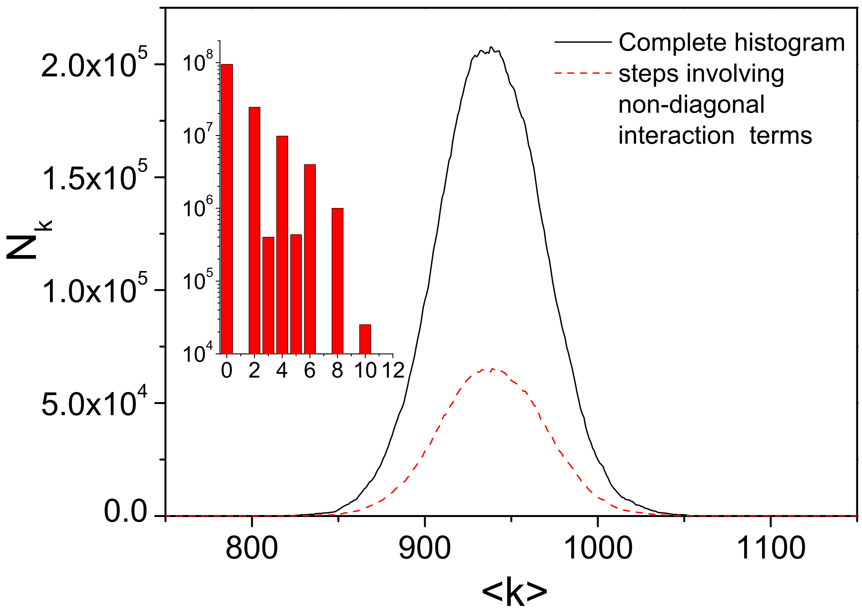

Figure 4.8: Main graph: Histograms of Ω_k distribution, $U = 4\ eV$, $J = 0.7\ eV$, $\beta = 10\ eV^{-1}$, 5-orbital impurity coupled to realistic bath with 7 electrons (*Co* in *Cu*). Solid line denotes full histogram, dash histogram of steps involving non-diagonal fields.
Inset: histogram of non-diagonal interaction fields, $\langle U \rangle = 4\ eV$, $\langle J \rangle = 0.7\ eV$, $\beta = 1\ eV^{-1}$, 5-orbital impurity coupled to bath with semi-elliptical DOS ($W = 0.5\ eV$) at half-filling.

change interaction, the nanostructure can be driven into ferromagnetic or antiferromagnetic state or complex spin structures [124]. The recent STM spin-flip experiments by Hirjibehedin and co-workers [125] have enabled a direct probing of the magnetic interaction in linear manganese chains decoupled from the metallic substrate by insulating spacer layer. Another experiments to determine the exchange interaction between individual cobalt adatoms on a metallic substrate as a function of their distance were done by Chen et al. [126] and Wahl et al. [127]. A Cobalt nanostructures, namely chains and clusters on metallic surface also are of a great experimental and theoretical interest [128, 129]. One of the most important characteristics of such systems is Kondo temperature. The Kondo temperatures of different 3*d* transition metals impurities in non-magnetic bulk are shown on Fig. 4.9 [130]. The deviation of the impurity's 3*d* shell filling from the half-filled case (that takes place in manganese) leads to surviving of the Kondo scattering processes at relatively high temperatures.

Since the Kondo temperature is extremely sensitive to density of states at Fermi energy, position of the impurity (on the surface at FCC or HCP site, embedded into surface layer of

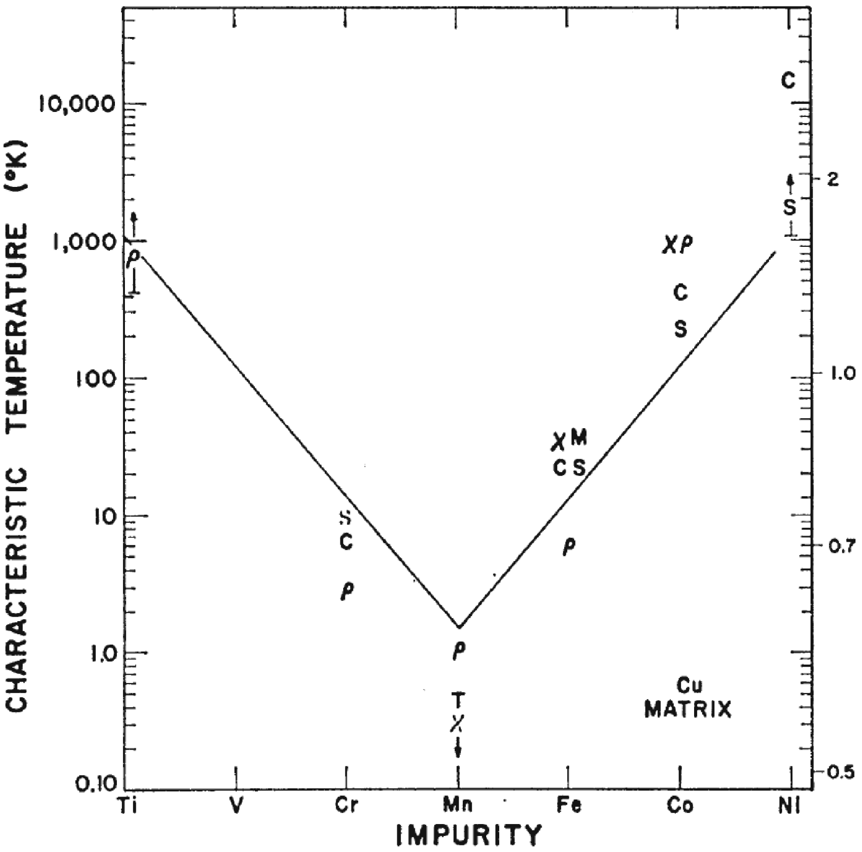

Figure 4.9: Experimental results for Kondo temperatures of different 3*d* transition metals in bulk copper matrix. Symbols used to represent each type of measurement are: susceptibility χ, resistivity ρ, specific heat *C*, thermoelectric power *S* and Mössbauer *M*. From Ref. [130].

the substrate or deeper) is also of the critical importance for the many-body effects (see Fig. 4.10). The cobalt impurity embedded into copper matrix exhibit Kondo physics even above room temperature, therefore we shall use it as a benchmark system for our CT-QMC method.

The *Co*-*Cu* system is treated as five-orbital AIM representing 3*d* electronic shell of the cobalt atom hybridized with a bath of conducting *Cu* electrons with known DOS. The bath Green function was obtained using full-potential linearized muffin-tin orbitals method, namely LmtART code developed by S. Savrasov [131]. The LDA calculation is carried out using Cu_3Au crystal structure with lattice constant corresponding to the pure copper. The further tests with a bigger supercell were done, but no qualitative difference to the Cu_3Co system mentioned above was found.

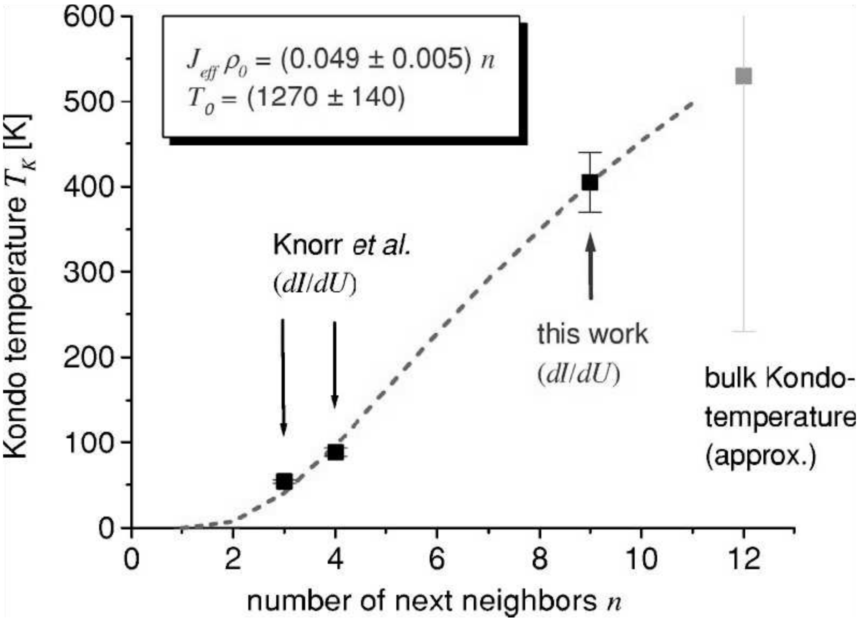

Figure 4.10: Experimental results for Kondo temperatures of *Co* impurities on (or in) *Cu* matrix as a function of coordination number. Four points represents *Co* atom *on Cu* (111) and *Cu* (100) surfaces, *Co* atom *embedded into first layer* of *Cu* (111) surface and *bulk* environment of the Cobalt impurity respectively. From Ref. [132].

The interaction part of impurity Hamiltonian was taken according the procedure described in sec. 4.2. Average parameters of Coulomb interaction $U = 4\ eV$, $J = 0.7\ eV$ were taken from constrained LDA calculations [15]. The complex harmonics Y_{lm} basis is chosen to keep off the terms of $U_{iikl} n_{i\sigma} c^{\dagger}_{k\sigma'} c_{l\sigma'}$ form in interaction part of Hamiltonian. It was done to avoid numerical instability of the algorithm related to the sign problem. In the complex harmonics basis the Green function matrix for $3d$ orbitals splitted by cubic crystal field into t_{2g} and e_g have the following symmetry:

$$G^{loc}_{mm'} = \begin{array}{cc} & \begin{array}{ccccc} -2 & -1 & 0 & 1 & 2 \end{array} \\ \begin{array}{c} -2 \\ -1 \\ 0 \\ 1 \\ 2 \end{array} & \left(\begin{array}{ccccc} \frac{e_g+t_{2g}}{2} & 0 & 0 & 0 & \frac{e_g-t_{2g}}{2} \\ 0 & t_{2g} & 0 & 0 & 0 \\ 0 & 0 & e_g & 0 & 0 \\ 0 & 0 & 0 & t_{2g} & 0 \\ \frac{e_g-t_{2g}}{2} & 0 & 0 & 0 & \frac{e_g+t_{2g}}{2} \end{array} \right) \end{array} \tag{4.11}$$

and becomes non-diagonal.

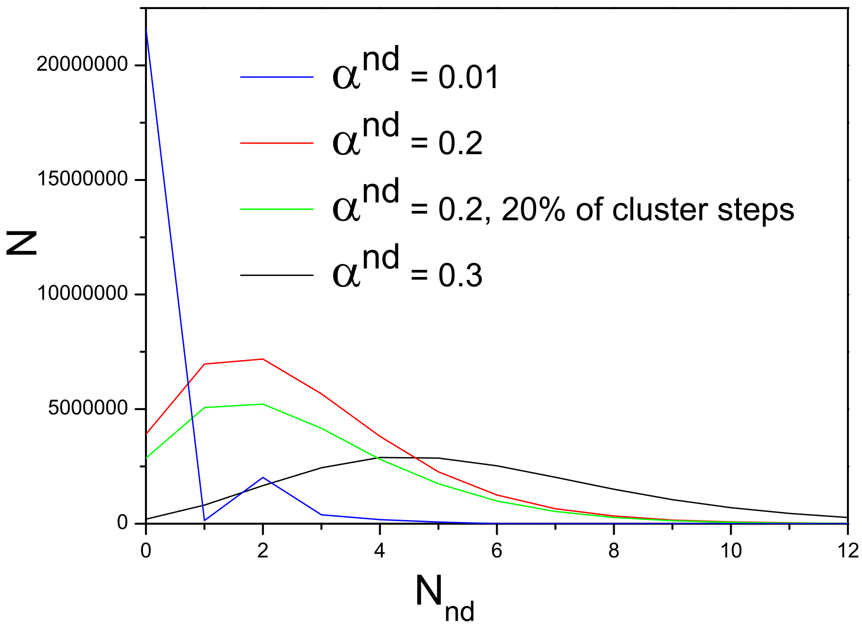

Figure 4.11: Histograms of different distributions of non-diagonal terms for different values of α^{nd}. Model parameters: $U = 2\ eV$, $J = 0.7\ eV$, $\beta = 3.7\ eV^{-1}$, 5 orbitals, realistic bath DOS.

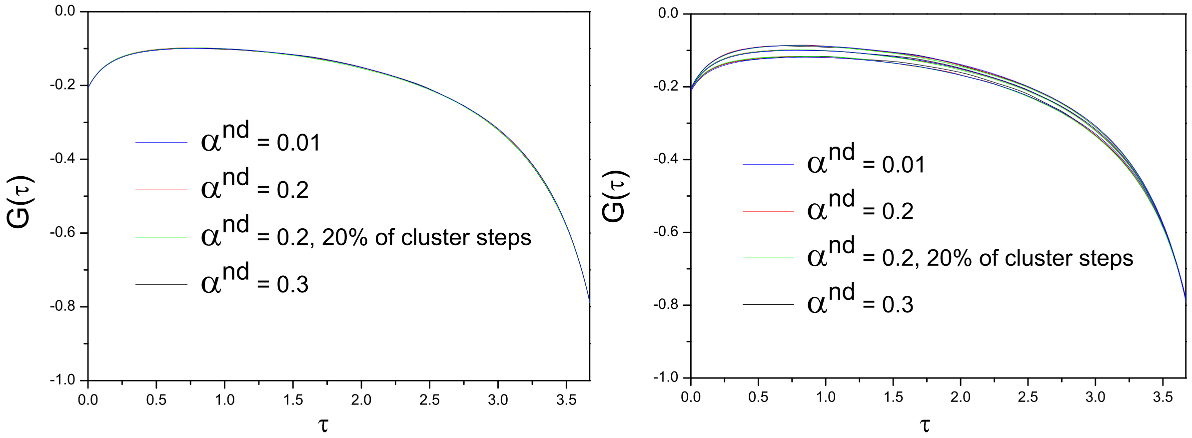

Figure 4.12: Resulting Green functions in imaginary time for different distributions of non-diagonal terms, τ in eV^{-1}. Left panel: Green function averaged over all d orbitals $G_{ii}(\tau)$. Right panel: diagonal elements $G_{mm}(\tau)$ for different d orbitals. The symmetry of $G_{mm}(\tau)$ corresponds to Eq. 4.11. $G_{mm}(\tau)$ Model parameters: $U = 2\ eV$, $J = 0.7\ eV$, $\beta = 3.7\ eV^{-1}$, 5 orbitals, realistic bath DOS.

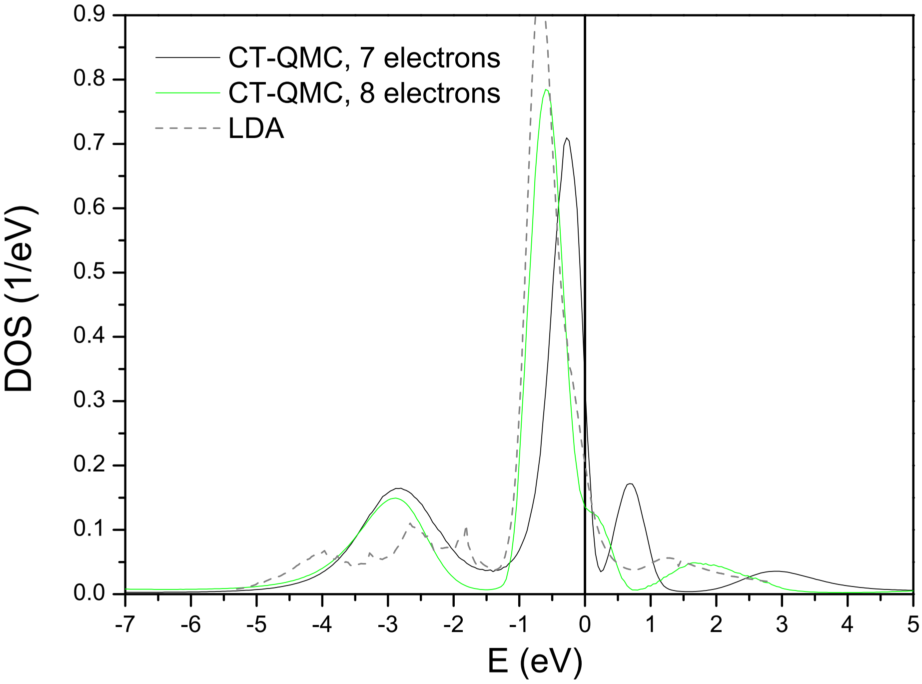

Figure 4.13: *Co* atom embedded in *Cu* matrix. Partial DOS of *Co* 3*d* orbitals with full Coulomb interaction. Comparison of d^7 (black solid line) and d^8 (green solid line) configuration of *Co* 3*d* orbitals. The LDA result (gray dash line) is given for reference. Model parameters: $U = 2\ eV$, $J = 0.7\ eV$, $\beta = 10\ eV^{-1}$.

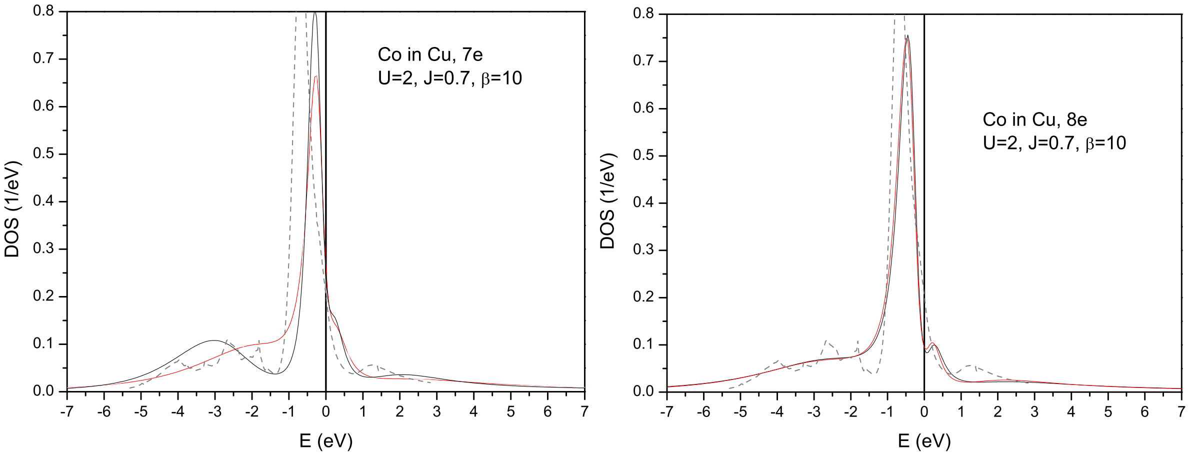

Figure 4.14: *Co* atom embedded in *Cu* matrix. Partial DOS of *Co* 3*d* orbitals (normalized by 1). Comparison of diagonal (red lines) and full (black lines) Coulomb interaction for *Co* impurity in *Cu* matrix. Left panel shows results for d^7 configuration, right – d^8 correspondingly. The LDA result (gray dash line) is given for reference.

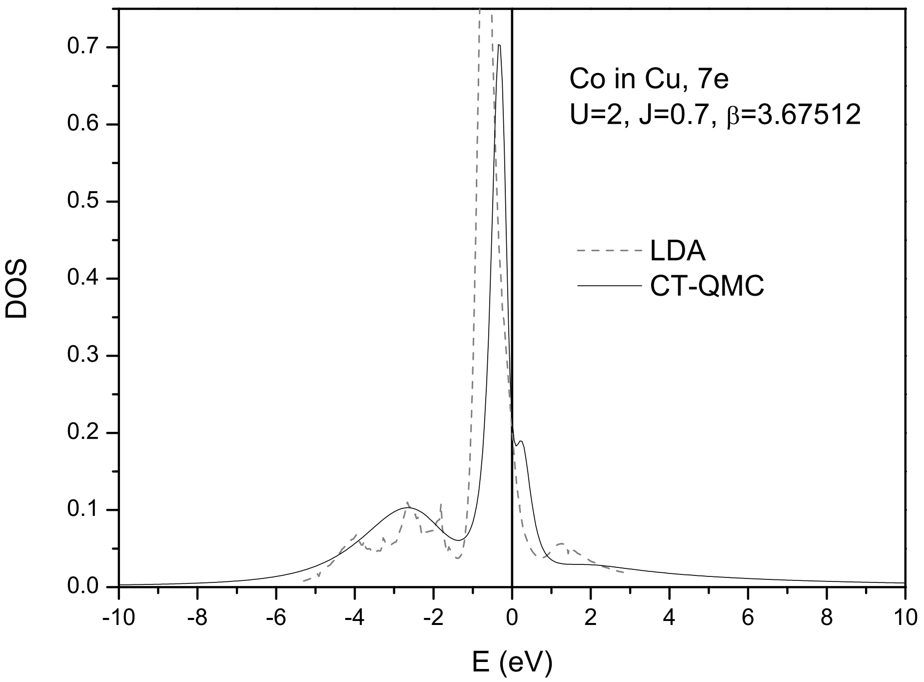

Figure 4.15: *Co* atom embedded in *Cu* matrix. Partial DOS of *Co* 3*d* orbitals (normalized by 1). Test with full Coulomb interaction and increased temperature. The LDA result (gray dash line) is given for reference. Model parameters: $U = 2\ eV$, $J = 0.7\ eV$, $\beta = 3.7\ eV^{-1}$

Another technical issue is a freedom of choosing the α parameters (2.59) and (2.59). Since introducing of these variables results in change of the form of interaction Hamiltonian, it can lead to changes in the QMC random walk process. In order to check that QMC random walk is performed the proper way and non-diagonal terms of interaction (4.10) are taken into account correctly, we performed a test calculation for five-orbital AIM with realistic DOS of conducting electrons band and the following parameters: $U = 2\ eV$, $J = 0.7\ eV$, $\beta = 3.7\ eV^{-1}$. The auxiliary parameter α^{nd} was varying from 0.01 to 0.3. The interaction part of Hamiltonian containing 65 non-equivalent terms (45 density-density terms and 20 spin-flips, the terms of most general form were omitted) was used in order to reduce computational time. The distribution of non-diagonal terms at different values of α^{nd} parameters is shown on Fig. 4.11. To improve the quality of exploring the system's phase space and to avoid trapping in some local energy minima, we use so-called cluster steps, i.e. we propose a pack of Coulomb fields (MC steps) and calculate the acceptance probability taking into account only initial and final state of the system. The ratio of cluster steps proposed by default was 5% and in one calculation (green lines) it was increased

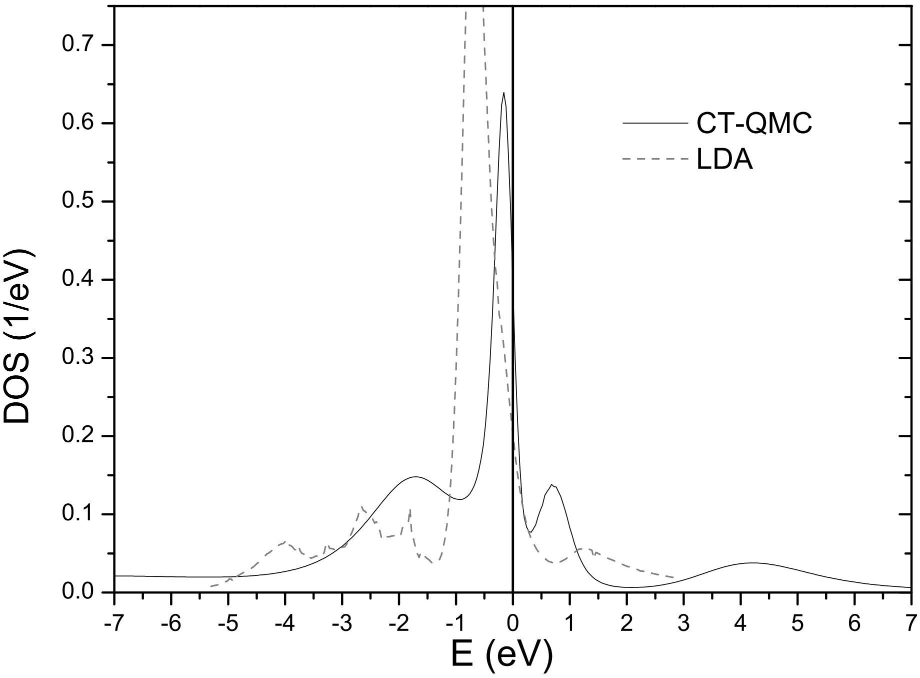

Figure 4.16: *Co* atom embedded in *Cu* matrix. Partial DOS of *Co* $3d$ orbitals (normalized by 1). Test with U increased to 3. The LDA result (gray dash line) is given for reference. Model parameters: $U = 3\ eV$, $J = 0.7\ eV$, $\beta = 10\ eV^{-1}$.

to 20% to find a balance between smaller number of cluster MC steps, but lager number of total MC steps to reach convergence in Green function, The resulting local Green functions (averaged over all the orbitals) are shown on the Fig. 4.12, left panel. The same colors as on Fig. 4.11 were used, but all the curves are virtually undistinguishable. Orbitally resolved local Green functions for these cases are shown on Fig. 4.12, right panel. One can clearly see the splitting of the $3d$ orbitals to t_{2g}, e_g and $\frac{e_g+t_{2g}}{2}$ elements according to cubic crystal field symmetry in the basis of spherical harmonics (4.11). The agreement between the results obtained using different α^{nd} parameters is very good. But the average sign is sensitive to increasing of α^{nd}: it is equal to 0.998 for $\alpha^{nd} = 0.01$ and 0.59 for $\alpha^{nd} = 0.3$ correspondingly. Even with such bad average sign as 0.59 one can obtain spectral properties of the model with high accuracy. However it leads to increase of number of MC steps required to get a given precision of result.

The particular electronic configuration of cobalt atom in copper matrix is unknown. LDA give us 7.3 electrons in $3d$ shell. Since LDA gives not very accurate results (and the fact that correlated impurity tends to have integer occupation) we performed two series of calculations,

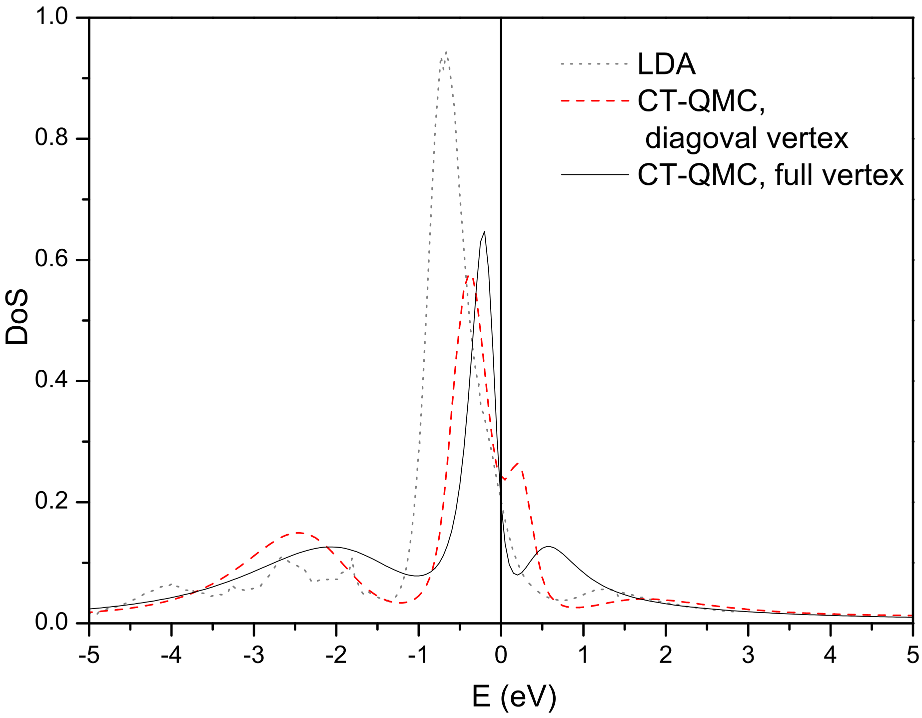

Figure 4.17: *Co* atom embedded in *Cu* matrix. Partial DOS of *Co* 3*d* orbitals (normalized by 1). Comparison between full (black solid line) and density-density (red dash line) Coulomb interaction. The LDA result (gray dash line) is given for reference. Model parameters: $U = 4\ eV$, $J = 0.7\ eV$, $\beta = 10\ eV^{-1}$, 5-orbital impurity with 7 electrons.

namely for d^7 and d^8 configurations.

First we perform a series of calculations for *Co* atom embedded to *Cu* matrix. In order to distinguish the effects caused by electronic configuration we obtained local densities of states for Co *d*-shell within d^7 and d^8 configurations and with full Coulomb interaction. To speed up the calculations U was decreased to 2 eV. On Fig. 4.13 we compare total DOS of Co d-shell in different configurations. While d^8 qualitatively is similar to the LDA result, in case of 7 electrons the quasi-particle peak moves towards to the Fermi level.

Another reason to devote our attention to the d^7 configuration is more pronounced difference between results obtained using full and density-density Coulomb interaction (see Fig. 4.14). The reason of such a difference between d^7 and d^8 configuration is following: in cubic crystal field atomic d orbitals splits to three-fold degenerated t_{2g} and twice degenerated e_g levels. In particular case of *Co* atom in *Cu* matrix the t_{2g} orbitals moves downwards and becomes completely occupied. Therefore the difference between d^7 and d^8 configuration is in occupancy of e_g orbitals: 1 or 2 electrons per two levels respectively. Since d^8 state leads to half-filling of e_g orbitals, we get more symmetrical situation (than within a quarter-filling e_g configuration in d^7) and less pronounced multiplet transitions. The width and position of the quasi-particle peak does not change significantly increasing U to 3 eV or decreasing β to 3.7 eV^{-1} (see Fig. 4.16, 4.14).

The final results obtained for realistic parameters $U = 4\ eV$, $J = 0.7\ eV$, $\beta = 10\ eV^{-1}$ in d^7 configuration are shown on Fig. 4.17. Here the difference between DOS calculated with full interaction part of Hamiltonian and density-density one is well pronounced.

The summary of this chapter is following: we described the benchmark calculations for the model systems with 2 and 3 orbitals using multiorbital CT-QMC impurity solver. We found that the full Coulomb vertex lead to formation of narrow Kondo-like peak near the Fermi level. We also applied our CT-QMC solver to a realistic model of Kondo impurity, namely cobalt atom in copper matrix and studied the effects caused by the spin-flip processes. We found, that d^7 configuration of the *Co* atom leads to strong renormalization of LDA density of states near the Fermi level.

5 Lattice problem

Materials with correlated electrons exhibit variety of interesting phenomena. DFT methods (see sec. 2.1) explains the physical properties of numerous materials, such as simple metals and some semiconductors and insulators. But materials with open d and f electron shells, where electrons occupy narrow orbitals, have properties that are harder to explain without accurate taking into account many-body part of the problem.

Since there is no exact way to solve the lattice problem in presence of strong electron correlations, we need to use some approximations. A recent theoretical framework, namely Dynamical Mean-Field Theory (DMFT) [1, 18] allows to calculate the electronic structure of these correlated materials in the best local scheme. The DMFT is an approximation that maps correlated lattice problem onto single impurity problem. In this case the CT-QMC impurity solver considered above can be used also for investigation of correlated solids.

5.1 Lattice problem. Approximations.

The discovery of the heavy fermion compounds and of the high-temperature superconductors has revived interest in strongly correlated electron systems. These are systems in which the strength of the electron-electron interactions is comparable to or larger than the kinetic energy. Initially the motivation to study such systems came from experiments on transition metal oxides, from the Mott metal-insulator transition, and from the problem of itinerant ferromagnetism. Theoretical progress in the field has been impeded however by the extreme difficulty of dealing with even the simplest model Hamiltonians appropriate for these systems, such as the Hubbard model and the Kondo lattice model. Only in the one-dimensional case we have a variety of theoretical tools to study these models in a systematic manner. For two- and three-dimensional models, one is often unable to assess confidently whether a given physical phenomenon is indeed captured by the idealized Hamiltonian under consideration or whether a theoretical prediction reflects a true feature of this Hamiltonian, rather than an artifact of the approximation.

These difficulties originate in the nonperturbative nature of the problem, and reflect the presence of several competing physical mechanisms for even the simplest models. The interplay of localization and lattice coherence, of quantum and spatial fluctuations, and of various competing types of long-range order are important examples. Numerous approximation schemes (see e.g. [57]) have been employed to circumvent these difficulties, but all of them are not based on some controlled limit, i.e. some extreme limit of the model is considered wherein the problem simplifies and can be solved in a controlled manner. The reason to favor these approaches is not that of out-of-place mathematical rigor, but rather that it is often easier to identify which of the physical aspects of the problem will be privileged by a specific limit, and thus to choose that specific limit best adapted to the physical phenomenon under consideration. In favorable cases, the physical ingredients that have been left out can be reintroduced by expanding around this starting point.

The increase of computational power has also stimulated a direct numerical solution of these models using exact diagonalization (see sec. 2.2.1) and quantum Monte Carlo methods (see sec. 2.2.3). However, the exact diagonalization technique is limited by the exponential growth of the computations with system size, while the quantum Monte Carlo method is restricted to rather high temperatures by the minus-sign problem. Despite the interest of these numerical studies, these limitations have often prevented the extraction of reliable low energy information.

Dynamical Mean-Field Theory (DMFT) [1, 18] is a new approach to the problem of strong correlations that has been developed over recent years and has led to some progress in our understanding of these systems. The essential idea is to replace a lattice model by a single-site quantum impurity problem embedded in an effective medium determined self-consistently [3]. The impurity model offers an intuitive picture of the local dynamics of a quantum many-body system. The self-consistency condition captures the translation invariance and coherence effects of the lattice [22].

Actually a mean-field theory reduces a many-body lattice problem to a single-site problem with effective parameters. Consider the classical theory of magnetism as an analogy: Spin is the relevant degree of freedom at a single site and the medium is represented by an effective magnetic field (the classical mean field). In the fermionic case, the degrees of freedom at a single site are the quantum states of the atom inside a selected central unit cell of the crystal; the rest of the crystal is described as a reservoir of noninteracting electrons that can be emitted or absorbed by correlated site.

The dynamical mean-field theory becomes exact in the limit of large spatial dimensions $d \to \infty$ [1], or more appropriately in the limit of large lattice coordination (note that the coordination z is already quite large for several three-dimensional lattices: z=6 for a cubic lattice, z=12 for a face-centered-cubic lattice). This ensures the internal consistency of the approach and establishes 1/z as a control parameter.

The main merit of the DMFT approximation is a proper description of typical correlation problems such as the Mott transition and possibility to treat a realistic models of actual materials, taking into account several orbitals, and specific lattice structure and density of states, as obtained, e.g., from local density approximation (LDA) calculations [4, 5].

5.2 Dynamical mean-field theory

The main idea of a mean-field theory is to approximate a lattice problem with many degrees of freedom by a single-site effective problem with less degrees of freedom. Thus the dynamics at a given site can be represented as the interaction of the degrees of freedom at this site with an external bath formed by all other degrees of freedom in crystal.

Proposed as an exact solution of Hubbard model in infinite dimensions [1, 18], DMFT become a very powerful tool for investigation of lattice models of correlated electrons. In DMFT the lattice model is mapped on an effective quantum impurity model in a bath which has to be determined self-consistently.

Let us consider the Hubbard Hamiltonian:

$$H = \sum_{ij\sigma} t_{ij} c^{\dagger}_{i\sigma} c_{j\sigma} + U \sum_{i} c^{\dagger}_{i\uparrow} c_{i\uparrow} c^{\dagger}_{i\downarrow} c_{i\downarrow}. \tag{5.1}$$

It is the simplest model of interacting electrons on a lattice. The t_{ij} matrix element describes hopping of electrons with spin s between sites i and j. The second term in (5.1) is a local Coulomb interaction U between two electrons occupying the same site i.

For simplicity it is assumed, that no symmetry breaking occurs, i.e. we have translation-invariant paramagnetic phase.

In dynamical mean-field description the Hamiltonian (5.1) can be described as an impurity in some effective field.

The imaginary-time action of this system reads as (2.18), where $\mathcal{G}^{-1}_{imp}(i\omega_n) = i\omega_n + \mu -$

$\Delta_\sigma(i\omega_n)$ plays a role of the effective field. In other words, the Anderson impurity model (see Chapter 4) can be a reference system for the Hubbard model because it yields the exact local Green function in DMFT when the hybridization function $\Delta(i\omega_n)$ fulfills a self-consistency condition [2, 3]:

$$G_{loc}(i\omega_n) = \sum_{\mathbf{k}} (G_0^{-1}(\mathbf{k}, i\omega_n) - \Sigma(i\omega_n))^{-1}, \tag{5.2}$$

where $G_0(\mathbf{k}, i\omega_n) = (i\omega_n + \mu - t_{\mathbf{k}})^{-1}$ is non-interacting **k**-dependent Green function of the initial lattice problem in tight binding scheme and can be obtained, for example, from LDA calculation. The $\Sigma(i\omega_n))$ is frequency-dependent self-energy (5.5). The initial guess for Σ in the first iteration is usually zero. The bath Green function obtained from solution of effective impurity problem with no local Σ:

$$\mathcal{G}_{imp}^{-1}(i\omega_n) = G_{loc}^{-1}(i\omega_n) + \Sigma(i\omega_n). \tag{5.3}$$

After we find the bath Green function, we approach the most non-trivial part of the DMFT loop: solving of the corresponding impurity model taking into account electronic correlations. Using bare green function $\mathcal{G}_{imp}(i\omega_n)$ as an input ($\mathcal{G}_{imp}(i\omega_n) = G_{loc}(i\omega_n)$ at the first DMFT iteration), as an output the impurity solver produces

$$G_{imp}(\tau) = -\left\langle T_\tau c(\tau) c^\dagger(0) \right\rangle_{S_{imp}}. \tag{5.4}$$

This is an interacting Green function of the reference impurity problem. The energy-dependent self-energy $\Sigma(i\omega_n)$ is obtained in the following way:

$$\Sigma(i\omega_n) = \mathcal{G}_{imp}^{-1}(i\omega_n) - G_{imp}^{-1}(i\omega_n) \tag{5.5}$$

Usually one have to use Fourier transform to obtain $G_{imp}(i\omega_n)$ on Matsubara frequencies from the imaginary time result $G_{imp}(\tau)$. However in the CT-QMC method this transformation is performed analytically (2.46) and we get rid of additional numerical errors caused by this operation. It leads to significant reduction of the numerical noise in $\Sigma(i\omega_n)$ (see Fig. 5.1, lower panel) and, as a consequence, our DMFT-loop reach self-consistency much faster then using, e.g. Hirsch-Fye QMC as an impurity solver.

Since the self-energy (5.5) is used for construction of new bath Green function for the reference impurity problem (5.2), the equations (5.2, 5.3, 5.5) make up the DMFT loop.

When a self-consistency condition is fulfilled, i.e. all the quantities in Eqs. (5.2, 5.3, 5.5) converges to some stable values and do not changes from one DMFT iteration to another, the (5.2) become the final local Green function for Hubbard model in DMFT approximation.

The DMFT is exact in the limit of infinite coordination number (or infinite dimensions). For any finite-dimensional system, DMFT is an approximation as it fails to take into account non-local fluctuations, like Cooper pairing or antiferromagnetic correlations. Nevertheless, it can be used as a reasonable starting point in many cases.

5.3 Two- and three-band lattice model, orbital selective metal-insulator transition

The Mott metal-insulator transition plays an important role in the physics of strongly correlated solids [115]. At a qualitative level, localization of the electrons can occur when the kinetic energy gain (typically given by the bare bandwidth) is smaller than the cost in on-site repulsive Coulomb energy (U). Although simplified models like one-band Hubbard model advance our understanding of correlated phenomena in solids, in real materials however, such as transition metal oxides, several orbital components are involved. However, most attention has focused on the one-orbital case, in part because of its presumed relevance to high temperature superconductivity [133] and in part because appropriate theoretical tools for the multiorbital case have until recently not been available. This focus on the one-band case is limiting: in most Mott systems more than one orbital is relevant and the orbitals are occupied by more than one electron or hole. Intuition gained from studies of single-orbital models may not necessarily carry over to the multiorbital case [134, 135, 136]. One of the reasons of such behavior of multiorbital system is emerging of additional degree of freedom and energy scale, namely Hund exchange J. Furthermore, the inter-site hopping amplitudes can be significantly different for different orbital functions (due e.g to their relative orientations). It is therefore essential to understand how these effects can affect behavior of the correlated solid's properties and whether qualitatively new effects are possible when the orbital degeneracy is lifted. Removing of orbital degeneracy can lead to variety of interesting effects, such as orbital ordering [137], orbital selective Mott transition (OSMT) [138, 139], etc. Some works on this subject were done omitting exchange and pair hopping terms [136], but a reliable extension of these results to the rotationally invariant model in the strong coupling regime has until recently not been possible. On a technical level, multiorbital models are more difficult to study both because of the larger number of degrees of freedom, and because the physically important exchange and pair-hopping terms are not easy to treat by standard Hubbard-Stratonovich methods [72, 140].

We use the CT-QMC method with the full rotationally invariant interactions (Eq. (4.1)). To benchmark our method we performed a DMFT calculation of 2-band strongly anisotropic lattice model: both bands are at half-filling and their bandwidth are $W_1 = 2\ eV$ and $W_2 = 0.2\ eV$, i.e. the hoppings between the lattice sites differs by factor of 10 for the different orbitals. The inverse temperature $\beta = 30\ eV^{-1}$ corresponds to temperature $T \approx 350\ K$ that is already close to the room temperature. The Coulomb interaction strength $U = 1.2\ eV$, exchange parameter $J = 0.2\ eV$, interaction part of the Hamiltonian is of the form (4.1). The resulting local DOS as well as local Green functions are presented on Fig. 5.1. In this region of parameters we have very pronounced orbital-selective metal-insulator transition: The broad band is conductive and the narrow one is a Mott insulator. Moreover the Luttinger sum rule (”pinning condition”) is violated due to the interorbital coupling and relatively large temperature, and this fact is in good agreement with known results [141, 142].

Next we consider three-orbital lattice model. We fitted the chemical potential to get a non-integer occupancy. This model corresponds to doped Hubbard model in infinite dimensions.
We choose the parameters to bring all the orbitals to strong correlated regime: two (broad) bands are degenerated and their bandwidth is $W_1 = W_2 = 2\ eV$, the third (narrow) band has a bandwidth $W_3 = 0.2\ eV$. The inverse temperature $\beta = 10\ eV^{-1}$ corresponds to temperature $T \approx 1160\ K$ The Coulomb interaction strength $U = 2.7\ eV$, exchange parameter $J = 0.7\ eV$, interaction part of the Hamiltonian is of the form (4.1). In our case the occupancy is set to $n = 1.4$ electrons pro all 3 orbitals. The results are presented on the Fig. 5.2. The occupancy of the narrow orbital (red) is 1 electron ($n_{narrow} = 1/2$ pro state, half-filled case) and the broad orbitals (black) contains approximately 0.4 electrons on both orbitals ($n_{broad} \approx 0.1$ pro state). The narrow orbital became insulating, (Fig. 5.2, inset) whereas the broad ones remains conducting and form a pseudogap at the Fermi level. For the undoped model (see Fig. 5.3) our system becomes an insulator: narrow band is still a Mott insulator and the broad ones are pushed out over the Fermi level. The corresponding occupancies are $n_{narrow} = 1/2$ and $n_{broad} = 0$. Notice, that the particular model has $U/D = 2.7$ ratio for broad orbitals, that is much lower than the critical value for the degenerated half-filled 3-band model $U_c/D \approx 6.5$ [143].

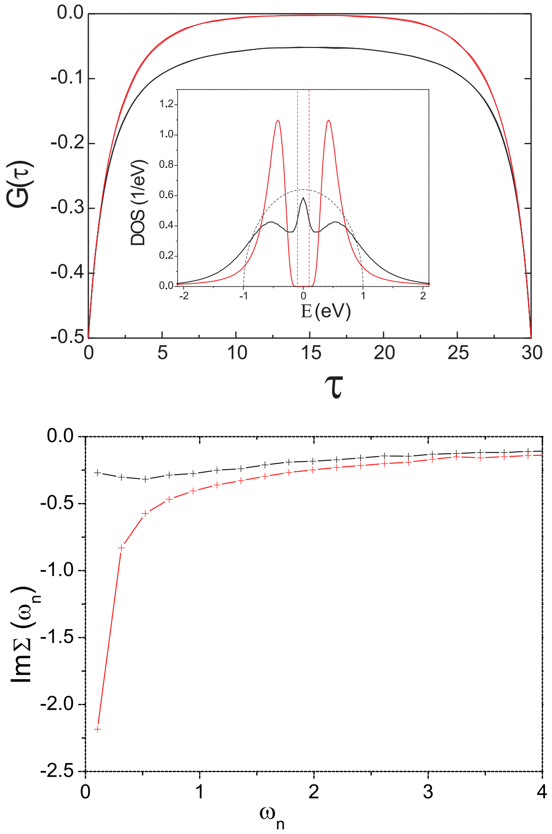

Figure 5.1: Results for 2-band interacting lattice model in DMFT approximation. Model parameters: Initial bandwidth $W_1 = 2\ eV$, $W_2 = 0.2\ eV$. On-cite Coulomb repulsion: $U = 1.2\ eV$, Hund exchange $J = 0.2\ eV$, the system is at half-filling. Inverse temperature $\beta = 30\ eV^{-1}$ ($T \approx 350\ K$). Upper panel, main graph: interacting imaginary time impurity Green function $G(\tau)$ (5.4) for both orbitals, τ in eV^{-1}. Upper panel, inset: Orbital-resolved DOS. Dash lines denotes initial (non-interacting) local density of states of a lattice site. Lower panel: Imaginary part of self-energy $\Sigma(i\omega_n)$ on Matsubara frequencies, ω_n in eV. Black lines corresponds to broad band, red - to the narrow one. The Fermi energy corresponds to zero.

5.4 Role of spin-flips in Sr_2RuO_4

The interest to the Sr_2RuO_4 compound emerged in the middle of 90's, when it was found, that at temperatures below 1K this compound becomes superconductive [144]. There is still a possibility, that studying of this system can help to understand the mechanism of high-T_c superconductivity. However 4d states of Ru in the compound are more broad than the 3d states in high-T_c cuprates.

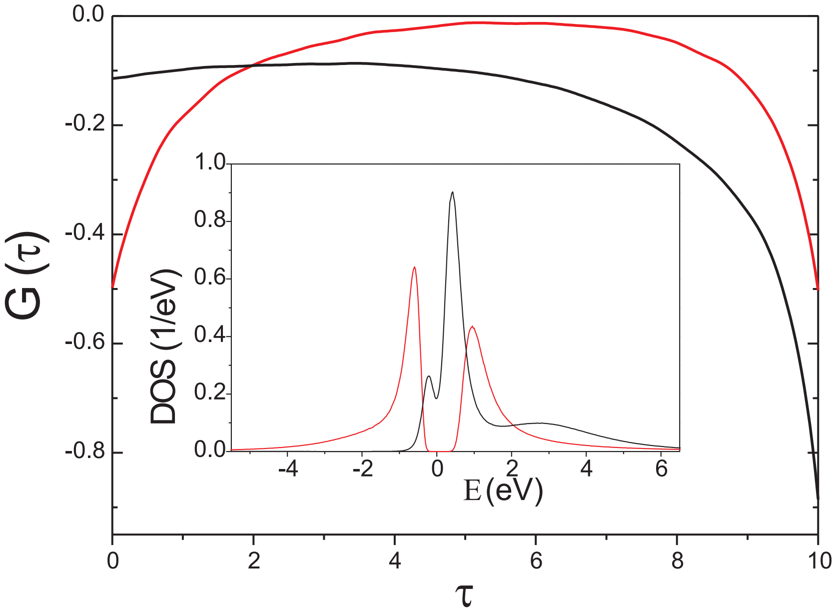

Figure 5.2: Results for 3-band interacting lattice model in DMFT approximation, doped regime – total site occupancy is $n_{tot} \approx 1.2$ electrons. Model parameters: Initial bandwidth $W_1 = W_2 = 2\ eV$, $W_3 = 0.2\ eV$. On-cite Coulomb repulsion: $U = 2.7\ eV$, Hund exchange $J = 0.7\ eV$. Inverse temperature $\beta = 10\ eV^{-1}$ ($T \approx 1160\ K$). The orbital occupancies are $n_1 = n_2 \approx 0.1$, $n_3 = 1/2$. Main graph: interacting imaginary time impurity Green function $G(\tau)$ (5.4) for all orbitals, τ in eV^{-1}. inset: Orbital-resolved DOS. The narrow orbital (red) has a gap on the Fermi level whereas the broad orbitals (black) form pseudogap but still remains conductive. Black lines corresponds to broad bands, red - to the narrow one. The Fermi energy corresponds to zero.

The first-principle LDA calculation of the electronic structure of Sr_2RuO_4 [145] is based on density functional theory (DFT) within the LDA approximation [10] using the linearized muffin-tin orbitals (LMTO) method. [146] The partial densities of states for Sr_2RuO_4 are shown in Fig. 5.4. The strontium 4d states are almost empty and lie above 3 eV; the O-2p derived bands are filled and extend from $-8\ eV$ to $-1\ eV$.

Due to the crystal field symmetry the Ru-4d states splits into t_{2g} and e_g orbitals (see Fig. 5.5). Since two e_g bands lie above the three t_{2g} bands in the energy region from 0.5 eV to 5 eV, four Ru-4d electrons occupy three t_{2g} bands (d^4 configuration). The partially filled ruthenium 4d-states are the most interesting from the point of view of correlation effects. The layered crystal structure of Sr_2RuO_4 results in further splitting of t_{2g} orbitals: the xy orbital is almost two-

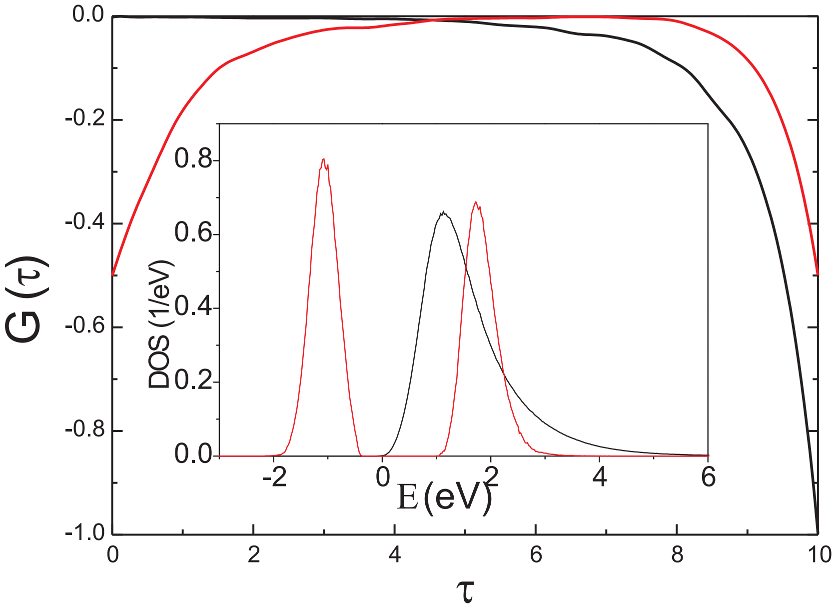

Figure 5.3: Results for 3-band interacting lattice model in DMFT approximation, undoped regime – total site occupancy is $n_{tot} = 1$ electron. Model parameters: Initial bandwidth $W_1 = W_2 = 2\ eV$, $W_3 = 0.2\ eV$. On-cite Coulomb repulsion: $U = 2.7\ eV$, Hund exchange $J = 0.7\ eV$. Inverse temperature $\beta = 10\ eV^{-1}$ ($T \approx 1160\ K$). The orbital occupancies are $n_1 = n_2 = 0$, $n_3 = 1/2$. Main graph: interacting imaginary time impurity Green function $G(\tau)$ (5.4) for all orbitals, τ in eV^{-1}. inset: Orbital-resolved DOS. The narrow orbital (red) has a gap on the Fermi level whereas the broad orbitals (black) became a band insulator. Black lines corresponds to broad bands, red - to the narrow one. The Fermi energy corresponds to zero.

dimensional while the xz, yz orbitals have nearly one-dimensional character (see Fig. 5.5). The initial (non-interacting) DOS for the correlation problem was obtained by Pchelkina et al. [145] using Wannier functions formalism [147] which allows one to project the Hamilton matrix from the full-orbital space to a selected set of relevant orbitals.

The experiments [148, 149] shows the presence of correlations in Sr_2RuO_4: the quasiparticle (QP) weight is 3-4 times larger than the results obtained from standard band calculations and position of the QP peak is at Fermi energy or $\approx 10\ meV$ above, whereas tight-binding (TB) calculation gives $\approx 100\ meV$ [122] and realistic LDA calculation gives even larger ($\approx 200\ meV$, [145]) shift of the peak. It means that correlations plays a crucial role in understanding of the material's properties [145].

There were a number of theoretical works on Sr_2RuO_4 in a framework of the DMFT scheme

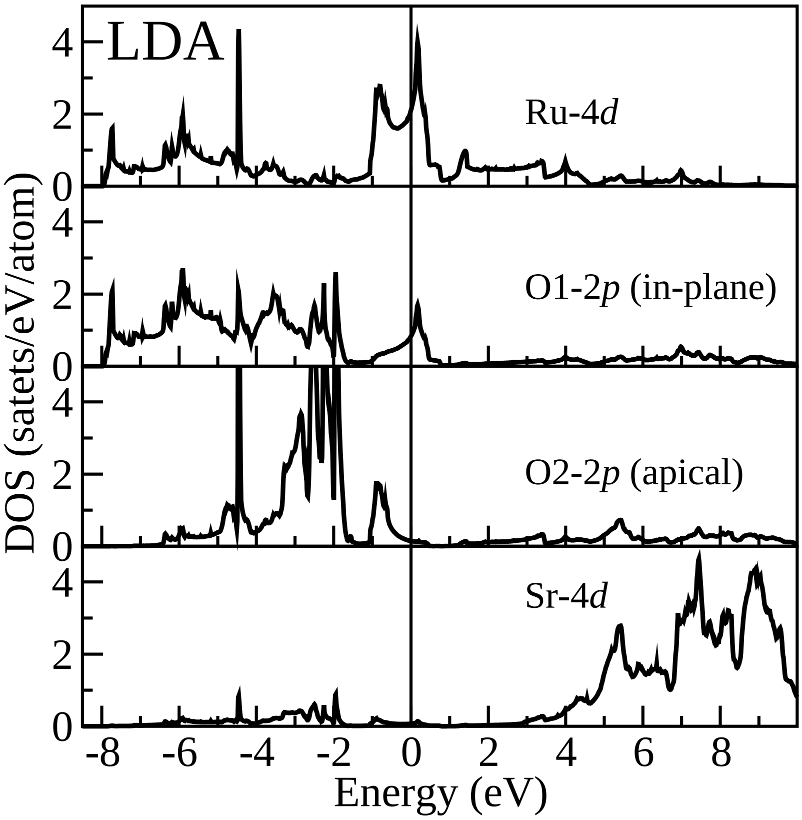

Figure 5.4: Partial LDA DOS for Sr_2RuO_4. The partially filled ruthenium 4d-states are the most interesting from the point of view of correlation effects [145]. The Fermi level corresponds to zero. From Ref. [145].

in order to investigate many-body effects leading to unusual spectral properties of this compound mentioned above. As a many-body impurity solver were used the Hirsch-Fye QMC approach [145] and finite temperature exact diagonalization method [150].

In the work [145] Hirsch-Fye QMC solver was used. The limitations of this method (see sec. 2.2.3) have lead to impossibility of including fully rotationally invariant interaction – spin flips and pair hoppings terms were omitted, i.e the interaction part of Hamiltonian was of the form (4.1), but without last term. The model parameters were following: inverse temperature was $\beta = 10\ eV^{-1}$, the number of imaginary time slices was 40 ($\Delta\tau = 0.25\ eV^{-1}$), Coulomb interaction parameters were $U = 3.1\ eV$, $J = 0.7\ eV$. The result of that calculation is presented on Fig. 5.7.

Another recent attack on this problem was done by Liebsch and Ishida [150]. They used

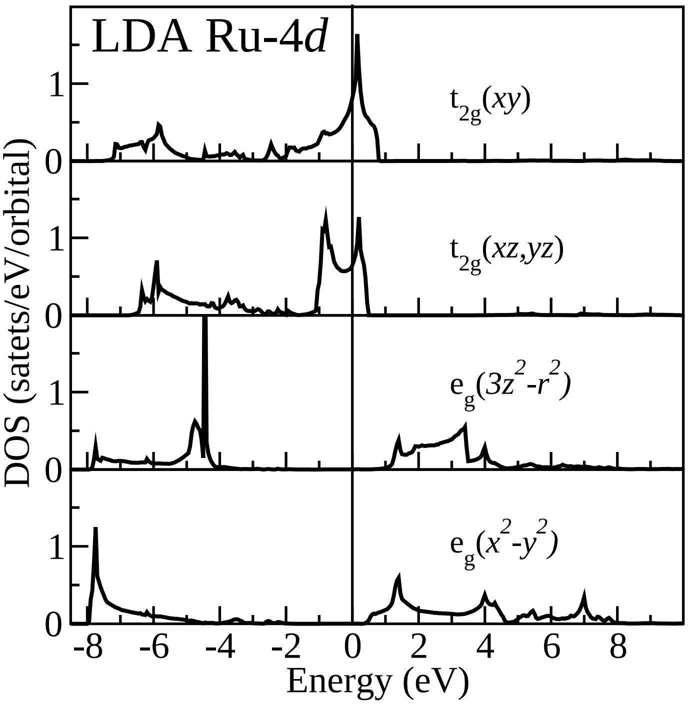

Figure 5.5: Orbitally projected LDA Ru-4*d* DOS. Only *xy*, *xz* and *yz* orbitals contributes to the DOS at Fermi level. The Fermi level corresponds to zero. From Ref. [145].

finite temperature exact diagonalization technique as an impurity solver for the DMFT loop. Their solver allowed to include full Coulomb matrix, but the bath DOS was (strongly) discretized in order to represent it as a finite set of levels. The first fact made possible to obtain very reach structure of all the many-particle states, but the second, although allowing to perform the exact diagonalization of the system's Hamiltonian in finite (and relatively small) Hilbert space, led to very spiked local DOS, corresponding rather to the solution of the local problem, not the band one (see Fig. 5.8).

In the CT-QMC formalism we can perform calculation of the spectral properties of the system with full Coulomb matrix and without any artificial discretization of the input DOS of non-interacting system.

In order to understand how the spin-flips and pair hopping terms influence on the spectrum of the system, we performed a number of calculations with different interaction Hamiltonians: with and without spin-flip and pair hopping terms. To distinguish effects caused by shape of the non-interacting bath DOS, all the calculations were don for two bath DOS: first was an

LDA result from Ref. [145] (see Fig. 5.6, solid line) and the second from Ref. [122] (see Fig. 5.6, dash line). From the Fig. 5.8 one can conclude that this system has a very reach structure of many-particle states and it can lead to strong temperature dependence of the system's spectrum. Therefore we performed two series of calculations: for inverse temperature $\beta = 5\ eV^{-1}$ ($T \approx 2300K$) and $\beta = 10\ eV^{-1}$ ($T \approx 1160K$). The choice of so high temperatures is determined by limitations of the computational effort: all the results presented in this chapter were produced on a dual-processor workstations with AMD Opteron 1.8 GHz CPU's. The usual time pro one DMFT iteration was 10-20 hours.

The interaction part of the Hamiltonian is of the rotationally invariant form (4.1). The values of the orbitally averaged Coulomb interaction parameter $\bar{U} = 1.7\ eV$ and Hund exchange energy $J = 0.7\ eV$, the same as in [145], were obtained from constrained LDA calculations [123, 151]. In the particular case of three t_{2g}-orbitals $\bar{U}$ is equal to the inter-orbital Coulomb interaction U'. [4, 5] Thus we obtain $U = U' + 2J = 3.1\ eV$ for the local intra-orbital Coulomb repulsion.

Since the one-electron Hamiltonian is diagonal in **k** space [122], we can use the following realization of the DMFT: The DOS resulting from LDA calculations is connected to a non-interacting bath Green function of *Ru* the following way: $N_m(E) = -\frac{1}{\pi} Im(G_m(E))$, where m is orbital index. Thus in order to obtain bath green function on Matsubara frequencies for CT-QMC solver we need to perform the Hilbert transform. In general form it reads $G(z) = \int_{\infty}^{-\infty} \frac{N(E)}{z-E} dE$. For our purpose one have to use $z = i\omega_n + \mu - \Sigma(i\omega_n)$, where $\omega_n = (2n+1)\pi T$ is Matsubara frequency, μ is a chemical potential and $\Sigma(i\omega_n) = \mathcal{G}^{-1}(i\omega_n) - G^{-1}(i\omega_n)$ is a self energy. In other words, instead of Eq. (5.2) we use local Green function of the following form:

$$G^m_{loc}(i\omega_n) = \int_{-\infty}^{\infty} dE \frac{N^{bath}_m(E)}{i\omega_n - \Sigma_m(i\omega_n) - E}, \tag{5.6}$$

where $N^{bath}_m(E)$ is non-interacting bath DOS of the corresponding orbital (m).

To distinguish the effects caused by spin-flip and pair-hopping terms, the last item in (4.1) was omitted and DMFT calculations with density-density Coulomb interaction have been performed. First we have done DMFT calculation for bath Green function obtained in LDA approximation [145], using full and density-density Coulomb interaction (with or without last item of (4.1)). Resulting DOS is presented on Fig. 5.9, left panel.

The hybridization due to interorbital Coulomb interaction leads to complete different spectra in comparison to LDA and TB non-interacting results. The DOS features that were apart from

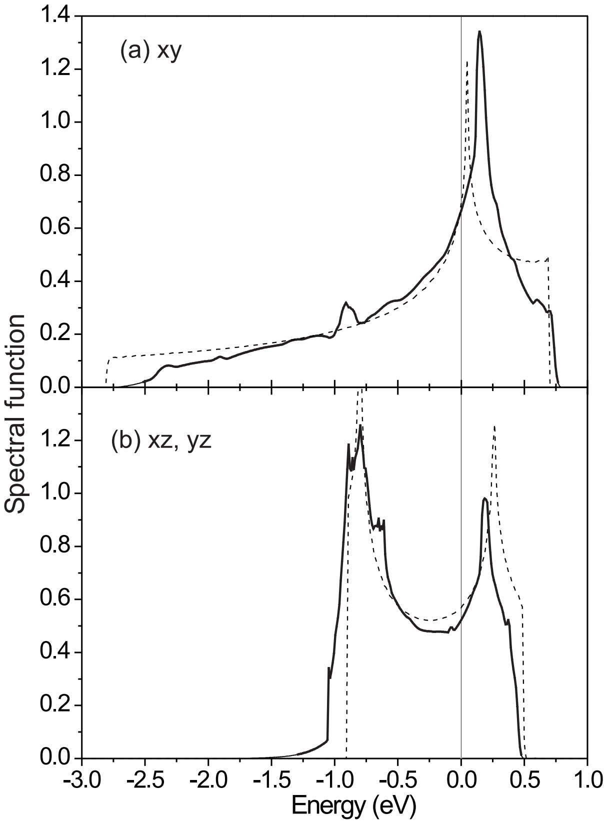

Figure 5.6: Density of states of of non-interacting system. Solid line – LDA results from Ref. [145], dash line – tight binding model from Ref. [122] Upper panel: *xy* orbital, lower panel: *xz* and *yz* orbitals.

the Fermi level (especially on *xz* and *yz* orbitals) moves towards the Fermi level and form a quasiparticle peak, the upper (UHB) and lower (LHB) Hubbard bands appears (compare figs. 5.6 and 5.9, left panel).

The result for diagonal Coulomb matrix is in qualitative agreement with with one of Hirsch-Fye QMC calculation by Pchelkina et al. [145]. The deviations can be attributed to big difference of temperature (by factor of 2). Including of the spin-flip terms have almost no effect on *xy* orbital (see fig 5.9 left panel, (a)), only small weight transfer from the satellite peaks at -1 and 1.7 eV occurs. The LHB stays almost unchanged at -4.3 eV. The derivative of self energy with respect to Matsubara frequency $\left.\frac{\partial Im\Sigma(i\omega)}{\partial(i\omega)}\right|_{\omega=\omega_1}$ is positive and the (5.7) definition of the quasiparticle residue makes no sense. This fact can have two possible reasons: either we are at very high temperature and cannot catch the low-temperature behavior, or our system tends to have a pseudogap. The *xz* and *yz* orbitals (see Fig. 5.9 left panel, (b)) are more sensitive

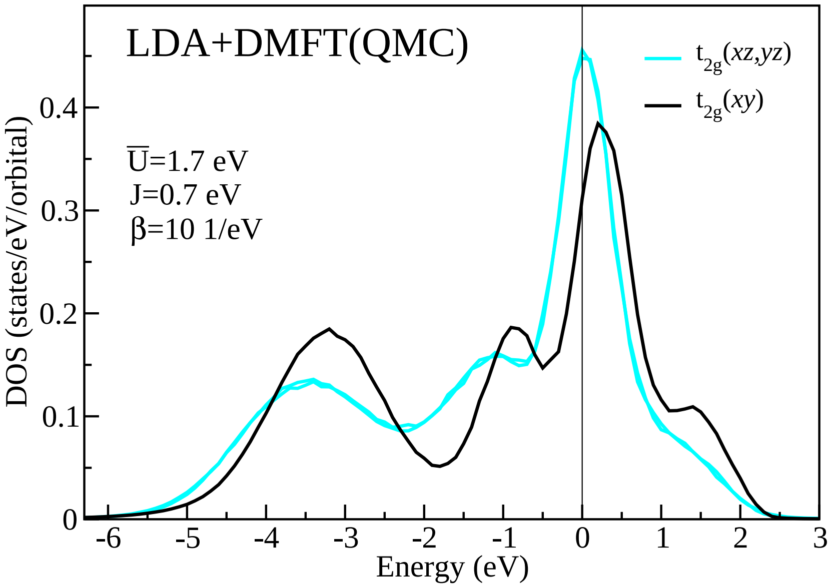

Figure 5.7: Ru-4d(t_{2g}) spectral functions obtained within LDA+DMFT (Hirsch-Fye QMC) by Pchelkina et al. [145]. Dark curve: *xy* orbital, light curve: *xz*, *yz* orbitals; interaction parameters: $U = 3.1$ eV, $J = 0.7$ eV; inverse temperature $\beta = 10$ eV^{-1} ($T \approx 1160$ K). The Fermi level corresponds to zero. From Ref. [145].

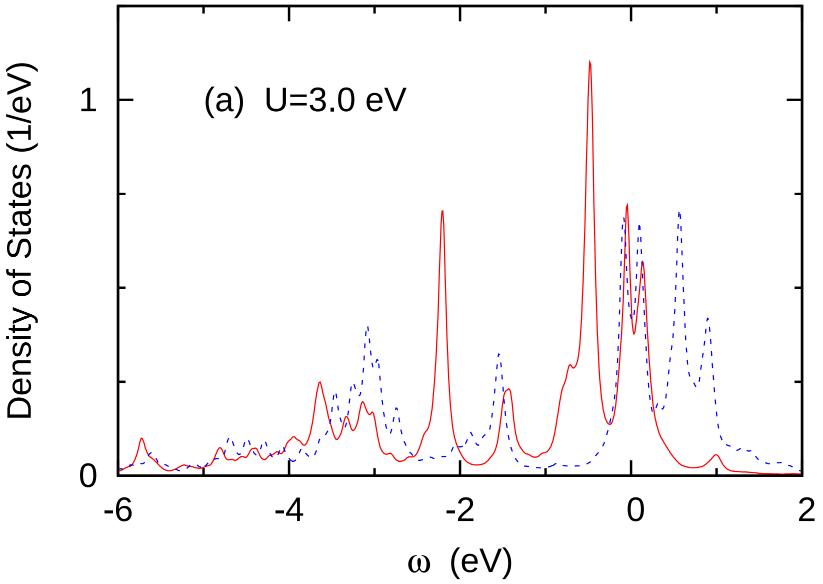

Figure 5.8: Quasi-particle spectra is calculated using ED/DMFT at $\beta = 50$ eV^{-1} ($T \approx 220$ K), $U = 3.0$ eV. Solid (red) curves: d_{xy} band, dashed (blue) curves: $d_{xz,yz}$ bands. From Ref. [150].

to form of Coulomb interaction. It leads to slight narrowing of the peak hear the Fermi level and the LHB shifts by 0.2 eV: from -3 to -2.8 eV (see fig 5.9 left panel, (b)). Moreover, the quasiparticle weight (calculated by the (5.7) formula, see Tab. 5.1) of these orbitals slightly decreases with including the spin-flip terms: from $Z_{diag} = 0.99$ for density-density Coulomb interaction to $Z_{full} = 0.95$ in case of full Coulomb vertex. The quasiparticle weight here is calculated using approximative formula [3]:

$$Z = \left[1 - \frac{\partial Im\Sigma(i\omega)}{\partial(i\omega)} \bigg|_{\omega=\omega_1} \right]^{-1}. \tag{5.7}$$

To check the results presented above we performed the calculation with tight-binding model bath DOS from [122]. Results are presented on Fig. 5.9, right panel. The spin-flip effects are qualitatively the same as in previous calculation, but much more pronounced. The xy orbital undergoes almost no changes, the LHB position is -4.4 eV, UHB is at 1.6 eV and the satellite peak is at -1 eV. The self energy exhibit the same behavior as in the previous case.

On xz and yz orbitals including of spin-flip terms lead to smearing of the satellite peak at -0.7 eV and shifting of the LHB from -3.5 eV to -3.3 eV. Note that this shifting (0.2 eV) is the same as in the case of realistic bath DOS.

The splitting between LHB of xy orbital and LHB of xz, yz orbitals is increased from 1.1 eV for realistic bath DOS to 1.5 eV for the model (TB) one. The quasiparticle renormalization of the xz and yz orbitals is of the same order as in the previous case: from $Z_{diag} = 0.99$ for density-density Coulomb interaction to $Z_{full} = 0.96$ in case of full Coulomb matrix.

Lowering the temperature ($\beta = 10$) in case of LDA bath DOS has the following consequences: LHB of the xy orbital moves to -2.7 eV for full Coulomb interaction and to -2.5 eV for diagonal one (see fig 5.10 left panel, (a)). When including spin-flip terms to the Coulomb interaction the satellite peak in the xy orbital moves from -0.3 eV to -0.2 eV and becomes more pronounced; the xy orbital becomes more correlated: its quasiparticle weight decreases from $Z_{diag} = 0.91$ to $Z_{full} = 0.84$.

The xz and yz orbitals in this case are also more correlated than the xy one: their quasiparticle residues without and with spin-flip terms are $Z_{diag} = 0.91$ and $Z_{full} = 0.84$ correspondingly. The LHB of these orbitals moves from -3.2 eV to -2.6 eV and the UHB at 1.5 eV becomes more pronounced (see fig 5.10 left panel, (b)). Finally the shifting of the QP peak partially below the Fermi level caused by non-diagonal terms of Coulomb interaction is observed on xz and yz orbitals.

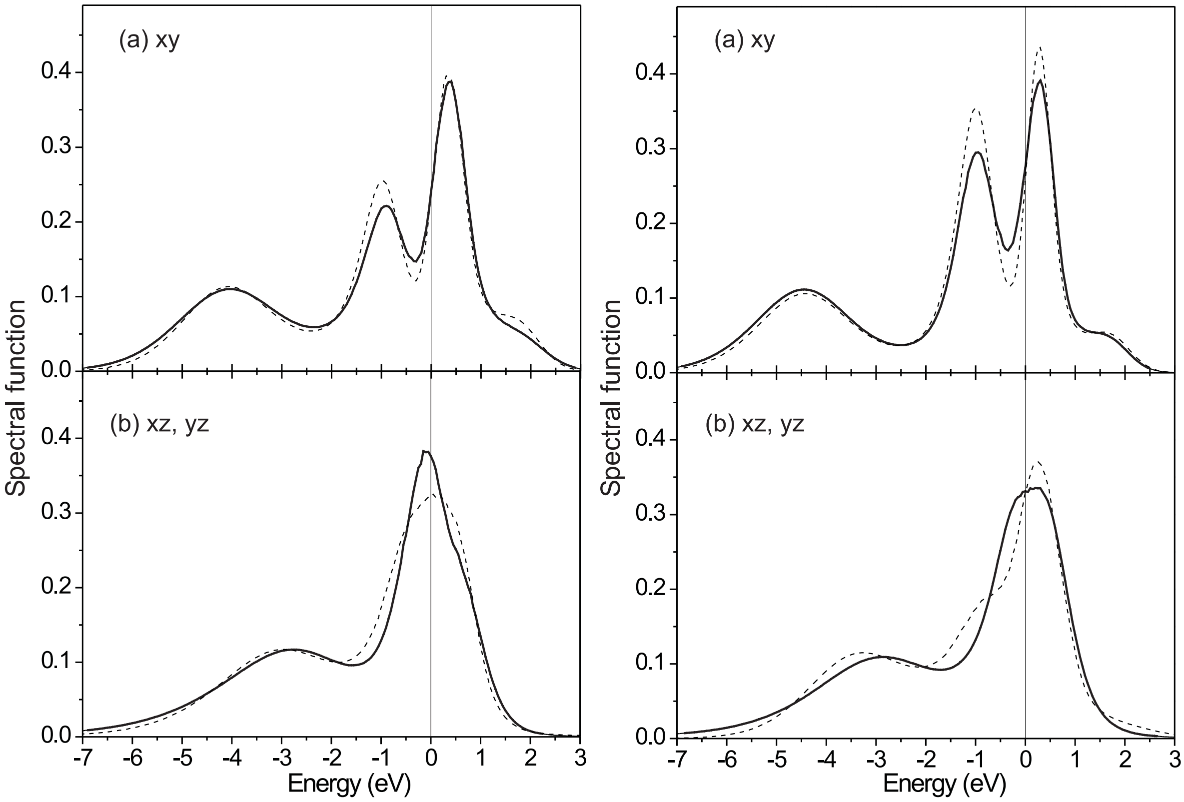

Figure 5.9: Density of states of interacting Ru-4d(t_{2g}) orbitals. Left Panel: bath Green function is taken from LDA calculations [145]. Right panel: bath Green function is taken from TB calculations [122]. Model parameters are following: inverse temperature $\beta = 5\ eV^{-1}$ ($T \approx 2300\ K$). The interaction parameters are $U = 3.1\ eV$, $J = 0.7\ eV$. Solid line denotes rotationally invariant interaction (4.1), dash line – density-density one (without last item in (4.1)). Upper graphs: *xy* orbital, lower graphs: *xz* and *yz* orbitals.

The last series of calculations have been performed for TB bath DOS with the same parameters ($U = 3.1\ eV$, $J = 0.7\ eV$, $\beta = 10\ eV^{-1}$ ($T \approx 1160\ K$)) and full U matrix (see fig 5.10, right panel). In this case on *xy* orbital the LHB at $-2.8\ eV$, UHB at $1.5\ eV$ and the satellite peak at $-0.7\ eV$ become more pronounced (see fig 5.10 right panel, (a)). Position of the LHB of *xz*, *yz* orbitals is $-2.5\ eV$ and UHB is at $1.7\ eV$, quasiparticle weight were from $Z_{xy} = 0.84$ to $Z_{xz,yz} = 0.74$.

The quasiparticle weights of the Ru-4d(t_{2g}) orbitals obtained in DMFT approximation for full (with spin-flip terms) and diagonal Coulomb interaction and for bath DOS obtained in LDA approximation [145] or from tight-binding model [122] are presented in Tab. 5.1. The N/A

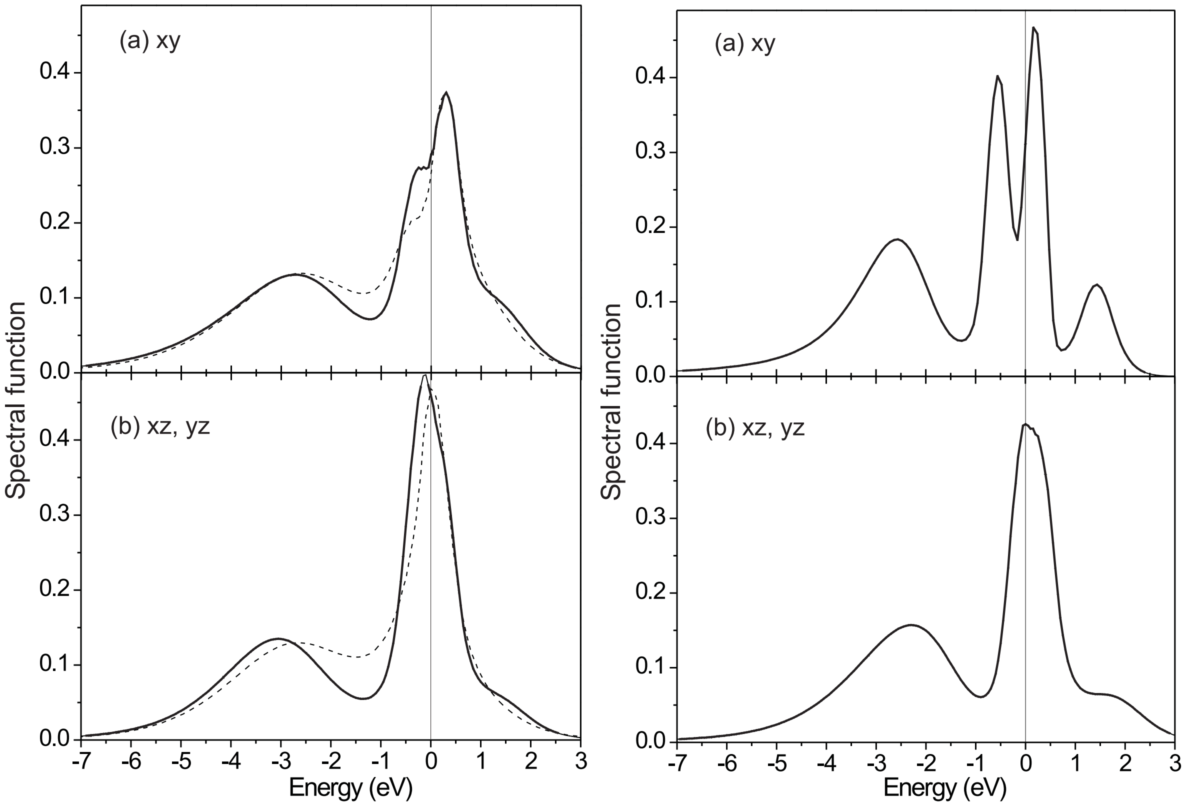

Figure 5.10: Density of states of interacting Ru-4d(t$_{2g}$) orbitals. Left Panel: bath Green function is taken from LDA calculations [145]. Right panel: bath Green function is taken from TB calculations [122]. Model parameters are following: inverse temperature $\beta = 10\ eV^{-1}$ ($T \approx 1160\ K$). The interaction parameters are $U = 3.1\ eV$, $J = 0.7\ eV$. The bath Green function is taken from LDA calculations [145]. Solid line denotes rotationally invariant interaction (4.1), dash line – density-density one (without last item in (4.1)). Upper graphs: *xy* orbital, lower graphs: *xz* and *yz* orbitals.

Z		LDA		TB	
		xy	xz,yz	xy	xz,yz
$\beta = 5\ \ eV^{-1}$	diag	N/A	0.99	0.99	0.99
$\beta = 5\ \ eV^{-1}$	full	N/A	0.95	0.98	0.96
$\beta = 10\ eV^{-1}$	diag	0.91	0.82	0.96	0.84
$\beta = 10\ eV^{-1}$	full	0.84	0.76	0.84	0.74

Table 5.1: Values of the quasiparticle weight Z for different model parameters.

entry for xy orbital at $\beta = 5$ denotes that the self energy derivative $\left.\frac{\partial Im\Sigma(i\omega)}{\partial(i\omega)}\right|_{\omega=\omega_1}$ was negative and calculation of Z according to (5.7) definition was impossible. Analyzing this table we can conclude that xz and yz orbitals exhibit more correlated behavior than xy one. It can be attributed to the fact that non-interacting band DOS for these orbitals is almost twice more narrow than the xy one (see Fig. 5.6).

Another subject to analysis is structure of DOS. Whereas the lower Hubbard band has almost the same position in all the calculation series (it may contain some fine structure we can not resolve because the features of the maximum entropy method we are using for analytical continuation of the Green function to the real axis, see sec. 2.3.7), the DOS features near the Fermi level exhibit reasonable dependence on both interaction type (full or reduced) and bath DOS. In case of LDA bath DOS the results (see figs. 5.9 and 5.10, left panels) are qualitatively consistent with the DOS obtained by Hirsch-Fye QMC [145] (see Fig. 5.7). At high temperature ($\beta = 5\ eV^{-1}$, $T \approx 2300K$) the satellite peak on the xy orbital at $-1\ eV$ is reproduced with both types of Coulomb interaction we used. With lowering the temperature (to $\beta = 10\ eV^{-1}$, $T \approx 1160\ K$) this feature moves towards the Fermi level and becomes more sensitive to the type of Coulomb interaction (see Fig. 5.10, left panel): turning on the spin-flip terms leads to stronger hybridization between xy and xz, yz orbitals: position of the satellite peak on the xy orbital becomes almost the same as the maximum of quasiparticle peak on xz, yz orbitals, approximately at $-0.25\ eV$. It is in a good agreement with the ED-DMFT results if Liebsch and Ishida [150] (see Fig. 5.8): In their spectral function xy and xz, yz orbitals have almost the same structure near E_F. The similar situation takes place in case of TB bath DOS: at high temperature we have very pronounced satellite peak on the xy orbital at $-1\ eV$ (see Fig. 5.9, right panel) and at lower temperature this peak moves towards Fermi level and hybridization of xy and xz, yz orbitals takes place: the lower Hubbard bands are almost on the same position, at $-2.5\ eV$.

In this chapter we applied CT-QMC multiorbital solver to the lattice problem in DMFT approximation. We reproduced such features of the multiorbital Hubbard model in infinite dimensions as orbital-selective metal-insulator transition (OSMT), conductive character of doped Hubbard model in doped case and localization phenomena in non-doped one. Also the results for realistic model describing the Sr_2RuO_4 compound were reproduced and the influence of spin-flip terms on spectral function was studied. The method showed good precision within a reasonable computational effort.

6 Conclusions and outlook

In the present thesis we developed the weak-coupling continuous time quantum Monte-Carlo (CT-QMC) scheme for the general multiorbital impurity problem. We test this solver on a variety of physically interesting systems, such as two- and three-orbital impurities, a realistic Kondo problem of a cobalt atom in a copper matrix and multi-band correlated solids.

A number of technical problems related with the multi-band correlated problem have been solved. In order to obtain the full atomic-like Coulomb interaction, the matrix in complex harmonic basis was constructed and symmetrized. The fermionic sign problem was overcome by introducing additional α parameters to make all Coulomb interaction elements effectively negative. These parameters were applied not only to diagonal (density-density) Coulomb interaction elements, as in the one-band case, but also to spin-flip-like terms as well. A computationally inexpensive way to investigate spin susceptibilities has been developed.

In order to describe a single-spin Kondo impurity embedded into a conduction band with arbitrary density of electron states (DOS), we used the Abrikosov's transformation to get rid of spin operators in favor of fermionic ones. This led to an effective two-site Anderson impurity model, which can be easily solved by the CT-QMC scheme. The non-universality of the magnetic susceptibility behavior has been found in case of non-constant conduction electron DOS. We show a possibility of calculating different magnetic properties of interesting systems, like magnetic impurity in an ultrasmall grain and disordered Kondo alloys. The obtained results are in good agreement with other methods, such as exact diagonalization and numerical renormalization group.

We applied the multiorbital CT-QMC solver to the two-, three- and five-orbital Anderson Impurity models. The benchmark calculations in the atomic limit show a very good agreement with exact diagonalization results both in the half-filled case and away from half-filling. The effects of spin-flip terms and their interplay with coupling of the impurity to a conduction band of non-interacting electrons is studied. The role of singularities in the conduction band DOS on the impurity spectral function has been discussed.

A realistic Kondo model, namely a cobalt atom in a copper matrix, is considered. The effects caused by spin-flip terms of the Coulomb interaction are studied as a function of impurity occupancy, temperature, and strength of Coulomb interaction. Strong renormalization of initial DOS, obtained within the density-functional theory in the local density approximation, is found.

In order to calculate a properties of correlated solids, the multiorbital CT-QMC solver is used as a part of the self-consistent loop in dynamical mean-field theory. Benchmark calculations for two- and three-band correlated lattice model were performed. The orbital-selective Mott metal-insulator transition was reproduced. A calculation of a real solid, namely strontium ruthenate (Sr_2RuO_4), was performed. The influence of spin-flip terms of the Coulomb interaction as well as dependence of the result on initial non-interacting band DOS were studied. The obtained spectral functions are in a good agreement with previous studies.

We belive that the developed multiorbital CT-QMC method could be used to describe and predict spectral and magnetic properties of correlated nanosystems and solids. At the moment we are working on relativistic generalization of CT-QMC method for transition metals adatoms on metallic surfaces taking into account spin-orbital coupling. We will also extend the lattice problem algorithms using CT-QMC to systems with correlated f electron shell.

7 Appendix

Magnetic susceptibility calculation for Anderson impurity in the atomic limit.

Consider a simple one orbital AIM without coupling to any bath of free electrons. This system has only four states (see Fig. 7.1)

Magnetic susceptibility χ is given by

$$\chi = \left.\frac{\partial M}{\partial H}\right|_{H=0}, \tag{7.1}$$

where M is magnetization of the system and H is magnetic field applied to the system. Suppose that the magnetic field is applied along z axis. Than the magnetization is given by

$$M = \mu_B S_z \tag{7.2}$$

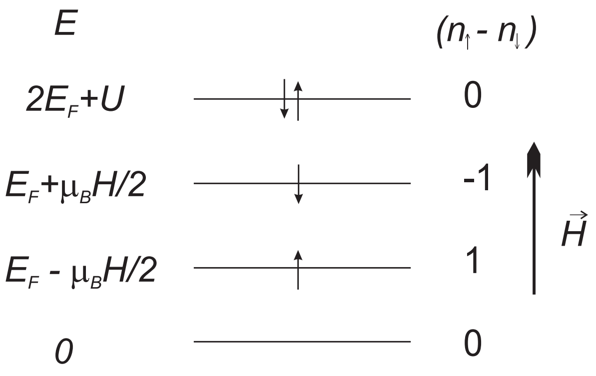

Figure 7.1: One orbital AIM without coupling to bath of free electrons.

where $S_z = (n_\uparrow - n_\downarrow)$. Thus

$$\langle M \rangle = \frac{Sp\left[Me^{-\frac{E}{k_B T}}\right]}{Sp\ e^{-\frac{E}{k_B T}}} = \frac{Sp\left[\mu_B(n_\uparrow - n_\downarrow)e^{-\beta E}\right]}{Sp\ e^{-\beta E}}$$

$$= \mu_B \frac{e^{-\beta E_F + \frac{\beta mu_B H}{2}} - e^{-\beta E_F - \frac{\beta mu_B H}{2}}}{1 + e^{-\beta E_F + \frac{\beta mu_B H}{2}} + e^{-\beta E_F - \frac{\beta mu_B H}{2}} + e^{-2\beta E_F - \beta U}}. \quad (7.3)$$

From (7.1) and (7.3) obtain:

$$\chi = \beta \mu_B^2 \frac{e^{-\beta E_F}}{1 + 2e^{-\beta E_F} + e^{-2\beta E_F - \beta U}}. \quad (7.4)$$

8 List of publications

A Journal contributions

P1 A. N. Rubtsov, M. I. Katsnelson, E. N. Gorelov, and A. I. Lichtenstein, ”Kondo effect in mesoscopic system” in: Electron Correlation in New Materials and Nanosystems (Springer, Berlin, NATO Science Series, Physics and Astronomy, Volume 241, 2007), ed. by K. Scharnberg and S. Kruchinin, p. 327.

P2 A. Zhuravlev, I. Zharekeshev, E. Gorelov, A. I. Lichtenstein, E. R. Mucciolo, S. Kettemann, ”Nonperturbative Scaling Theory of Free Magnetic Moment Phases in Disordered Metals”, cond-mat:0706.3456v1, accepted in Phys. Rev. Lett. (LF11622, 25 Oct. 2007).

P3 E. Gorelov, A. N. Rubtsov, M. I. Katsnelson and A. I. Lichtenstein, ”Relevance of the complete Coulomb interaction matrix for the Kondo problem”, submitted to Phys. Rev. Lett.

P4 E. Gorelov, A. N. Rubtsov, A.V. Lukoyanov, V.I. Anisimov and A. I. Lichtenstein ”Correlation effects in Sr_2RuO_4 : Continuous time QMC study”, submitted to Eur. Phys. J. B.

B Conference contributions

C1 E. Gorelov, A. Rubtsov and A. Lichtenstein, ”Continuous time quantum Monte Carlo scheme for Multiorbital Impurity Problems”, DPG - spring meeting of the Division Condensed Matter EPS - 21st General Conference of the Condensed Matter Division, Dresden, 30^{th} March 2006.

C2 E. Gorelov, H. Hafermann, A. Rubtsov, and A. Lichtenstein, ”Realistic Description of Magnetic Nanostructures in Metallic Environment”, SPS06, SPSTM-1, 4 International Conference on Scanning Probe Spectroscopy and 1 International Workshop on Spin-Polarized Scanning Tunneling Microscopy, Hamburg, 25^{th} July 2006.

C3 A. Zhuravlev, S. Kettemann, E. Mucciolo, E. Gorelov, and A. Lichtenstein, ”Spin Correlations and Free Magnetic Moments in Disordered Metals”, SPS06, SPSTM-1, 4 International Conference on Scanning Probe Spectroscopy and 1 International Workshop on Spin-Polarized Scanning Tunneling Microscopy, Hamburg, 25^{th} July 2006.

C4 E. Gorelov, H. Hafermann, A. Rubtsov and A. Lichtenstein, ”The Continuous Time Quantum Monte Carlo Impurity Solver – applications and results”, WE Heraeus Summerschool ”Computational Many Particle Physics”, Greifswald, 22^{nd} September 2006.

C5 H. Hafermann, E. Gorelov, A. Rubtsov and A. Lichtenstein, ”The Continuous Time Quantum Monte Carlo Impurity Solver – technical and computational aspects”, WE Heraeus Summerschool ”Computational Many Particle Physics”, Greifswald, 22^{nd} September 2006.

C6 E. Gorelov, H. Hafermann and A. Lichtenstein, ”Numerically exact scheme for the calculation of electronic structure and magnetic properties of correlated systems”, Conference on ”Computational Magnetism and Spintronics” CompMag 2006, Jülich, 3^{rd} October 2006.

C7 E. Gorelov, A. Zhuravlev, A. Rubtsov, and A. Lichtenstein, ”Quantum Monte-Carlo scheme for the solution of the Kondo impurity problem with an arbitrary density of free electron states”, DPG - spring meeting of the Division Condensed Matter, Regensburg, 28^{th} March 2007.

C8 E. Gorelov, A. Rubtsov and A. Lichtenstein, ”Continuous Time Quantum Monte Carlo for Multiorbital systems”, DFG workshop ”Realistic theory of electron correlations”, Prague, Czech Republic, 24^{th} May 2007.

C9 E. Gorelov, A. Lichtenstein, A. Rubtsov, V. Anisimov, A. Zhuravlev, A. Shick, ”Continuous Time Quantum Monte Carlo for Multiorbital systems”, Workshop ”Frontiers in Theoretical Magnetism II”, Uppsala, Sweden, 12^{th} October 2007.

Bibliography

[1] W. Metzner and D. Vollhard. Correlated lattice fermions in $d = \infty$ dimensions. *Phys. Rev. Lett.*, 62:324–327, 1989.

[2] G. Kotliar and D. Vollhardt. Strongly correlated materials: Insights from dynamical mean-field theory. *Phys. Rev. B*, 61(13):8906–8912, Apr 2000.

[3] A. Georges, G. Kotliar, W. Krauth, and M. J. Rozenberg. Dynamical mean-field theory of strongly correlated fermion systems and the limit of infinite dimensions. *Rev. Mod. Phys.*, 68:13–125, Jan 1996.

[4] V. I. Anisimov, A. I. Poteryaev, M. A. Korotin, A. O. Anokhin, and G. Kotliar. First-principles calculations of the electronic structure and spectra of strongly correlated systems: dynamical mean-field theory. *J. Phys.: Condens. Matter*, 9:7359–7367, Sep 1997.

[5] A. I. Lichtenstein and M. I. Katsnelson. Ab initio calculations of quasiparticle band structure in correlated systems: Lda++ approach. *Phys. Rev. B*, 57(12):6884–6895, Mar 1998.

[6] A. I. Lichtenstein and M. I. Katsnelson. Antiferromagnetism and d-wave superconductivity in cuprates: A cluster dynamical mean-field theory. *Phys. Rev. B*, 62(14):R9283–R9286, Oct 2000.

[7] A. N. Rubtsov, M. I. Katsnelson, and A. I. Lichtenstein. Dual fermion approach to nonlocal correlations in the hubbard model, cond-mat/0612196.

[8] Michael Potthoff and Matthias Balzer. Self-energy-functional theory for systems of interacting electrons with disorder. *Phys. Rev. B*, 75(12):125112, 2007.

[9] P. Hohenberg and W. Kohn. Inhomogeneous electron gas. *Phys. Rev.*, 136(3B):B864–B871, Nov 1964.

[10] W. Kohn and L. J. Sham. Self-consistent equations including exchange and correlation effects. *Phys. Rev.*, 140(4A):A1133–A1138, Nov 1965.

[11] P. Giannozzi. Large-scale electronic structure calculations in solids. In D. Neilson and

M.P. Das, editors, *Computational Approaches to Novel Condensed Matter Systems: Applications to Classical and Quantum Systems, Proceedings of the 3rd Gordon Godfrey Workshop on Condensed Matter Physics*, page 67, 1995.

[12] S. Baroni, S. de Gironcoli, A. Dal Corso, and P. Giannozzi. Phonons and related crystal properties from density-functional perturbation theory. *Rev. Mod. Phys.*, 73(2):515–562, Jul 2001.

[13] D. M. Ceperley and B. J. Alder. Ground state of the electron gas by a stochastic method. *Phys. Rev. Lett.*, 45(7):566–569, Aug 1980.

[14] R. O. Jones and O. Gunnarsson. The density functional formalism, its applications and prospects. *Rev. Mod. Phys.*, 61(3):689–746, Jul 1989.

[15] V. I. Anisimov, F. Aryasetiawan, and A. I. Lichtenstein. First-principles calculations of the electronic structure and spectra of strongly correlated systems: the lda + u method. *J. Phys.: Condens. Matter*, 9:767–808, 1997.

[16] A. G. Petukhov, I. I. Mazin, L. Chioncel, and A. I. Lichtenstein. Correlated metals and the $lda+u$ method. *Phys. Rev. B*, 67(15):153106, Apr 2003.

[17] K. Held, I.A. Nekrasov, G. Keller, V. Eyert, N. Blmer, A.K. McMahan, R.T. Scalettar, T. Pruschke, V.I. Anisimov, and D. Vollhardt. The lda+dmft approach to materials with strong electronic correlations. *Quantum Simulations of Complex Many-Body Systems: From Theory to Algorithms*, 10:175–209, 2002.

[18] A. Georges and G. Kotliar. Hubbard model in infinite dimensions. *Phys. Rev. B*, 45(12):6479–6483, Mar 1992.

[19] M. Jarrell. Hubbard model in infinite dimensions: A quantum monte carlo study. *Phys. Rev. Lett.*, 69(1):168–171, Jul 1992.

[20] A. C. Hewson. *The Kondo Problem to Heavy Fermions*. Cambridge University Press, Cambridge, 1993.

[21] R. Bulla, T. Costi, and T. Pruschke. The numerical renormalization group method for quantum impurity systems, cond-mat/0701105.

[22] G. Kotliar, S. Y. Savrasov, K. Haule, V. S. Oudovenko, O. Parcollet, and C. A. Marianetti. Electronic structure calculations with dynamical mean-field theory. *Reviews of Modern Physics*, 78(3):865, 2006.

[23] P. Coleman. New approach to the mixed-valence problem. *Phys. Rev. B*, 29(6):3035–3044,

Mar 1984.

[24] G. Kotliar and A. E. Ruckenstein. New functional integral approach to strongly correlated fermi systems: The gutzwiller approximation as a saddle point. *Phys. Rev. Lett.*, 57(11):1362–1365, Sep 1986.

[25] T. Li, P. Wölfle, and P. J. Hirschfeld. Spin-rotation-invariant slave-boson approach to the hubbard model. *Phys. Rev. B*, 40(10):6817–6821, Oct 1989.

[26] J. E. Hirsch and R. M. Fye. Monte carlo method for magnetic impurities in metals. *Phys. Rev. Lett.*, 56:2521–2524, 1986.

[27] R. M. Noack and S. R. Manmana. Diagonalization- and numerical renormalization-group-based methods for interacting quantum systems, cond-mat/0510321.

[28] M. Caffarel and W. Krauth. Exact diagonalization approach to correlated fermions in infinite dimensions: Mott transition and superconductivity. *Phys. Rev. Lett.*, 72(10):1545–1548, Mar 1994.

[29] Press W. H., S. A. Teukolsky, W. T. Vetterling, and B. P. Flannery. *Numerical Recipes in C++*. Cambridge University Press, 1993.

[30] **L**inear **a**lgebra **pack**age (lapack, fortran and c libraries; an implementation of the blas library is required for this package), http://www.netlib.org/lapack.

[31] **B**asic **l**inear **a**lgebra **s**ubprograms (blas, fortran libraries providing basic matrix and vector operations), http://www.netlib.org/blas.

[32] **A**utomatically **t**uned **l**inear **a**lgebra **s**oftware (atlas, efficient blas library, needs to be compiled), http://math-atlas.sourceforge.net/.

[33] A.A. Abrikosov, L.P. Gorkov, and I.E. Dzyaloshinskii. *Methods of Quantum Field Theory in Statistical Physics*. Pergamon, New York, 1965.

[34] R. Haydock. The recursive solution in the schrödinger equation. *Solid State Physics*, 35:215, 1980.

[35] B. N. Parlett. *The Symmetric Eigenvalue Problem*. Prentice-Hall, 1980.

[36] Th. Pruschke, R. Bulla, and M. Jarrell. Low-energy scale of the periodic anderson model. *Phys. Rev. B*, 61(19):12799–12809, May 2000.

[37] D. Meyer, A. C. Hewson, and R. Bulla. Gap formation and soft phonon mode in the holstein model. *Phys. Rev. Lett.*, 89(19):196401, Oct 2002.

[38] R. Bulla. Zero temperature metal-insulator transition in the infinite-dimensional hubbard

model. *Phys. Rev. Lett.*, 83(1):136–139, Jul 1999.

[39] K. G. Wilson. The renormalization group: Critical phenomena and the kondo problem. *Rev. Mod. Phys.*, 47(4):773–840, Oct 1975.

[40] P. W. Anderson. Localized magnetic states in metals. *Phys. Rev.*, 124(1):41–53, Oct 1961.

[41] H. R. Krishna-murthy, J. W. Wilkins, and K. G. Wilson. Renormalization-group approach to the anderson model of dilute magnetic alloys. i. static properties for the symmetric case. *Phys. Rev. B*, 21(3):1003–1043, Feb 1980.

[42] H. R. Krishna-murthy, J. W. Wilkins, and K. G. Wilson. Renormalization-group approach to the anderson model of dilute magnetic alloys. ii. static properties for the asymmetric case. *Phys. Rev. B*, 21(3):1044–1083, Feb 1980.

[43] B. A. Jones and C. M. Varma. Study of two magnetic impurities in a fermi gas. *Phys. Rev. Lett.*, 58(9):843–846, Mar 1987.

[44] B. A. Jones, C. M. Varma, and J. W. Wilkins. Low-temperature properties of the two-impurity kondo hamiltonian. *Phys. Rev. Lett.*, 61(1):125–128, Jul 1988.

[45] J. B. Silva, W. L. C. Lima, W. C. Oliveira, J. L. N. Mello, L. N. Oliveira, and J. W. Wilkins. Particle-hole asymmetry in the two-impurity kondo model. *Phys. Rev. Lett.*, 76(2):275–278, Jan 1996.

[46] K. Ingersent, B. A. Jones, and J. W. Wilkins. Study of the two-impurity, two-channel kondo hamiltonian. *Phys. Rev. Lett.*, 69(17):2594–2597, Oct 1992.

[47] L. N. Oliveira and J. W. Wilkins. New approach to the x-ray-absorption problem. *Phys. Rev. B*, 24(8):4863–4866, Oct 1981.

[48] L. N. Oliveira and J. W. Wilkins. Fano antiresonances in x-ray-absorption spectroscopy. *Phys. Rev. B*, 32(2):696–707, Jul 1985.

[49] H. O. Frota and L. N. Oliveira. Photoemission spectroscopy for the spin-degenerate anderson model. *Phys. Rev. B*, 33(11):7871–7874, Jun 1986.

[50] T. A. Costi and A. C. Hewson. Resistivity cross-over for the nondegenerate anderson model. *Phil. Mag. B*, 65:1165–1170, 1992.

[51] T. A. Costi, P. Schmitteckert, J. Kroha P., and Wölfle. Numerical renormalization group study of pseudo-fermion and slave-boson spectral functions in the single impurity anderson model. *Phys. Rev. Lett.*, 73(9):1275–1278, Aug 1994.

[52] W. Hofstetter. Generalized numerical renormalization group for dynamical quantities.

Phys. Rev. Lett., 85(7):1508–1511, Aug 2000.

[53] T. A. Costi. Renormalization-group approach to nonequilibrium green functionsin correlated impurity systems. *Phys. Rev. B*, 55(5):3003–3009, Feb 1997.

[54] F. B. Anders and A. Schiller. Real-time dynamics in quantum-impurity systems: A time-dependent numerical renormalization-group approach. *Phys. Rev. Lett.*, 95:196801, Oct 2005.

[55] F. B. Anders and T. Pruschke. Can competition between the crystal field and the kondo effect cause non-fermi-liquid-like behavior? *Phys. Rev. Lett.*, 96:086404, Mar 2006.

[56] R. Bulla, H. Lee, N. Tong, and M. Vojta. Numerical renormalization group for quantum impurities in a bosonic bath. *Phys. Rev. B*, 71:045122, Jan 2005.

[57] E. Dagotto. Correlated electrons in high-temperature superconductors. *Rev. Mod. Phys.*, 66(3):763–840, Jul 1994.

[58] D. J. Scalapino and R. L. Sugar. Method for performing monte carlo calculations for systems with fermions. *Phys. Rev. Lett.*, 46:519, 1981.

[59] R. Blankenbecler, D. J. Scalapino, and R. L. Sugar. Monte carlo calculations of coupled boson-fermion systems. i. *Phys. Rev. D*, 24:2278, 1981.

[60] J. E. Hirsch. Discrete hubbard-stratonovich transformation for fermion lattice models. *Phys. Rev. B*, 28:4059, 1983.

[61] J. E. Hirsch. Two-dimensional hubbard model: Numerical simulation study. *Phys. Rev. B*, 31:4403, 1985.

[62] S. R. White. Numerical canonical transformation approach to quantum many-body problems. *J. of Chem. Phys.*, 117:7472, 2002.

[63] S. W. Zhang and H. Krakauer. Quantum monte carlo method using phase-free random walks with slater determinants. *Phys. Rev. Lett.*, 90:136401, 2003.

[64] P. Sun and G. Kotliar. Extended dynamical mean-field theory and gw method. *Phys. Rev. B*, 66:085120, 2002.

[65] A. W. Sandvik and J. Kurkijärvi. Quantum monte carlo simulation method for spin systems. *Phys. Rev. B*, 43:5950, 1991.

[66] N. V. Prokof'ev, B. V. Svistunov, and I. S. Tupitsyn. Exact quantum monte carlo process for the statistics of discrete systems. *JETP Lett.*, 64:911–916, 1996.

[67] J. Hubbard. Calculation of partition functions. *Phys. Rev. Lett.*, 3:77, 1959.

[68] P. Werner, A. Comanac, L. de' Medici, M. Troyer, and A. J. Millis. Continuous-time solver for quantum impurity models. *Phys. Rev. Lett.*, 97:076405, 2006.

[69] J. Yoo, S. Chandrasekharan, R. K Kaul, D. Ullmo, and H. U Baranger. On the sign problem in the hirsch-fye algorithm for impurity problems. *J. Phys. A: Math. Gen.*, 38:10307–10310, 2005.

[70] M. J. Rozenberg. Integer-filling metal-insulator transitions in the degenerate hubbard model. *Phys. Rev. B*, 55(8):R4855–R4858, Feb 1997.

[71] M. I. Katsnelson and A. I. Lichtenstein. First-principles calculations of magnetic interactions in correlated systems. *Phys. Rev. B*, 61(13):8906–8912, Apr 2000.

[72] S. Sakai, R. Arita, K. Held, and H. Aoki. Quantum monte carlo study for multiorbital systems with preserved spin and orbital rotational symmetries. *Phys. Rev. B*, 74:155102, Oct 2006.

[73] S. Sakai, R. Arita, and H. Aoki. Numerical algorithm for the double-orbital hubbard model: Hund-coupled pairing symmetry in the doped case. *Phys. Rev. B*, 70(17):172504, 2004.

[74] B. B. Beard and U.-J. Wiese. Simulations of discrete quantum systems in continuous euclidean time. *Phys. Rev. Lett.*, 77:5130, 1996.

[75] P. E. Kornilovitch. Continuous-time quantum monte carlo algorithm for the lattice polaron. *Phys. Rev. Lett.*, 81:5382, 1998.

[76] S. M. A. Rombouts, K. Heyde, and N. Jachowicz. Quantum monte carlo method for fermions, free of discretization errors. *Phys. Rev. Lett.*, 82:4155, 1999.

[77] V. S. Oudovenko and G. Kotliar. Thermoelectric properties of the degenerate hubbard model. *Phys. Rev. B*, 65(7):075102, Jan 2002.

[78] M. Feldbacher, K. Held, and F. F. Assaad. Feldbacher, held, and assad reply:. *Phys. Rev. Lett.*, 96(13):139702, 2006.

[79] M. I. Katsnelson. Comment on "projective quantum monte carlo method for the anderson impurity model and its application to dynamical mean field theory". *Phys. Rev. Lett.*, 96(13):139701, 2006.

[80] M. Feldbacher, K. Held, and F. F. Assaad. Feldbacher, held, and assad reply:. *Phys. Rev. Lett.*, 96(13):139702, 2006.

[81] A. N. Rubtsov, V. V. Savkin, and A. I. Lichtenstein. Continuous-time quantum monte

carlo method for fermions. *Phys. Rev. B*, 72:035122, 2005.

[82] P. Werner and A. J. Millis. Hybridization expansion impurity solver: General formulation and application to kondo lattice and two-orbital models. *Phys. Rev. B*, 74:155107, 2006.

[83] E. Gull, P. Werner, A. J. Millis, and M. Troyer. Performance analysis of continuous-time solvers for quantum impurity models, cond-mat/0609438.

[84] F. F. Assaad and T. C. Lang. Diagrammatic determinantal quantum monte carlo methods: Projective schemes and applications to the hubbard-holstein model. *Phys. Rev. B*, 76(3):035116, 2007.

[85] G. D. Mahan. *Many-Particle Physics*. Plenum, 1990.

[86] H. R. Krishna-murthy, J. W. Wilkins, and K. G. Wilson. Renormalization-group approach to the anderson model of dilute magnetic alloys. i. static properties for the symmetric case. *Phys. Rev. B*, 21(3):1003–1043, Feb 1980.

[87] Giuseppe E. Santoro and Gabriele F. Giuliani. Impurity spin susceptibility of the anderson model: A perturbative approach. *Phys. Rev. B*, 44(5):2209–2219, Aug 1991.

[88] A. Zhuravlev, E. Gorelov, S. Kettemann, and A. Lichtenstein. Impurity spin susceptibility of the anderson model: A perturbative approach. *to be published*, 2007.

[89] N. Menyhard. Perturbation calculation of the susceptibility in the symmetric anderson model. *Solid State Communications*, 12(3):215–217, Feb 1973.

[90] K. Yamada. Perturbation expansion for the anderson hamiltonian. ii. *Progr. of Theor. Phys.*, 53(4):970, 1975.

[91] M. Jarrell and J. E. Gubernatis. Bayesian inference and the analytic continuation of imaginary-time quantum monte carlo data. *Phys. Rep.*, 269:133, 1996.

[92] Anders W. Sandvik. Stochastic method for analytic continuation of quantum monte carlo data. *Phys. Rev. B*, 57(17):10287–10290, May 1998.

[93] L. Kouwenhoven and L. Glazman. Revival of the kondo effect. *Physics World*, 1:33–38, Jan 2001.

[94] W. J. de Haas, J. de Boer, and G. J. van den Berg. The electrical resistance of gold, copper and lead at low temperatures. *Physica*, 1:1115, 1933.

[95] V. Madhavan, W. Chen, T. Jamneala, M. F. Crommie, and N. S. Wingreen. Tunneling into a single magnetic atom: Spectroscopic evidence of the kondo resonance. *Science*, 280:567, 1998.

[96] J. Li. and W.-D. Schneider. Kondo scattering observed at a single magnetic impurity. *Phys. Rev. Lett.*, 80:2893, 1998.

[97] N. Knorr, M. A. Schneider, L. Diekhöner, P. Wahl, and K. Kern. Kondo Effect of Single Co Adatoms on Cu Surfaces. *Phys. Rev. Lett.*, 88(9):096804, Feb 2002.

[98] H. C. Manoharan, C. P. Lutz, and D. M. Eigler. Quantum mirages formed by coherent projection of electronic structure. *Nature*, 403:512, 2000.

[99] A. Zhao, Q. Li, L. Chen, H.Xiang, W. Wang, S. Pan, B. Wang, X. Xiao, J. Yang, J. G. Hou, and Q. Zhu. The Resonating Valence Bond State in La_2CuO_4 and Superconductivity. *Science*, 309:1542–1544, Sep 2005.

[100] U. Fano. Effects of configuration interaction on intensities and phase shifts. *Phys. Rev.*, 124(6):1866–1878, Dec 1961.

[101] M. Plihal and J. W. Gadzuk. Nonequilibrium theory of scanning tunneling spectroscopy via adsorbate resonances: Nonmagnetic and kondo impurities. *Phys. Rev. B*, 63(8):085404, Feb 2001.

[102] O. Újsághy, J. Kroha, L. Szunyogh, and A. Zawadowski. Theory of the fano resonance in the stm tunneling density of states due to a single kondo impurity. *Phys. Rev. Lett.*, 85(12):2557–2560, Sep 2000.

[103] P. Wahl, L. Diekhöner, M. A. Schneider, L. Vitali, G. Wittich, and K. Kern. Kondo temperature of magnetic impurities at surfaces. *Phys. Rev. Lett.*, 93:176603, Oct 2004.

[104] A. A. Abrikosov. Electron scattering on magnetic impurities in metals and anomalous resistivity effects. *Physics*, 2(1):5–20, 1965.

[105] G. M. Pastor. Magnetic impurities in small metal clusters. *Annalen der Physik*, 14(9–10):547–555, 2005.

[106] M. Lübcke, B. Sonntag, W. Niemann, and P. Rabe. Size-dependent valence change in small pr, nd, and sm clusters isolated in solid ar. *Phys. Rev. B*, 34(8):5184–5190, Oct 1986.

[107] R.-J. Tarento and P. Joyes. Gutzwiller-type approach of the size-dependent valence change in small pr aggregates. *Phys. Rev. B*, 41(7):4547–4551, Mar 1990.

[108] M. Koga, W. Liu, M. Dolg, and P. Fulde. Orbital localization and delocalization effects in the U $5f^2$ configuration: Impurity problem. *Phys. Rev. B*, 57(17):10648–10654, May 1998.

[109] O. Pietzsch, S. Okatov, A. Kubetzka, M. Bode, S. Heinze, A. Lichtenstein, and R. Wiesendanger. Theory of the fano resonance in the stm tunneling density of states due to a single kondo impurity. *Phys. Rev. Lett.*, 96:237203, Jun 2006.

[110] L.M. Falicov, W. Hanke, and M.B. Maple (eds.). *Valence Fluctuations in Solids*. North-Holland, Amsterdam, 1981.

[111] P. Fulde. *Electron correlations in molecules and solids*. Springer, Berlin, 1993.

[112] J. Kondo. Resistance minimum in dilute magnetic alloys. *Progr. Theor. Phys.*, 32:37, 1964.

[113] Wolfgang B. Thimm, Johann Kroha, and Jan von Delft. Kondo box: A magnetic impurity in an ultrasmall metallic grain. *Phys. Rev. Lett.*, 82(10):2143–2146, Mar 1999.

[114] A. Zhuravlev, I. Zharekeshev, E. Gorelov, A. I. Lichtenstein, E. R. Mucciolo, and S. Kettemann. Nonperturbative scaling theory of free magnetic moment phases in disordered metals, cond-mat.str-el/0706.3456, Accepted to Phys. Rev. Lett. (LF11622).

[115] M. Imada, A. Fujimori, and Y. Tokura. Metal-insulator transitions. *Rev. Mod. Phys.*, 70(4):1039–1263, Oct 1998.

[116] C. Castellani, C. R. Natoli, and J. Ranninger. Magnetic structure of V_2O_3 in the insulating phase. *Phys. Rev. B*, 18(9):4945–4966, Nov 1978.

[117] Fiete, Gregory A., and Eric J. Heller. Colloquium: Theory of quantum corrals and quantum mirages. *Rev. Mod. Phys.*, 75(3):933–948, Jul 2003.

[118] Oded Agam and Avraham Schiller. Projecting the kondo effect: Theory of the quantum mirage. *Phys. Rev. Lett.*, 86(3):484–487, Jan 2001.

[119] D. Porras, J. Fernández-Rossier, and C. Tejedor. Microscopic theory for quantum mirages in quantum corrals. *Phys. Rev. B*, 63(15):155406, Mar 2001.

[120] L. Limot and R. Berndt. Kondo effect and surface-state electrons, cond-mat/0312434.

[121] Chiung-Yuan Lin, A. H. Castro Neto, and B. A. Jones. First-principles calculation of the single impurity surface kondo resonance. *Phys. Rev. Lett.*, 97:156102, Oct 2006.

[122] A. Liebsch and A. Lichtenstein. Photoemission Quasiparticle Spectra of Sr_2RuO_4. *Phys. Rev. Lett.*, 84(7):1591–1594, Feb 2000.

[123] O. Gunnarsson, O. K. Andersen, O. Jepsen, and J. Zaanen. Density-functional calculation of the parameters in the anderson model: Application to mn in cdte. *Phys. Rev. B*, 39(3):1708–1722, Jan 1989.

[124] T. Asada and S. Blügel. Total Energy Spectra of Complete Sets of Magnetic States for fcc-Fe Films on Cu (100). *Phys. Rev. Lett.*, 79(3):507–510, Jul 1997.

[125] C. F. Hirjibehedin, C. P. Lutz, and A. J. Heinrich. Spin coupling in engineered atomic structures. *Science*, 312:1021, 1998.

[126] W. Chen, T. Jamneala, V. Madhavan, and M. F. Crommie. Disappearance of the kondo resonance for atomically fabricated cobalt dimers. *Phys. Rev. B*, 60(12):R8529–R8532, Sep 1999.

[127] P. Wahl, P. Simon, L. Diekhoner, V. S. Stepanyuk, P. Bruno, M. A. Schneider, and K. Kern. Exchange interaction between single magnetic adatoms. *Phys. Rev. Lett.*, 98(5):056601, 2007.

[128] O. Pietzsch, S. Okatov, A. Kubetzka, M. Bode, S. Heinze, A. Lichtenstein, and R. Wiesendanger. Spin-Resolved Electronic Structure of Nanoscale Cobalt Islands on Cu (111). *Phys. Rev. Lett.*, 96(23):237203, 2006.

[129] F. Meier, K. von Bergmann, P. Ferriani, J. Wiebe, M. Bode, K. Hashimoto, S. Heinze, and R. Wiesendanger. Spin-dependent electronic and magnetic properties of Co nanostructures on Pt (111) studied by spin-resolved scanning tunneling spectroscopy. *Phys. Rev. B*, 74(19):195411, 2006.

[130] M. D. Daybell and W. A. Steyert. Localized magnetic impurity states in metals: Some experimental relationships. *Rev. Mod. Phys.*, 40(2):380–389, Apr 1968.

[131] S. Y. Savrasov. Program lmtart for electronic structure calculations. *Zeitschrift für Kristallographie*, 220:555–557, 2005.

[132] N. Quaas, M. Wenderoth, A. Weismann, R. G. Ulbrich, and K. Schonhammer. Kondo resonance of single Co atoms embedded in Cu (111). *Phys. Rev. B*, 69(20):201103, 2004.

[133] P. W. Anderson. The Resonating Valence Bond State in La_2CuO_4 and Superconductivity. *Science*, 235:1196–1198, Mar 1987.

[134] J. Kunes, V. I. Anisimov, A. V. Lukoyanov, and D. Vollhardt. Local correlations and hole doping in nio: A dynamical mean-field study. *Phys. Rev. B*, 75(16):165115, 2007.

[135] S. Okamoto and A. J. Millis. Integer-filling metal-insulator transitions in the degenerate hubbard model. *Phys. Rev. B*, 70:195120, Nov 2004.

[136] F. Lechermann, S. Biermann, and A. Georges. Importance of Interorbital Charge Transfers for the Metal-to-Insulator Transition of $BaVS_3$. *Phys. Rev. Lett.*, 94:166402, 2005.

[137] Y. Tokura and N. Nagaosa. Orbital physics in transition-metal oxides. *Science*, 288:462–468, Apr 2000.

[138] A. Koga, N. Kawakami, M. Rice, and M. Sigrist. Orbital-selective mott transitions in the degenerate hubbard model. *Phys. Rev. Lett.*, 92:216402, 2004.

[139] A. Liebsch. Mott transitions in multiorbital systems. *Phys. Rev. Lett.*, 91(22):226401, Nov 2003.

[140] P. Werner and A. J. Millis. High-spin to low-spin and orbital polarization transitions in multiorbital mott systems, cond-mat/0704.0057v1.

[141] S. Biermann, L. de' Medici, and A. Georges. Non-fermi-liquid behavior and double-exchange physics in orbital-selective mott systems. *Phys. Rev. Lett.*, 95(20):206401, 2005.

[142] A. Liebsch. Novel mott transitions in a nonisotropic two-band hubbard model. *Phys. Rev. Lett.*, 95(11):116402, 2005.

[143] L. de'Medici, A. Georges, and S. Biermann. Orbital-selective mott transition in multi-band systems: Slave-spin representation and dynamical mean-field theory. *Phys. Rev. B*, 72(20):205124, 2005.

[144] Y. Maeno, H. Hashimoto, K. Yoshida, S. Nishizaki, T. Fujita, J. G. Bednorz, and F. Lichtenberg. Superconductivity in a layered perovskite without copper. *Nature*, 372:532, 2002.

[145] Z. V. Pchelkina, I. A. Nekrasov, Th. Pruschke, A. Sekiyama, S. Suga, V. I. Anisimov, and D. Vollhardt. Evidence for strong electronic correlations in the spectra of Sr_2RuO_4. *Phys. Rev. B*, 75(3):035122, 2007.

[146] O. Krogh Andersen. Linear methods in band theory. *Phys. Rev. B*, 12(8):3060–3083, Oct 1975.

[147] V. I. Anisimov, D. E. Kondakov, A. V. Kozhevnikov, I. A. Nekrasov, Z. V. Pchelkina, J. W. Allen, S.-K. Mo, H.-D. Kim, P. Metcalf, S. Suga, A. Sekiyama, G. Keller, I. Leonov, X. Ren, and D. Vollhardt. Full orbital calculation scheme for materials with strongly correlated electrons. *Phys. Rev. B*, 71(12):125119, 2005.

[148] A. P. Mackenzie, S. R. Julian, A. J. Diver, G. J. McMullan, M. P. Ray, G. G. Lonzarich, Y. Maeno, S. Nishizaki, and T. Fujita. Quantum oscillations in the layered perovskite superconductor $\mathrm{sr}_2\mathrm{ruo}_4$. *Phys. Rev. Lett.*, 76(20):3786–3789, May 1996.

[149] A. V. Puchkov, Z.-X. Shen, T. Kimura, and Y. Tokura. ARPES results on Sr_2RuO_4 : Fermi surface revisited. *Phys. Rev. B*, 58(20):R13322–R13325, Nov 1998.

[150] A. Liebsch and H. Ishida. Subband Filling and Mott Transition in $Ca_{2-x}Sr_xRuO_4$. *Phys. Rev. Lett.*, 98(21):216403, 2007.

[151] V. I. Anisimov and O. Gunnarsson. Density-functional calculation of effective coulomb interactions in metals. *Phys. Rev. B*, 43(10):7570–7574, Apr 1991.

Acknowledgments

I would like to express my gratitude to all the people who gave me assistance and support during my work at the *1. Institut für Theoretische Physik*.

First of all, I would like to thank my supervisor, Prof. Alexander Lichtenstein, for giving me the opportunity to study such interesting areas of modern computational physics. I am thankful for the interesting topic proposed, for many helpful discussions during the work, and for patiently explaining to me the basics of many-body physics. This support and encouragement help me a lot the complicated task of writing this thesis.

I am greatly indebt to Alexey Rubtsov and Vladimir Savkin for providing the starting help with the initial one-band CT-QMC algorithm. I am greatly thankful to to Alexey Rubtsov for helping me on every stage of developing the multiorbital formalism. I would also like to thank Prof. Mikhail Katsnelson for his friendly attitude and motivating ideas.

I give special thanks to Stefan Kettemann for fruitful collaboration in the area of disordered Kondo-systems. Also I want to thank Andrey Zhuravlev for his contribution to the present work, in form of NRG and ED calculations used as a benchmark for the CT-QMC method, as well as for his initiative to rewrite the code, making it more clear and finally for assistance in developing the susceptibilities block. I am grateful to Kelly Patton for useful discussions on STM and STS physics and for assistance in repairing my “Russian” English.

I am very grateful to all members of our group for supporting me all the time, especially Hartmut Hafermann and Tim Wehling for testing and further developing the CT-QMC code we used. I thank Sergej Brener for reading and criticizing the early versions of my thesis and many thanks to Frank Lechermann for useful discussions about DMFT and behavior of orbital selective Mott transition systems.

I would like to thank Prof. Stefan Blügel, Prof. Eva Pavarini, Erik Koch, Ansgar Liebsch, Theo Costi, and Phivos Mavropoulos for fruitful discussions on realistic solid-state physics and new approaches in many-body theory during my visit to FZ Jülich.

I would like to express my appreciation to Alexey Lukoyanov, Alexey Shorikov, and Prof. Vladimir Anisimov for productive collaboration in the framework of the LDA+DMFT approach, during my visit to Ekaterinburg. I am greteful to Alexander Shick, Prof. Peter Oppeneer, and Prof. Olle Eriksson for useful discussions during my visit to Uppsala.

I would also like to thank Prof. Kurt Scharnberg for his kind assistance working out and publishing a chapter in the Springer book. Also I would like to thank Prof. Hartmut Monien for helping me gain insight into $C++$.

I want to also acknowledge young members of our group: Felix Binder, Claudius Herkt, Sergej Schuwalow, German Ulm, Martin Kecker and Christoph Jung for their good attitude and for creating a friendly, informal, and collaborative atmosphere.

I would like to thank all the members of my committee, especially Alexander Chudnovskiy, Prof. Eva Pavarini, and Prof. Michael Potthoff for the time and energy they have devoted to reading my work. In spite of busy schedules, all have been readily available for advice, reading, or simply a word of encouragement.

I acknowledge Prof. Roland Wiesendanger for giving me a short SFB-668 grant to have the possibility to complete my work, and for basic motivation to study 3*d* imputities on metallic surfaces.

This work was done in the area of computational physics, and it would not be possible to manage this project without the staff keeping computers running. I acknowledge Bodo Krause-Kyora for kind help with all the computer problems on the PHYSnet, and I would express my appreciation to the personnel of Hamburg regional computational center (RRZ), especially to Elisabeth Kahnert for giving me the possibility to use the first supercomputer in my life.

I am also very thankful to the secretaries of our Institute, namely Mrs. Schmidtke and Mrs. Sen for their assistance in breaking through all the bureaucracy.

Finally, I want to thank my parents, without their encouragement and support I would never have chosen this path for my life.

Thank you all!